

We are IntechOpen, the world's leading publisher of Open Access books Built by scientists, for scientists

6,300

Open access books available

171,000

International authors and editors

190M

Downloads

Our authors are among the

154

Countries delivered to

TOP 1%

most cited scientists

12.2%

Contributors from top 500 universities



WEB OF SCIENCE™

Selection of our books indexed in the Book Citation Index
in Web of Science™ Core Collection (BKCI)

Interested in publishing with us?
Contact book.department@intechopen.com

Numbers displayed above are based on latest data collected.
For more information visit www.intechopen.com



Introductory Chapter: Ion Beam Applications

Ishaq Ahmad and Fabian I. Ezema

Additional information is available at the end of the chapter

<http://dx.doi.org/10.5772/intechopen.78966>

1. Overview

Ion beam instruments such as particle accelerators, focused ion beams (FIB), and ion implanters are versatile instruments which are broadly applied almost in all field of physics from nuclear physics to particle physics, condense matter physics, and atomic physics. These are also an important tool in other areas of science and technologies such as chemistry, environment sciences, biology, space science and engineering, and semiconductor technology. Its applications are substantially being extended for generating cluster ions, synchrotron radiations, focused ion beams with molecular nitrogen source gas, and proton-proton colliders. Progress in nuclear and particle physics originated from studies with ion beam is playing now a determining role in astrophysics and cosmology. Similarly, low energy ion beam, such as ion implanters and FIB, are also useful instruments for device fabrication and microscopy.

This chapter aimed to present a brief review of a broad range of applications of the ion beam in diversified fields which will be useful for the common reader to understand ion beam science and technology. Finally, the latest research using MeV ion beam, focused ion beam, and ion implanter is compiled in this book in three respective sections. For a further concise review of ion beam applications, electron beams are excluded from this review chapter and book, even though electron microscopes and other useful applications are being emerged in different areas of fields. For example, focused electron beam was used in patterning and cutting of nanowires [1]. **Figure 1** shows the patterning of ZnO nanowires using focused electron beams at transmission electron microscopy (TEM).

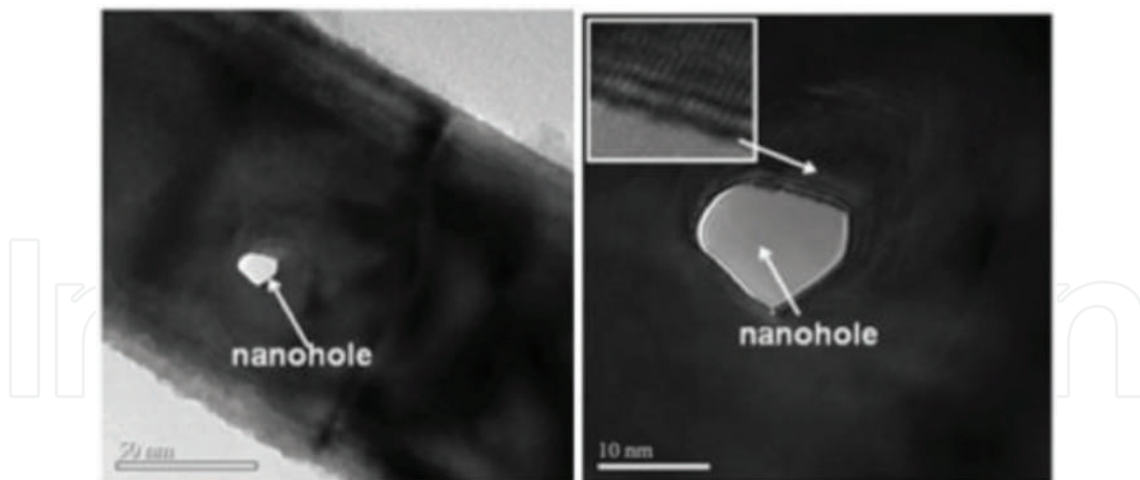


Figure 1. Focused electron beam to create nanoholes in ZnO nanowires [1].

2. Applications

2.1. Materials science

This section introduces to the materials scientists, chemists, and physicists about the ion beam techniques for materials analysis, modification of materials, and development of new materials using ion beam. MeV ion beams for materials analysis techniques are being used as complementary techniques in materials analysis. These are the group of non-destructive analytical techniques such as particle induced X-ray emission (PIXE), particle-induced gamma-ray emission (PIGE), nuclear reaction analysis (NRA), Rutherford backscattering (RBS), and ion channeling, which are being used to analyze composition and depth profiling of solids. Almost all elements from hydrogen onward can be probed by ion beam analysis (IBA). IBA techniques are discussed in detail in Section 2. Focused or collimated beam into micron and submicron (Microprobe) is now developed, which is useful for mapping of lateral elemental distribution over a specimen. These microbeams are useful for high-resolution imaging by measuring density variations through scanning transmission ion microscopy (STIM) technique.

Ion beam modification of materials is an important application of ion beam. Recently, boron carbonitride nanotubes were synthesized from boron nitride nanotubes using C ion beam irradiation [2]. Similarly, phase transformation of thin film and nanostructured materials by ion beams is another important application. Ion beam-induced controlled modification of physical properties is possible in thin film and nanostructured materials [2–8]. Phase segregation and separation is another unique application of ion beam [9].

Ion implantation is an exceptional surface treatment method to implant N-type and P-type dopants into semiconductors to make solid-state electronics. Moreover, dilute magnetic semiconductor devices could be synthesized through direct implantation of magnetic elements into nonmagnetic semiconductors [10, 11]. After developed FIB, now it is also possible to

implant required elements into required depth to make semiconductor devices. Section 3 describes the advantages of ion implantation process with emerging new applications.

Focused ion beam in keV energies is also used for microscopy of materials [12]. FIB instrument can be utilized for microstructure tomography in the range from ~ 100 nm to $10\ \mu\text{m}$. Advanced FIB microscopy has been described in detail in Section 3.

2.2. Environmental sciences

IBA techniques such as PIXE are widely used for environmental studies. Trace element measurement in aerosol samples is an important application of MeV ion beam. After developed microprobe, now it is possible to measure or mapping of heavy metals in various samples like trees, fish, deposit mining dust on trees leaf, glacial melting study, etc., which give valuable seasonal and historical information of pollution to the particular area of study. Many authors have proven the diagnostic usefulness of hair analysis in assessing pathological elemental concentrations in the body. Hair has been shown to reflect environmental and occupational exposure to lead, mercury, aluminum [13], and a combination of multiple metals. Microanalysis of hair to assess the toxic metals in scalp hair of artisanal miners are important environmental studies using micro PIXE. The PIXE technique has been proven as a high accurate, sensitive, and nondestructive method to determine concentration and composition of chemical elements. Beside these, PIXE technique has been successfully used in many other environmental studies like elemental mapping, source appointment, and chemical characterization of various pollutants.

2.3. Device fabrications

Focused ion beam either in MeV or keV energies is a considerable tool in science and technology for micro and nanodevice fabrications using both bottom-up and top-down approaches. In the bottom-up approach, individual nano-objects such as nanowires and nanotubes can be assembled directly together in form of functional welded networks using ion beam induced nano-welding technique. Ion beam-induced nanowelding is another option to make nanowire/nanotube-welded junctions and to make nanodevices or integrate nanodevices. Recently, researchers used ion beam as a tool to weld carbon nanotubes, silver nanowires, Ni nanowires, and SiC nanowires to make junctions and large-scale welded networks [14–21] (**Figure 2**).

In top-down device fabrication approach, 3D MeV proton beam writing is an important technique to make micro and nanodevices [22]. Whereas, keV energy FIB is now an essential tool to use for TEM sample preparation and device fabrication and to fabricate complex nanoscale structures/patterns. It is a tool that directly makes a 3D and 2D pattern without masks from a few nanometers to hundreds of micrometers in size. Compact FIB instruments are developed and being used to fabricate microelectromechanical systems (MEMS)-based devices, microfluidic chips, photonic devices, and DNA sequencing nanopore membranes [23, 24]. More detail FIB applications are described in Section 3.

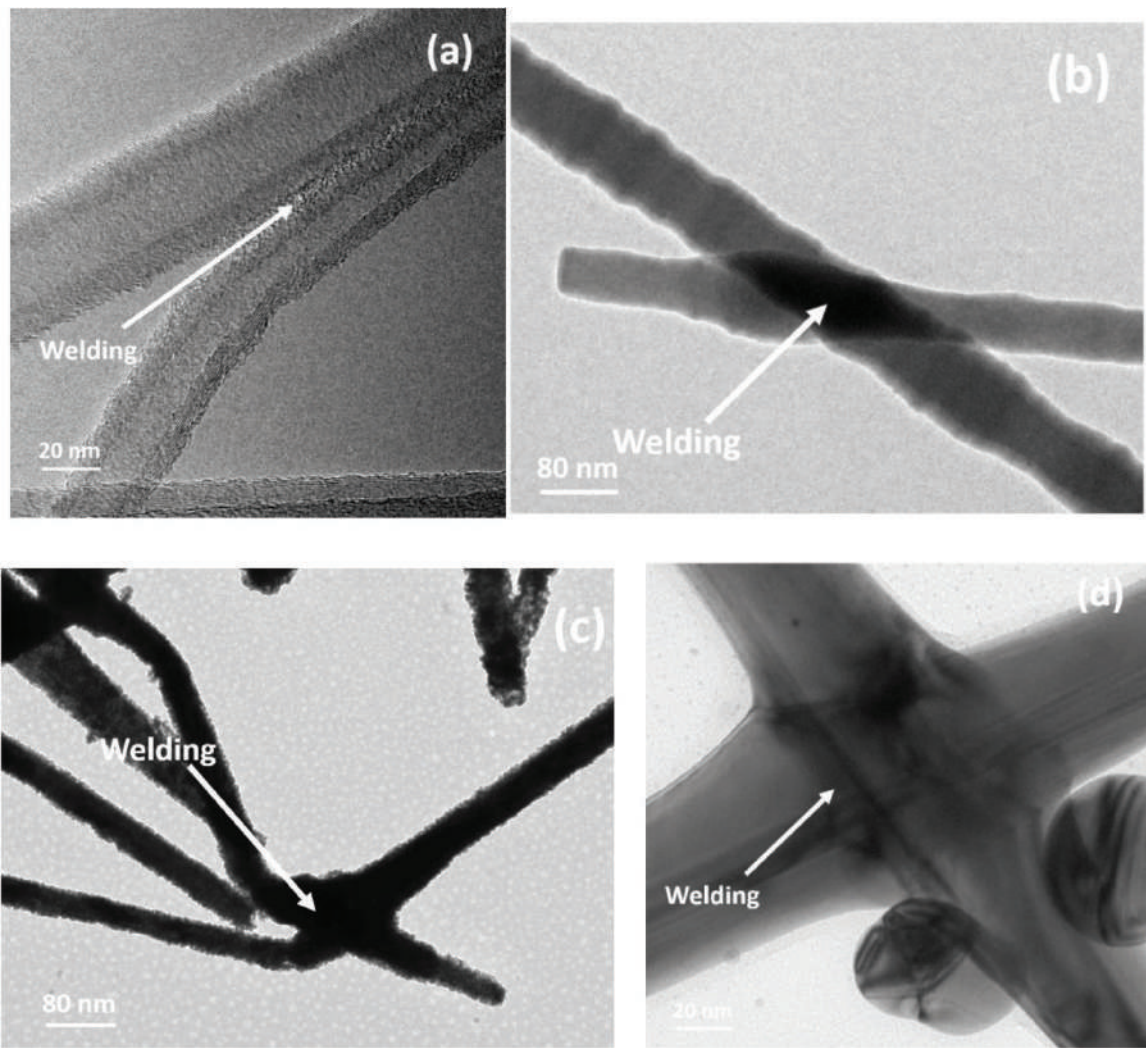


Figure 2. Ion beam-induced welding of (a) multiwalled carbon nanotubes [21], (b) SiC nanowires [14], (c) Cu nanowires, and (d) silver nanowires [18].

2.4. Atomic physics

Excitation and ionization of atoms by ion beam is another application of ion beam technology to study atomic structure. Ion beam-induced X-ray emission is a rich phenomenon to study the complicated process during ion beam interaction with matter. The fundamental parameter such as ionization cross section is a pure quantum mechanical phenomenon. When an ion passes through the target atom, the target atom becomes ionized due to coulombic interaction of ions with target atom. The target atom is ionized by absorbing ion beam energy and rest of the energy is utilized in ejection of auger electron in case of atomic collision and heating.

When an atom deionized, it released the absorbed energy in the form of photon, and its excess energy ejects the auger electron and rest of the energy loss goes in the heating of sample. The probability of emission of x-rays or photon from particular due to electron transition from upper shell to lower shell is called the fluorescence of particular shell. We can measure the

X-ray production cross section of particular shell using fluorescence yield of shell of target element. For K-shell, X-ray production cross-section data are available so far to support PIXE technique for materials analysis, whereas a lot of discrepancies exist in L-shell and M-shell of X-ray production cross section measurement. As it had become complicated due to fluorescence and auger electron transition between levels and sublevels.

The fine and hyperfine lines originating from s, p, d and f orbitals and its suborbitals (from levels and sublevel) can be studied and explore the fluorescence and auger electron transition and Coster-Kronig transition for L- and M-shell X-ray production cross section. The relative intensity ratios of K-shell, L-shell, and M-shell transition lines can be explored from light and heavy ion in advanced studies. Decreasing and increasing trend of intensity ratio of transitions lines $K\alpha/K\beta$ and $L\beta/L\alpha$ can also be explored as a function of ascending order of elements Z, respectively.

The stopping power or energy loss of projectile in the matter is another research area. Due to lack of correct knowledge of stopping power, error in cross-section measurement is large. Bethe formalism and Ziegler, the founder of TRIM/SRIM software for heavy ions stopping power, may deviate from the experimental results at different energy ranges. The study reveals that there are many discrepancies exist in the theoretical models. Using heavy ion for cross section and stopping power studies can improve the theoretical models.

The multi-ionization effect by heavy ion is an open research field and a once need to explore the complicated physics exit behind it. PIXE using heavy ion lead us to find the fact for corrections of theoretical Models.

2.5. Nuclear physics

Study of nuclear structure and nuclear reaction using ion beam is another application of ion beam technology. As the diameter of the nucleus is less than 10^{-14} m, the nuclear structure study with microscopy technique is hard to investigate. Therefore, high energy ions which have a size comparable to a nucleus are another option to investigate the structure of the nucleus. Scattering cross section could be measured by energetic ions interacting with target nucleus. Ion-induced nuclear reaction could be possible to emit secondary particles such as neutrons, alpha particle, gamma-rays, and beta particles. Once energies and angular distribution of secondary particle emission observe, then size and shape of the nucleus and the forces existing inside the nucleus could be deduced. Large range of ion beam-induced nuclear reactions is possible.

Proton beams with different energies are very useful for various aspects of research, such as proton beams with energies between 1 MeV and 1 GeV are almost always used for nuclear structure studies. Proton beam with energy between 1 and 100 MeV could be made to interact with whole nuclei or with several nucleons, while proton beam with energy between 100 and 1000 MeV could be interacted with individual nucleons in the nucleus which giving more precise information about each nucleon. Ion beam energies greater than 1 GeV are useful to produce short-lived particles such as mesons [25].

2.6. Biology

Ion beam could be applied in biology for probing, damaging and modifying the biological samples. Ion beam accelerators have advanced further by the introduction of nuclear microprobes. These microprobes have opened up new areas of research in biological science by allowing elemental microanalysis, with imaging capabilities, particularly suitable for the measurement of trace elements in biological tissues. Whereas ion beam-induced mutation of crops, vegetables and fruits are matured method. Micro PIXE is continuously applied in life science for comprehensive food crops analysis to determine traces of toxic heavy metals.

2.7. Particle physics

High-energy ion beams produced by particle accelerators also have vast applications in particle physics as it is a tool to study extreme states of matter. In high energy physics, particle colliders have taken part in a key role in scientific discoveries for last many decades. Particle colliders are basically ion beam accelerators where particles are accelerated up to relativistic speed to collide with a stationary target or head-on collision with each other like proton-proton colliders. At sufficiently high energy, relativistic particles smash into other high energy particles. Energies of the colliders continuously increase over time for exploring new physics/particles. Moreover, advanced high energy particle detectors are being developed for understanding the properties of high energy particles such as mass, energy, charge, spin, and isospin, which are being created during collision of relativistic particles.

Large Hadron Collider (LHC) is the world's largest accelerator built at Swiss-French border in Geneva, Switzerland. It is also used to accelerate the heavy ion beams. It is capable of accelerating Pb ions with the beam energy of 2.76 TeV/nucleon, which yield to 1.15 PeV in total, with the luminosity of $1.0 \times 10^{27} \text{ cm}^{-2} \text{ s}^{-1}$. Heavy ion beam focuses on study of quantum-chromo-dynamics (QCD), the strong interaction sector of Standard Model (SM). It allows to study physics of strongly interacting matter and the quark-gluon plasma at extreme values of energy density and temperature in nucleus-nucleus collision.

2.8. Medical application

Medical radioisotopes for medical applications are well established for diagnostic and therapy. Ion beams are also being used to produce radioisotopes that are used for the mentioned uses. Further research is also going on to produce high-quality radioisotopes through the series of investigation into production of radioisotopes and its decay characteristics in medical applications such as cross-section measurement of ion beam with target atom to monitor nuclear reactions, compilation of nuclear reaction data for therapeutic radionuclides production, and Beta decay nuclear reaction cross-section measurement for positron emission tomography.

Ion beam therapy is another unique application of ion beam, which provides cutting-edge cancer treatment. Ion beam therapy is a newly emerging treatment for cancer, which is more effective than any other old techniques. In ion beam therapy, ion beam is offering the possibility of excellent dose localization and thus maximizing cell killing within the tumor. Proton therapy for cancer treatment is a matured technology to damage cancer cells while producing the least

damage to the surrounding uninfected tissues. Radiotherapy with carbon ion beam is also developed and is popular in the world, while heavy ion therapy research is going on by understanding fundamental damage mechanisms of cancer cells under heavy ion irradiation [26].

2.9. Nuclear astrophysics

The production of radioactive ion beam and studying its properties are currently a hot research area in accelerator scientific community and for nuclear astrophysicists. Energetic radioactive ion beam, a beam of short-lived nuclei, opens up a new research direction to study nuclear reactions and nuclear structures. Nuclear reaction with radioactive ion beam provides information on reactions that occur at our sun and other stars in our universe. For astrophysics point of view, scientists have produced short-lived halo nuclei in radioactive ion beam facilities to study nuclear astrophysics. Further research is going on for a generation of short-lived neutron-enriched nuclei in next-generation radioactive ion beam facilities, which are required to understand the existence of heavy elements in the universe by the astrophysics rapid neutron-capture process. Through this short-lived radioactive ion beam, it may be possible to explore the secrets of the universe as these nuclei beams play a vital role in understanding the origin of the elements and the dynamics of stellar objects. Moreover, short-lived nuclei (radioactive ion beam) are essential for useful studies of astrophysical objects such as neutron stars, super novae, X-ray bursters, and supernovae. In conclusion, short-lived halo nuclei in radioactive ion beam facilities will provide us with the information that how the chemical elements had formed our world in the cosmos [27].

3. Conclusion

Recent researches in ion beam applications that are mentioned in this introductory chapter are so detailed that it is not possible to cover them in this book. Therefore, this book only has selected special chapters from distinguished authors that cover various aspects of:

1. MeV ion beam applications
2. Focused ion beam applications
3. Ion implantation

Author details

Ishaq Ahmad^{1*} and Fabian I. Ezema²

*Address all correspondence to: Ishaq@ncp.edu.pk

1 National Centre for Physics, Islamabad, Pakistan

2 Department of Physics and Astronomy, University of Nigeria, Nsukka, Nigeria

References

- [1] Ahmad I, Dee CF, Husnain G, Rafique HM, Yan L, Naseem S. The use of high intensity electron beam to form nanohole, induce bending and fabricate nano-contact on a ZnO nanowire. *Micro and Nano Letters*. 2012;**7**:122-124
- [2] Ahmad I, Naqvi SR, Iqbal JI, Lu B, Yan L, Dee CF, Aslam B. Substitutional carbon doping of hexagonal multiwalled boron nitride nanotubes (h-MWBNNTs) via ion implantation. *Journal of Nanoparticle Research*. 2014;**16**:2170-2178
- [3] Bushra B, Shehla H, Madhuku M, Ahmad I, Khan R, Arshad M, Alamgir K, Naseem S, Maaza M. MeV carbon ion irradiation-induced changes in the electrical conductivity of silver nanowire networks. *Current Applied Physics*. 2015;**15**:642-647
- [4] Usman M, Naeem M, Hassan NU, Maqbool M, Iftikhar A, Ahmad I, Zahid H. Structural, optical, and electrical characteristics of AlN:Ho thin films irradiated with 700 keV protons. *Applied Surface Science*. 2015;**357**:179-183
- [5] Ishfaq M, Rizwan Khan M, Bhopal MF, Nasim F, Ali A, Bhatti AS, Ahmad I, Bhardwaj S, Cepek C. 1.5 MeV proton irradiation effects on electrical and structural properties of TiO₂/n-Si interface. *Journal of Applied Physics*. 2014;**115**:174506
- [6] Khan S, Husnain G, Ahmad I, Khan K, Usman M, Saira R. Structural characteristics of Ni-implanted AlN. *Surface Topography*. 2014;**2**:035007
- [7] Shah A, Husnain G, Ahmad I, Arshad M. Cu ions irradiation impact on structural and optical properties of GaN thin film. *International Journal of Modern Physics B*. 2013;**27**:1350020
- [8] Yan L, Zhou G, Ahmad I, Zhou X. Improving the electrical conductivity of multi-walled carbon nanotube networks by H ion beam irradiation. *Carbon*. 2011;**49**:2141-2144
- [9] Ahmad I, Madhuku M, Adeela S, Khan S, Javaid H, Ali A, Wang D, Ilyas SZ, Mola G, Waheed A, Rasheed MA. Tailoring the structural and optical characteristics of InGaN/GaN multilayer thin films by 12 MeV Si ion irradiation. *Materials Science in Semiconductor Processing*. 2017;**64**:95-100
- [10] Husnain G, Yao SD, Ahmad I, Arshad RHM, M M. Characterization of n-GaN dilute magnetic semiconductors by cobalt ions implantation at high-fluence. *Journal of Magnetism and Magnetic Materials*. 2012;**324**:797-801
- [11] Husnain G, Yao SD, Ahmad I, Rafique HM. Structural and magnetic impact of Cr⁺ implantation into GaN thin film. *Solid State Sciences*. 2012;**14**:735-738
- [12] Munroe PR. The application of focused ion beam microscopy in the material sciences. *Materials Characterization*. 2009;**60**:2-13
- [13] Kempson IM, Lombi E. Hair analysis as a biomonitor for toxicology, disease and health status. *Chemical Society Reviews*. 2011;**40**(2011):3915-3940

- [14] Khan R, Khan MAR, Ahmad I, Khan MA, Iqbal T, Ezema FI, Maaza M. Joining of individual silicon carbide nanowires via proton beam irradiation. *Current Nanoscience*. 2018;**14**:1-6. DOI: 10.2174/1573413714666180328153514
- [15] Honey S, Naseem S, Ahmad I, Maaza M, Bhatti MT, Madhuku M. Interconnections between Ag-NWs build by argon ions beam irradiation. *Journal of Nanomaterials & Molecular Nanotechnology*. 2017;**6**:1000213
- [16] Honey S, Ishaq I, Madhuku M, Naseem S, Maaza M, Kennedy JV. Nickel nanowires mesh fabricated by ion beam irradiation-induced nanoscale welding for transparent conducting electrodes. *Materials Research Express*. 2017;**4**:075042
- [17] Shehla H, Naseem S, Ishaq A, Maaza M, Bhatti MT, Wan D. Large scale silver nanowires network fabricated by MeV hydrogen (H^+) ion beam irradiation. *Chinese Physics B*. 2016;**25**:046105
- [18] Shehla H, Ishaq A, Yaqoob K, Javed I, Saira R, Shahzad N, Maaza M. Ion beam irradiation-induced nano-welding of Ag nanowires. *Micro and nano Letters*. 2016;**11**:34-37
- [19] Shehla H, Khan S, Javed I, Madhuku M, Ahmad I, Shahzad N, Maaza M. Protons irradiation induced coalescence of silver nanowires. *Current Nanoscience*. 2015;**11**:792-796
- [20] Ishaq A, Ni Z, Long Yan L, Gong J, Zhu D. Constructing carbon nanotube junctions by Ar ion beam irradiation. *Radiation Physics and Chemistry*. 2010;**79**:687-691
- [21] Ishaq A, Yan L, Zhu D. The electrical conductivity of carbon nanotube sheets by ion beam irradiation. *Nuclear Instruments and Methods in Physics Research B*. 2009;**267**:1779-1782
- [22] Sum TC, Bettiol AA, Kan JA, Watt F, Pun EYB, Tung KK. Proton beam writing of low-loss polymer optical waveguides. *Applied Physics Letters*. 2013;**83**:1707-1709
- [23] Steve R, Robert P. A review of focused ion beam applications in microsystem technology. *Journal of Micromechanics and Microengineering*. 2001;**11**:287-300
- [24] Chih JL, Thomas A, Alexey B. Fabrication of symmetric sub-5 nm nanopores using focused ion and electron beams. *Nanotechnology*. 2006;**17**:3264-3267
- [25] Clark DJ. Accelerators for nuclear physics. *Reports on Progress in Physics*. 1972;**35**:1007-1075
- [26] Hirohiko T. Overview of carbon-ion radiotherapy. *Journal of Physics: Conference Series*. 2017;**777**:012032
- [27] Karlheinz L, Hendrik S. The role of radioactive ion beams in nuclear astrophysics. *Physica Scripta*. 2013;**T152**:014011

We are IntechOpen, the world's leading publisher of Open Access books Built by scientists, for scientists

6,300

Open access books available

171,000

International authors and editors

190M

Downloads

Our authors are among the

154

Countries delivered to

TOP 1%

most cited scientists

12.2%

Contributors from top 500 universities



WEB OF SCIENCE™

Selection of our books indexed in the Book Citation Index
in Web of Science™ Core Collection (BKCI)

Interested in publishing with us?
Contact book.department@intechopen.com

Numbers displayed above are based on latest data collected.
For more information visit www.intechopen.com



Ion-Nanoscale Matter Interactions

Elmuez A. Dawi

Additional information is available at the end of the chapter

<http://dx.doi.org/10.5772/intechopen.76862>

Abstract

Irradiation of spherical gold (Au) nanoparticles confined within a silica matrix with swift heavy ions induces their shaping into prolate nanorods along the beam direction. In this review, spherical colloidal Au nanoparticles with a diameter in the range of 15–30 nm (± 3 nm) are irradiated at normal incidence with Ag ions with a kinetic energy in the range of 18–54 MeV to fluences between 10^{13} and 10^{15} ions/cm² at 300 K. For example, under irradiation with 18 MeV Ag⁺⁴ ions to a fluence of 6.4×10^{14} ions/cm², the originally spherical nanoparticles of 15 nm diameter are shaped into prolate nanorods with a length of 40 nm and a width of 8 nm. An aspect ratio of the major to the minor axis of the nanorods of about 5.0 ± 0.4 at constant volume is achieved. Saturation of the variation of the aspect ratio is reached at a fluence of 8.7×10^{14} ions/cm². Irradiation of samples containing 15 nm Au particles with 25 and 54 MeV Ag ions has shown further lengthening of the Au nanorods, increasing with the increasing ion energy. Similar ion-shaping behavior is reported for 30 nm Au particles under irradiation with 18, 25, and 54 MeV Ag ion energies, respectively. By systematically monitoring the experimental data, we put in evidence the existence of a threshold fluence of Au nanoparticle elongation. The value of the threshold fluence is found to depend on both the ion energy and nanoparticle size.

Keywords: ion beam, electronic stopping, Au nanoparticles, ion track, nanorods, nanowires

1. Introduction

The use of ion beams as effective tools for changing the material properties has gained increasing interest during the past few decades. In particular, emphasis is given to ion implantation [1] and focused ion beam [2] processes which have received an enormous amount of attention in semiconductor technology applications.

When an ion penetrates a solid, it dissipates its kinetic energy in collisions with the target atoms. Ion implantation is performed in the energy regime where electronic stopping dominates the minimal sputtering mechanism. Implanted ion profile and the concentration of impurity atom are affected by sputtering. As the target material is being bombarded with energetic ions, some of the incident beam ions are implanted and retained in the target, while the surface that is exposed to the ion beam is simultaneously receding due to sputtering. Schematic diagram of the ion-solid interaction is illustrated in **Figure 1** (adopted from Nastasi et al. [3]). The basic mechanisms characterizing the interactions of ions with solids can be summarized as follows:

1. Nuclear energy loss. This is the main mechanism of energy losses at low ion velocities (kinetic energy, corresponding to ~ 1 keV/a.m.u.). The bombarding particle transfers its energy to the nucleus of the target atom in elastic collisions, which causes the atoms to be displaced from their equilibrium positions.
2. Electronic energy loss. This is the predominant mechanism of energy loss for fast ions (≥ 1 MeV/a.m.u.). In this regime the ions lose their kinetic energy by electronic excitation and ionization of target atoms.
3. Photon radiation. Stopping through photon generation becomes significant only at relativistic velocities (bremsstrahlung, transitional Vavilov-Cherenkov radiation).
4. Nuclear reactions. Nuclear reactions of the projectile ion and target atoms occur when the two collision partners have sufficient kinetic energy that the Coulomb barrier can be overcome

Taking into account the fact that most attention is paid to ion-induced structural changes of materials within nuclear and electronic energy loss regimes, we shall only discuss the two first mentioned mechanisms of the ion-matter interactions. A good approximation is the assumption that nuclear and electron energy losses are uncorrelated and can therefore be discussed separately and independently.

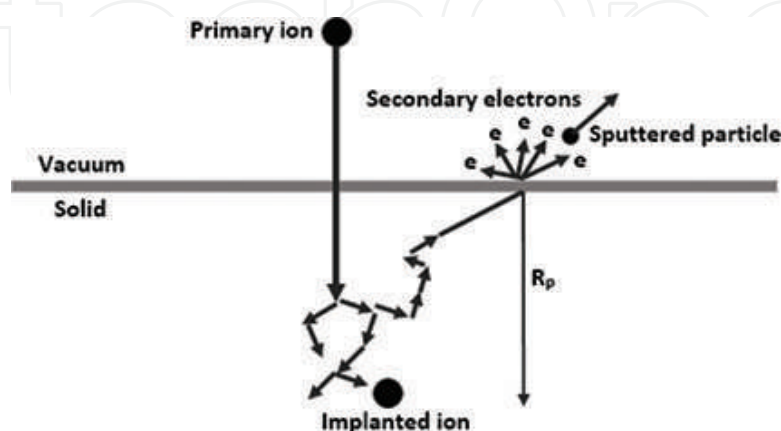


Figure 1. Schematic diagram of the ion solid interactions (adopted from Nastasi et al. [3]).

In the case of nuclear stopping, elastic collisions cause the ions to change their velocity, but the total kinetic energy of the colliding atoms remains constant. On the other hand, inelastic collisions involving electrons are not accompanied by large changes in the direction of the ion, and here several processes are possible: excitation and ionization of atoms with electron exchange in the colliding atoms. A typical evolution of the energy loss as a function of the ion kinetic energy is presented in **Figure 2** for a beam of xenon ions (Xe ions) in amorphous SiO_2 . From the figure, one can, for instance, infer that the electronic stopping power for an energy of 370 MeV is more than two orders of magnitude larger than the nuclear stopping power.

1.1. Ion beam-induced deformation

i. Anisotropic plastic deformation of colloidal silica particles

Heavy ions with $\sim \text{MeV/a.m.u.}$ kinetic energy predominantly lose their energy in a solid target material by electronic excitation and ionization of the target atoms. It is now well established that during irradiation with such ions, amorphous materials are subject to irreversible anisotropic changes of their specimen dimensions [4, 5]. Detailed description of the mechanism governing the anisotropic deformation is reported by the viscoelastic model. The latter presumes the deposition of energy by the incident ion into the electronic subsystem of the material. Through electron-phonon coupling, this energy is transformed in a cylindrical molten-like transient heating around the path of the particles. In a very short time interval (few femtoseconds), and as a result of the cylindrical molten expansion, shear stress relaxation induces freezing anisotropic stress as cooling of the heated regions is taking place. In this way,

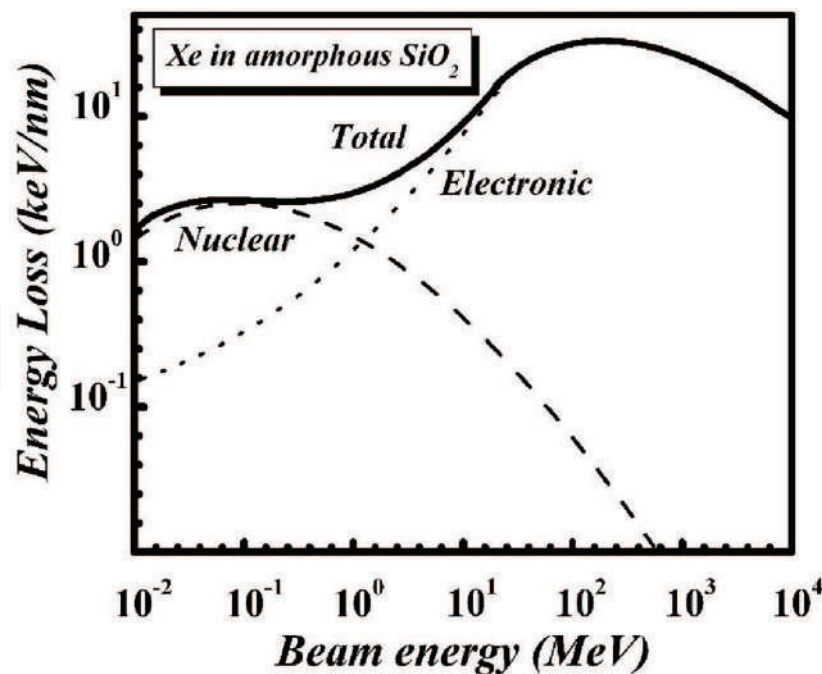


Figure 2. Nuclear, electronic, and total energy loss versus the ion energy for typical ion energy of 370 MeV Xe in amorphous SiO_2 . The figure is reproduced with permission from M. Toulemonde [8].

the deformation mechanism is governed by electronic energy loss and most efficiently with ions in the MeV/a.m.u. energy range. Extrapolation of experimental high-energy to lower-energy data has suggested that the deformation is not expected to occur below a minimum irradiation energy of 1 MeV [6, 7]. The concept of the thermal spike is generally invoked to interpret the damage induced in amorphous materials such as metallic or silica glasses when they are traversed by ions with a kinetic energy in the electronic stopping regime.

ii. Anisotropic plastic deformation of embedded metal nanoparticles

Metal nanoparticles (NPs) are subject of large scientific and technological interest because of their specific properties which are different from those of the corresponding bulk material [9, 10]. When light impinges on (nano)-metal, the free conduction electron clouds respond collectively by oscillating in resonance, which excitation is known as a surface plasmon (SP). For a number of (noble) metals, the resonance behavior is noticeable in a single band in the visible range of the electromagnetic spectrum. One of the interesting aspects is the possibility to shift the surface plasmon resonance (SPR) peak of metal NPs into the infrared region by modifying their aspect ratio [11]. The SPR peak characteristics depend on the size, the shape, and the chemical environment of the metal NP; thus, modification of one of these parameters represents a way to control the optical properties of the material containing the NPs. In this respect, the ion beam-shaping technique is becoming a powerful tool to manipulate matter at the nanometer scale, allowing spherical dielectric particles to be transformed into prolate nanostructures, i.e., to elongate in direction perpendicular to the incident beam direction. Meanwhile, metal NPs embedded within a dielectric matrix are transformed into nanorods and/or nanowires that are aligned along the direction of the incident ion beam [12]. The latter is becoming an increasing scientific interest specially in tailoring the optical properties of plasmonic-active materials which could be widely used in applications within nanophotonics and nanoplasmonics [13].

2. Method

Compared to conventional surface science techniques, such as gas-phase synthesis and deposition of NPs under ultrahigh-vacuum condition, the self-assembly of NPs by means of electrostatic coupling is a scientifically and economically interesting alternative [14]. In the following, charge-stabilized spherical colloidal gold NPs, which have been derivatized with (3-aminopropyl)triethoxysilane (APTES), are deposited on the surface of thermally grown silicon oxide substrates. The thickness of the thermal oxide amounts to 200 nm. Two sets of samples with the different NP size of 15 and 30 nm diameter are prepared. Dispersion in size is deduced from atomic force microscopy (AFM) technique. AFM analysis of the particle heights is measured and found to amount to about ± 3 nm. Each set consists of a number of identically prepared samples for each NP size.

At present AFM is one of the important techniques for analysis of surface morphology [15, 16]. The size and shape of Au NPs have been inspected by a Nanoscope® IIIa tapping mode atomic force microscope (TM-AFM) operating in air. **Figure 3** shows AFM images of Au NPs, distributed on the sample surface after immersion for 5 minutes into a solution containing Au NPs

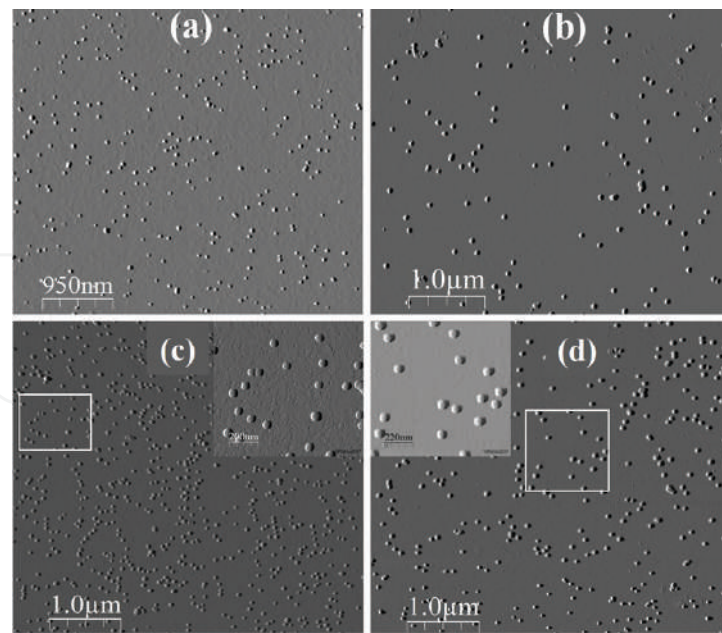


Figure 3. AFM images of 15 and 30 nm Au particles deposited on the SiO₂ surface after immersion into Au solution for 5 minutes, (a) and (b), respectively, and 40 minutes, (c) and (d), respectively.

with 15 and 30 nm diameter (a) and (b), respectively, and after immersion for 40 minutes into Au solution containing 15 and 30 nm diameter NPs, (c) and (d), respectively. These AFM images which were taken before sputter deposition of the second oxide layer show the uniformity of the Au NP distribution over the surface of the samples.

A silicon dioxide layer with thickness of about 150 nm is reactively sputtered to cover the Au NPs. Subsequently, the layer structure is annealed at 900°C in an open furnace. To provide a good thermal contact during the irradiation treatment, the samples are mounted on a massive copper holder using conductive paste. For better understanding of ion energy and NP initial size dependence, irradiations with 18, 25, and 54 MeV Ag ions are performed on the first set of the samples. This first set is composed of three identically prepared NPs of 15 and 30 nm diameter each. The additional set of samples composed of the same NP size is prepared at higher NP areal density as to investigate the role of NP density within the resulting deformation characteristics of embedded NPs. The variation in Au NP areal density is established by variation of the immersion time of the samples into the Au-containing solution, between 5 and 40 minutes. The resulting density of the 15 and 30 nm Au NP samples obtained following the deposition scheme between 5 and 40 minutes is estimated in **Table 1**. The average interparticle distance is calculated based on a square array of particles. The ion beam is electrostatically scanned to homogeneously irradiate the entire sample area of 2 × 2 cm. Irradiations are performed at room temperature (300 K) for fluences ranging from 10¹³ to 10¹⁵ ions/cm² applying normal incidence. Beam currents are sufficiently stable during irradiations as measured on a spot of 1 mm² using a micro-Faraday cup. The beams are delivered by the Utrecht 6.5 MV EN tandem accelerator. The values for the electronic stopping powers in SiO₂ and the projected range of the silver ions in SiO₂ at the energies applied are deduced from the SRIM program [17] and shown in **Table 2**.

Deposition time (± 1 min)	5 minutes	10 minutes	20 minutes	30 minutes	40 minutes
15 nm Au NP concentration (particles/cm ²) ($\pm 10\%$)	2.5×10^9	7.5×10^9	1.4×10^{10}	1.7×10^{10}	4×10^{10}
Interparticle distance (± 10 nm)	200	115	85	76	50
30 nm Au NP concentration (particles/cm ²) ($\pm 10\%$)	—	9×10^8	2.3×10^9	2.8×10^9	3.2×10^9
Interparticle distance (± 10 nm)	—	333	208	188	176

Table 1. NP concentration and the corresponding interparticle distance of Au NPs with average size of 15 and 30 nm diameter deposited on SiO₂ substrate by immersion of the substrate into colloidal Au-containing solution for time intervals of 5, 10, 20, 30, and 40 minutes.

These ranges are far beyond the thickness of the oxide layers containing the metal nanoparticles. Hence, the irradiation is only used to deposit energy into the SiO₂-Au layers. The Au nanoparticle size and shape before and after irradiation are studied by using (tapping mode) atomic force microscopy (AFM), Rutherford backscattering spectrometry (RBS), and transmission electron microscopy (TEM).

Analysis of the samples has been carried out by different techniques. Rutherford backscattering spectrometry (RBS) is used to measure the density of Au species as it penetrates into the SiO₂ matrix. With respect to the latter, RBS is regarded as a faster tool to bring information about Au NP depth distribution before and after irradiation with heavy ion beams. The depth distribution of the Au NPs is estimated from the corresponding full width at half maximum (FWHM) of the Au peak in the RBS spectra. It is worth mentioning that under swift heavy ion (SHI) irradiation, the vast majority of the Au species will not be confined to their NPs due to melting; therefore, the FWHM of the Au peak cannot bring qualitative estimation of the exact NP size. However, a qualitative trend of the NP elongation can be followed. RBS analysis was carried out applying an incident ⁴He⁺ ion beam with energy of 2 MeV at normal incidence geometry. The backscattered ions were analyzed in situ using two detectors at angles of 120° and 170°, respectively. In the “Results” section, we will only discuss the data analysis obtained from one detector of our selection (120° detector), assuming that the data obtained from the 170° are essentially identical. After RBS analysis, samples containing the metal NPs are analyzed by transmission electron microscope (TEM) for cross-sectional imaging of the size and shape of Au NPs before and after irradiation. For that purpose, a 300 keV Philips/CM30 microscope is used. The micrographs obtained from X-TEM analysis are processed with a slow scanning camera applying digital micrograph program.

	S_e (SiO ₂) (keV/nm)	S_n (SiO ₂) (keV/nm)	S_e (Au) (keV/nm)	S_n (Au) (keV/nm)	R_p (μm)
18 MeV ⁺⁴	5.4	0.23	11	0.9	5.8
25 MeV ⁺⁵	6.7	0.18	14	0.7	6.9
54 MeV ⁺⁸	9.7	0.10	24	0.4	10.3

Table 2. Values for electronic (S_e) and nuclear (S_n) stopping power for SiO₂ and gold and projected range (R_p) obtained for the applied ion beams (18, 25, and 54 MeV Ag ions). All the values are obtained using the code SRIM 2008 [17].

3. Results

Au NPs with average size of 15 and 30 nm diameter are prepared with different NP concentrations and/or areal densities (10^8 – 10^{10} particles/cm²) embedded within a single plane parallel to the surface of a SiO₂ matrix. In this section, we will report a detailed investigation of swift heavy ion irradiation effects on these NPs. A selective range on incident ion energy of 18, 25, and 54 MeV Ag ions is applied. Influence of the ion energy, NP size, and areal density on the process of ion-induced elongation of spherical Au NPs will be discussed. For clarity of presentation, the “Results” section is divided into two subsections. The first subsection discusses the role played by embedded NP size and ion energy within the deformation characteristics at almost constant NP areal density and/or concentration. For that purpose, NP size range between 15 and 30 nm diameter is selected of which its samples are identically prepared and successively irradiated with ion beam energies in the range of 18–54 MeV Ag ions. In the second subsection, for the two NP sizes, the ion beam-induced deformation is investigated considering two extreme regions of NP areal density (low concentration and high concentration) applying single ion energy of 54 MeV Ag⁺⁸ ions.

3.1. Elongation as a function of the initial NP size and the ion beam energy

3.1.1. Evolution of 15 nm Au NPs

The first set consisting of three identically prepared samples, containing 15 nm Au NPs with an average areal density amounting to 1.7×10^{10} particles/cm², is irradiated with 18, 25, and 54 MeV Ag ions, respectively. **Figure 4a–c** shows the Au RBS peak as obtained from the 120° detector for several fluence values for the three energies. The relatively sharp peak of the unirradiated regions corresponds to 15 nm particles which are embedded in a SiO₂ matrix in a plane at a depth of approximately 150 nm below the surface. RBS analysis in **Figure 4a–c** shows broadening in Au NP peak with increasing the irradiation fluence. The broadening in the Au RBS peak indicates that the depth distribution of the Au is penetrating into the hosting SiO₂ matrix. The latter indicates that the pristine Au NP is transformed into aligned nanorods parallel to the ion beam direction. The evolution of the FWHM with fluence from the 120° and 170° detectors is shown in **Figures 5(a)** and **5(b)**, respectively.

From inspection of the data in both figures, two facts are deduced for irradiations of 15 nm Au NPs with 18 and 25 MeV Ag ions, as follows:

- i. No elongation appears for fluences lower than $\sim 5.0 \times 10^{13}$ and 3.0×10^{13} ions/cm², respectively.
- ii. The RBS peak width reaches saturation for fluences larger than ~ 6 – 8×10^{14} and 4.5×10^{14} ions/cm², respectively.

The X-TEM micrographs in **Figure 6a, b** correspond to the highest 18 MeV irradiation fluence (8.7×10^{14} ions/cm²). Clearly, under 18 MeV Ag⁺⁴ ions, the originally spherical NPs of 15 nm diameter are all shaped into prolate nanorods with a length of ~ 40 nm and a width of ~ 8 nm, thus, with an aspect ratio of about 5. The volume of each nanorod corresponds approximately

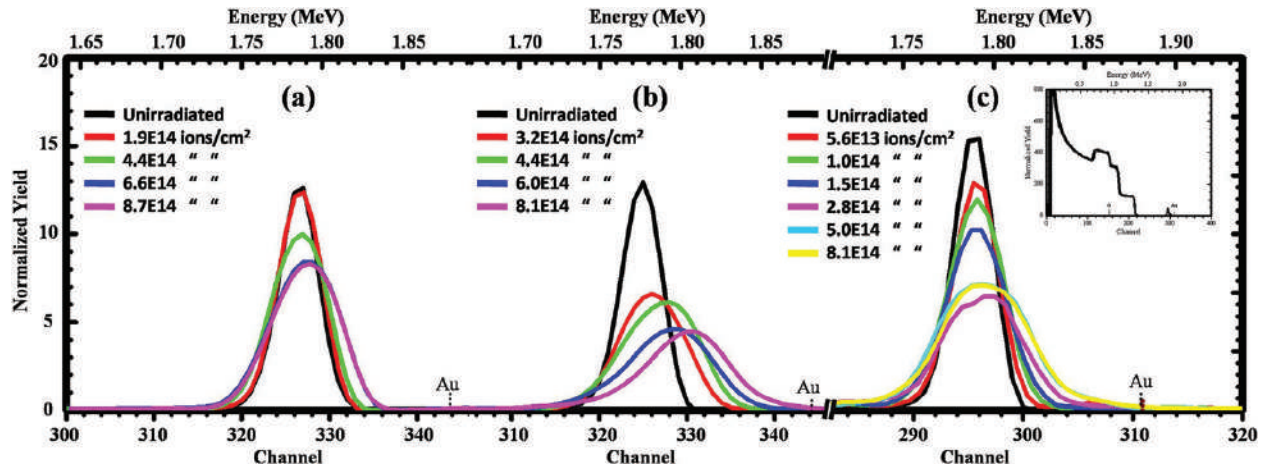


Figure 4. Normalized RBS spectra of three identically prepared samples containing Au NPs with 15 nm diameter with an average areal density of 1.7×10^{10} particles/cm² after being irradiated with energies of 18 MeV Ag⁺⁴ ions, 25 MeV Ag⁺⁵ ions, and 54 MeV Ag⁺⁸ ions, (a), (b), and (c), respectively. The inset shows total normalized spectra for all samples. The Au surface channel is indicated. The scale is (a), and (b) is the same; however, for (c), the experimental condition is slightly different.

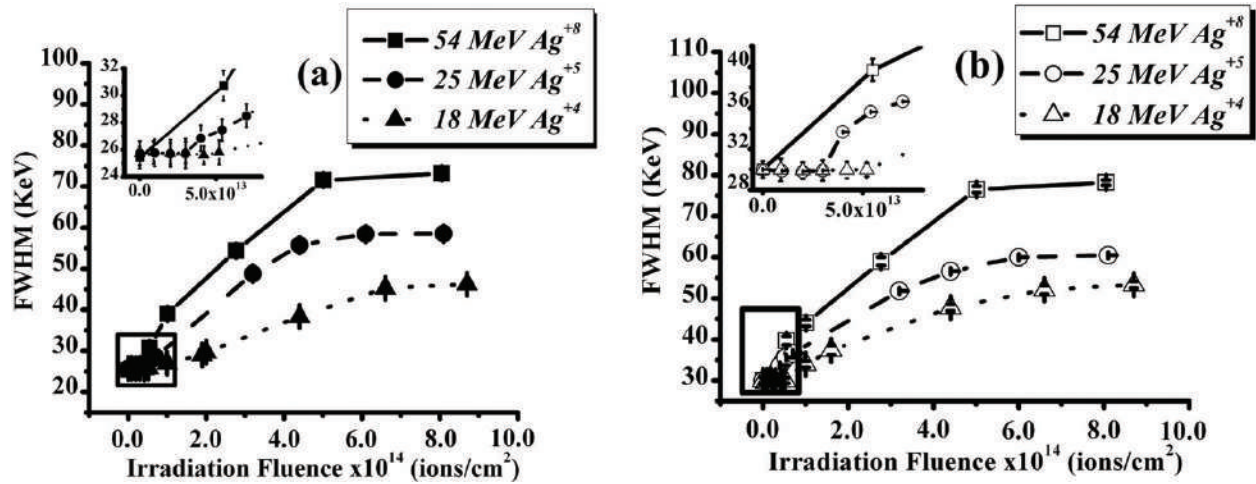


Figure 5. The FWHM of the Au peak as function of irradiation fluence determined simultaneously for the 120° and 170° scattering angles, (a) and (b), respectively. The figures are for 15 nm Au NPs irradiated with 18 MeV Ag⁺⁴ ion energy (triangles and dot line), 25 MeV Ag⁺⁵ ion energy (circles and dash line), and 54 MeV Ag⁺⁸ ion energy (squares and solid line). A magnified view of the region identified by the black square and the black rectangle is included in the inset of figure (a) and (b), respectively.

to that of the pristine spherical NP ($V_{NR} \sim V_{NP}$). This indicates that the ion-shaping process for these irradiation conditions is an individual process, i.e., each NP deforms into a similar prolate nanorod.

The broadening of the Au RBS peak for the sample irradiated with 54 MeV Ag⁺⁸ ions is also represented in **Figure 5a, b**. At this energy the elongation of 15 nm Au particles starts without detectable threshold fluence in these measurements. After irradiation to a fluence of 1.0×10^{14} ions/cm², the broadening of the Au RBS peak has already reached the value attained under irradiation with 18 MeV Ag⁺⁴ ions to the maximum fluence of 8.7×10^{14} ions/cm². The latter observation confirms the influence of the ion energy on the elongation characteristics of Au NPs.

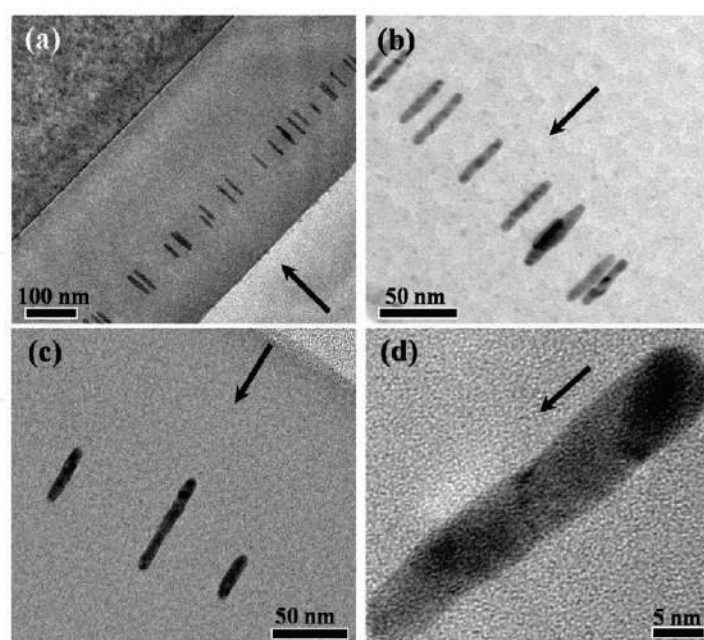


Figure 6. High-resolution X-TEM images of (i) 15 nm Au NPs under 18 MeV Ag^{+4} ions to a fluence of 8.7×10^{14} ions/cm² (a) and (b). (ii) 15 nm NPs under 54 MeV Ag^{+8} ions to a fluence of 1.0×10^{14} ions/cm² (c) and (d). The direction of the ion beam is indicated by the black arrows.

Strikingly, X-TEM micrographs corresponding to the irradiation with 54 MeV Ag^{+8} ions to a fluence of 1.0×10^{14} ions/cm² reveal almost similar nanorod morphology as those given in **Figure 6a, b**. These micrographs are given in **Figure 6c, d** showing aligned Au nanorods of approximately 40 nm length and ~8 nm width parallel to the ion beam direction. With increasing the irradiation fluence above 1.0×10^{14} ions/cm², the Au RBS peak continues to broaden until its width becomes constant for fluences larger than 5.0×10^{14} ions/cm².

3.1.2. Evolution of 30 nm Au NPs

A second set of three identically prepared samples containing 30 nm Au NPs with a areal density of about 2.8×10^9 particles/cm² are irradiated with 18, 25, and 54 MeV Ag swift heavy ions. The series (a–c) in **Figure 7** represents the evolution of the Au RBS peak with irradiation fluence at these energies. **Figure 8** shows the change in FWHM with fluence derived from the RBS spectra for the three energies using the 120° detector. From the figure, two facts are deduced similar to the case for 15 nm Au NPs under irradiations with 18 and 25 MeV Ag ions, as follows:

- i. Elongation threshold fluences are observed, amounting to about 7.0×10^{13} and 5.0×10^{13} ions/cm², respectively.
- ii. Saturation in FWHM of the Au RBS peak is reached at fluences 6.0×10^{14} and 5.0×10^{14} ions/cm², respectively.

For irradiation with 54 MeV Ag^{+8} ions, the ion-shaping effect starts again without detectable threshold fluence. At the same time, no saturation is visible up to a fluence 2.0×10^{14} ions/cm².

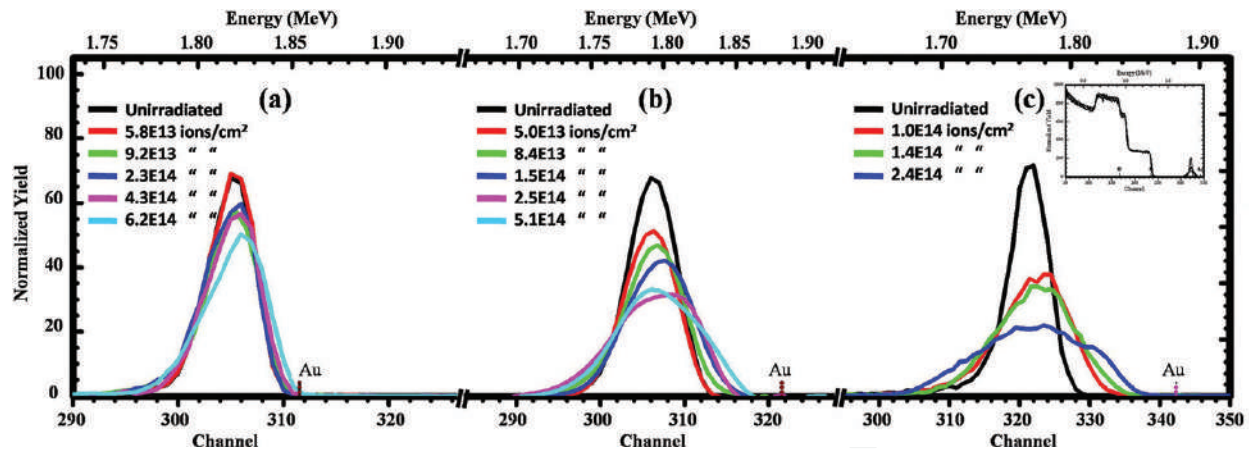


Figure 7. Normalized RBS spectra of 30 nm Au particles under (a) 18 MeV Ag^{+4} ions, (b) 25 MeV Ag^{+5} ions, and (c) 54 MeV Ag^{+8} ions for samples prepared with an average areal density of 2.8×10^9 particles/ cm^2 .

AFM analysis in **Figure 3** points to a good uniformity of Au NP distribution over the surface and the absence of agglomeration, i.e., clustering of individual NPs. This allows us to investigate the role of interparticle distance on the ion-shaping mechanism. Thus, in the following subsection, we will focus on the elongation phenomenon by varying the initial areal density of the Au NPs.

3.2. Elongation as a function of the initial NP size and initial NP concentration

3.2.1. Evolution of 15 nm Au NPs

Samples containing spherical Au NPs with diameter of 15 nm prepared with areal density between 0.25 and 4×10^{10} particles/ cm^2 were irradiated with 54 MeV Ag^{+8} ions. The series

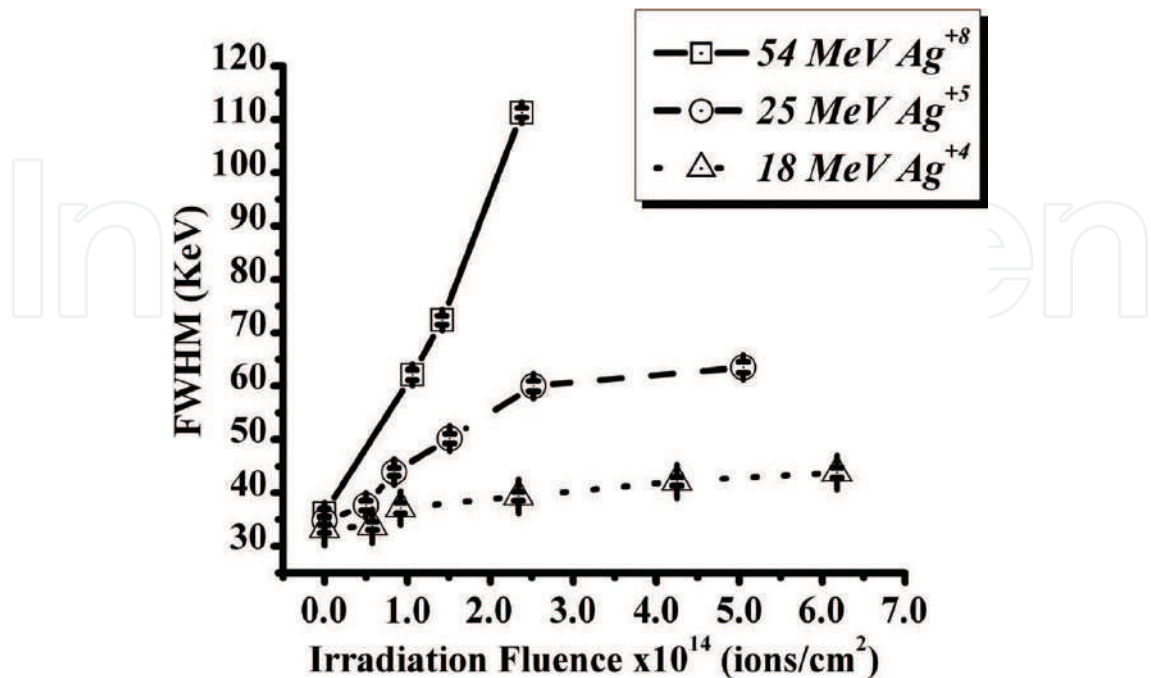


Figure 8. The relative change of Au peak width determined for the 120° scattering angle as a function of fluence for 30 nm Au particles under irradiation with 18 MeV Ag^{+4} ions (triangles and dot line), 25 MeV Ag^{+5} ions (circles and dash line), and 54 MeV Ag^{+8} ions (squares and solid line).

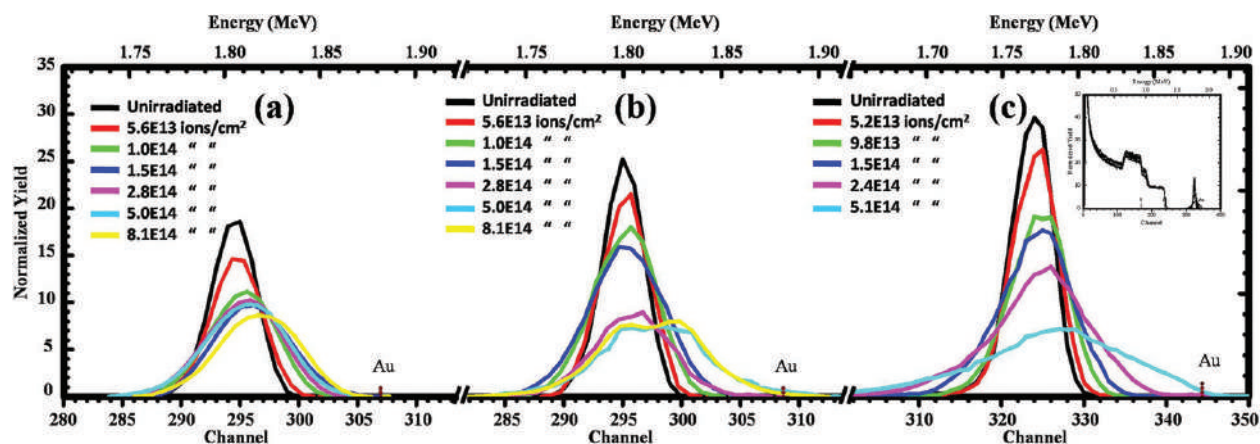


Figure 9. The Au RBS peak of 15 Au NPs for various irradiation fluences of 54 MeV Ag^{+8} ions for different areal densities of 2.5×10^9 , 1.4×10^{10} , and 4×10^{10} particles/cm², (a), (b), and (c), respectively. Normalized RBS spectra are presented in the inset of plot (c).

(a–c) in **Figure 9** show the 15 nm Au RBS peak for various fluences for NP at areal density of 2.5×10^9 , 1.4×10^{10} , and 4×10^{10} particles/cm², respectively. **Figure 10** shows the evolution of the FWHM of the RBS Au peak as a function of the fluence, for various values of the areal density. From the inspection of the figure, two regions clearly appear as follows: (i) For low irradiation fluences, the relative broadening of the RBS peak is almost the same for all samples irrespective of their areal density. We define this region as A. (ii) Above a critical fluence of about $1\text{--}2 \times 10^{14}$ ions/cm², the broadening of the RBS peak becomes significantly a function of the NP areal density. This region is denoted as region B. Apparently, all the curves tend to evolve toward a saturation value. The larger the initial NP areal density, the larger the saturation value of the FWHM appears to be.

We presume that in region A, Au NPs elongate into nanorods conserving their original volume ($V_{\text{NR}} \sim V_{\text{NP}}$). This is confirmed by X-TEM analysis as is shown in **Figure 11a–d**. To understand correlations between NP areal density and/or concentration and the broadening within the Au RBS peak observed in region B in **Figure 10**, we have selected two X-TEM micrographs of extreme NP densities (lower/higher) for comparison. As for the lowest NP density of 2.5×10^9 particles/cm², TEM micrographs in **Figure 11a, b** which correspond to irradiation fluence of 8.0×10^{14} ions/cm² is shown. The X-TEM micrograph in this figure shows aligned Au nanorods with major to minor axes of 100.8 nm. Calculation of the corresponding volume of these nanorods indicates that the volume for each nanorod is about twice the volume of the original pristine NP ($V_{\text{NR}} \sim 2V_{\text{NP}}$). Then, we consider the TEM micrographs corresponding to the highest areal density (4×10^{10} particles/cm²) at a fluence of 5.0×10^{14} ions/cm² (see **Figure 11**). These micrographs are given in **Figure 11c–e** and show long nanowires with their major axis varying from 150 to 180 nm and minor axis of 8 nm. It is obvious that these wires are not the result of the deformation of a single particle because their Au content exceeds that of the initial NPs by at least a factor of 5 to 6, i.e., $V_{\text{NR}} \sim (5\text{--}6) V_{\text{NP}}$. We attribute that multiple Au NPs must have contributed to the growth of such nanowires. Seemingly, under swift heavy ion irradiation, some NPs deliver their species by disintegration, and through lateral transport, the disintegrated particles contribute to the growth of other particles. In this way, further lengthened nanostructures will appear in account of shorter ones. The latter hypothesis has been confirmed by X-TEM analysis where we observed smaller aligned particles, likely resulting from the fragmentation of some

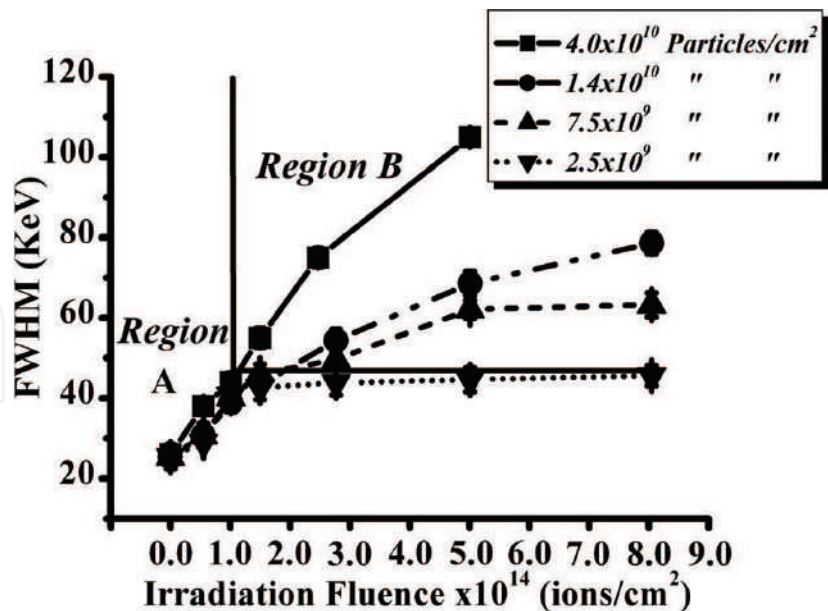


Figure 10. The FWHM of Au RBS peak obtained from the 120° detector as a function of 54 MeV Ag⁺⁸ irradiation fluence for different areal densities of 15 nm Au particles.

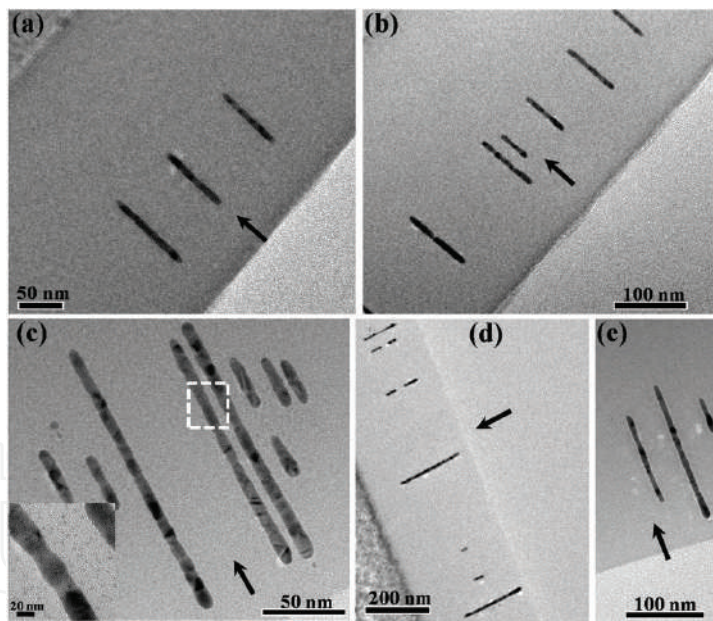


Figure 11. HR-XTEM images of (i) 15 nm Au particles with initial areal density of about 2.5×10^9 particles/cm 2 after irradiation with 54 MeV Ag⁺⁸ ions to a fluence of 8.1×10^{14} ions/cm 2 , (a) and (b), respectively. (ii) 15 nm Au particles with an initial areal density of 4.0×10^{10} particles/cm 2 irradiated with 54 MeV Ag⁺⁸ ions to a fluence of 5.0×10^{14} ions/cm 2 , (c), (d), and (e), respectively. The direction of the ion beam is indicated by the black arrows.

ion-deformed nanorods or nanowires. It emerges that the variation of NP areal density, and the concomitant variation of the interparticle distance, results in a strong variation in the shaping characteristics of the spherical Au NPs. For the areal density larger than 2.5×10^9 particles/cm 2

and above the critical fluence of 1.0×10^{14} ions/cm², Au NPs start to disintegrate, while others continue to grow by accumulation of atoms and/or fragments from the disintegrating particles. The latter is assumed to occur by means of a process that is well known as Ostwald ripening. Interestingly, in some regions of TEM micrographs, tiny satellite particles surrounding shorter particles were seen (inset of **Figure 11c**). These satellite particles were not visible before irradiation. It is clear that the relative increase in Au peak width of the lowest areal density sample has already attained its maximum value just above the critical fluence. This might imply that there exists a threshold areal density for nanowire formation for 15 nm diameter Au particles, at an areal density of $\sim 5.0 \times 10^9$ particles/cm², under 54 MeV Ag⁺⁸ ion irradiation. This corresponds to an interparticle distance of about 150 nm. Presumably, the mass transport process is effectively limited by a too large distance between the Au NPs.

3.2.2. Evolution of 30 nm Au NPs

Au NPs having an average diameter of about 30 nm and areal density ranging between 0.9 and 3.2×10^9 particles/cm² were irradiated with 54 MeV Ag⁺⁸ ions up to a fluence of 5.0×10^{14} ions/cm². The Au RBS peaks and the evolution of the FWHM of Au peak with the fluence for each NP areal density are shown in **Figure 12a–c** and **Figure 13**, respectively.

Again, we report the existence of two separated regions as in **Figure 10**. At lower irradiation fluences, the Au NP broadening evolves the NP size (region A). However, for fluences larger than a certain value (estimated for this NP size of about 1.0×10^{14} ions/cm²), the broadening in Au NPs in region B evolves the NP areal density. As can be seen in **Figure 14a, b**, X-TEM micrographs show Au nanowires of a length of about 150–200 nm and a width of 8 nm aligning as a result from irradiation of the 30 nm Au NPs with areal density of 3.2×10^9 particles/cm² with 54 MeV Ag⁺⁸ ions to a fluence of 5.0×10^{14} ions/cm² (see **Figure 3.5**). From the data in this figure, we deduce a threshold interparticle distance near 250 nm for nanowire formation, i.e., at an areal density of approximately 9.0×10^8 particles/cm².

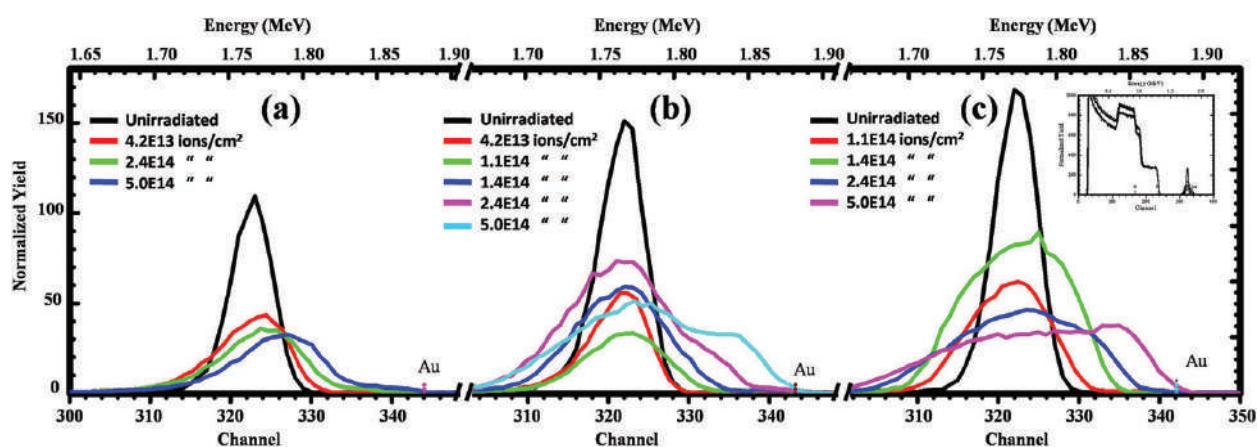


Figure 12. The Au RBS peak of 30 Au NPs for various irradiation fluences of 54 MeV Ag⁺⁸ ions for different areal densities of 9.0×10^8 , 2.8×10^9 , and 3.2×10^9 particles/cm², (a), (b), and (c), respectively. Normalized RBS spectra are presented in the inset of plot (c).

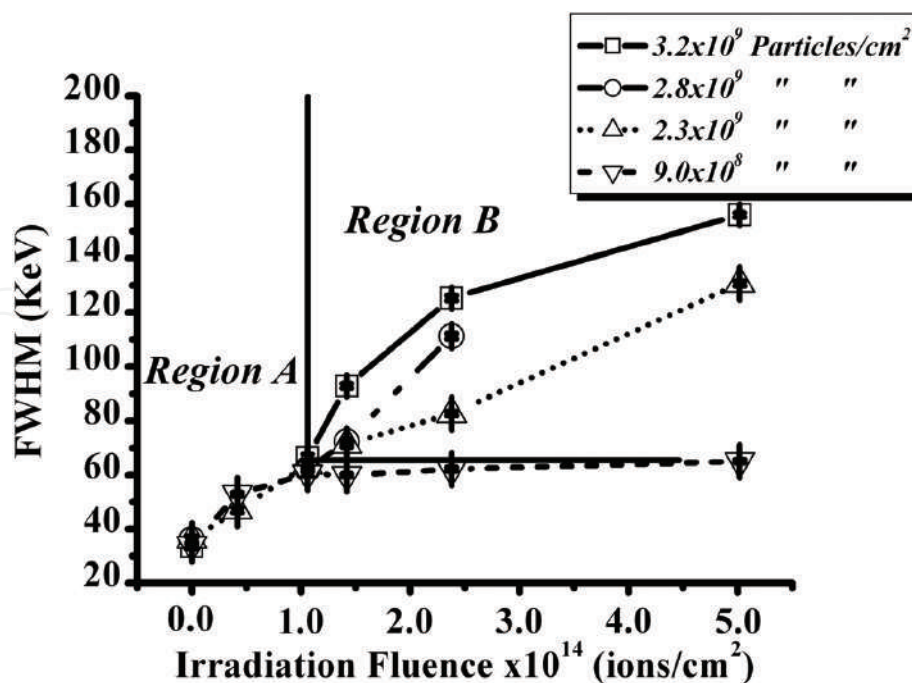


Figure 13. The FWHM of Au RBS peak obtained from only the 120° detector as a function of 54 MeV Ag⁺⁸ irradiation fluence for different areal densities of 30 nm Au particles.

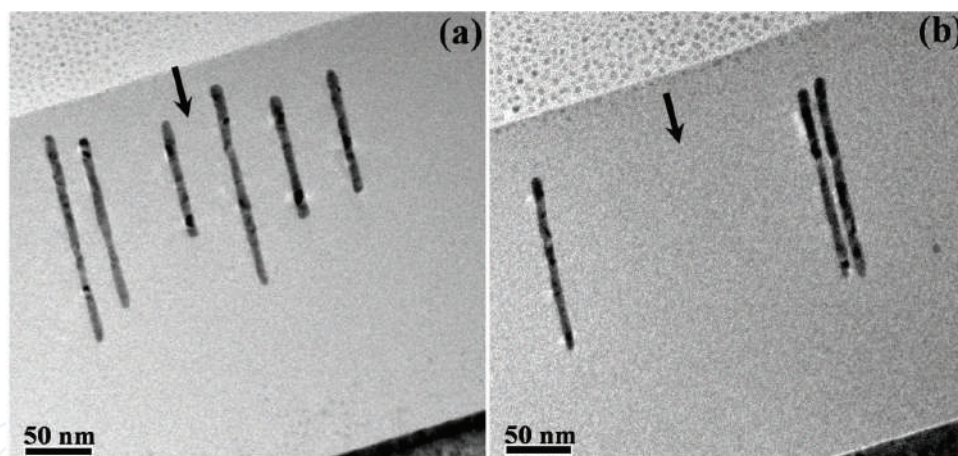


Figure 14. HR-XTEM images of 30 nm Au particles with initial areal density of 3.2×10^9 particles/cm 2 irradiated with 54 MeV Ag⁺⁸ ions to a fluence of 5.0×10^{14} ions/cm 2 , (a) and (b), respectively. The direction of the ion beam is indicated by the black arrows.

4. Discussion

As pointed out in the experimental section, the projected ranges of the ions at the applied energies are far beyond the location of the spherical Au NPs. Thus, the elongation of such metal NPs must be a result of the ion passage through the SiO₂-Au-containing layer.

Systematic investigations of the deformation of NPs in response to swift heavy ion (SHI) irradiation have allowed us to evidence experimentally the existence of a threshold fluence for elongation, Φ_c . The threshold fluence for elongation as a function of ion energy and NP size

for 15–80 nm Au particles is estimated in **Table 3**. The value of Φ_c has been observed to depend on both ion energy and pristine NP size. In particular, Φ_c decreases with increasing electronic stopping power and increases with the NP diameter. However, as suggested by Klaumünzer [18, 19] and successively experimentally shown by Penninkhof et al. [20, 21], irradiation-induced NP elongation is a complicated issue where both the matrix and the characteristics of the confined NPs play an active role. Here, we put forward three possible mechanisms that could be the origin of the existence of a threshold fluence and its variation with NP size and incident ion energy. These mechanisms are listed as followed:

- i. Preparation methodology of the samples.
- ii. The compaction of the hosting silica matrix under irradiation.
- iii. Occurrence of the irradiation-induced stresses within the silica matrix constrained by a substrate.
- iv. Following the process at which our samples are prepared, Au NPs are first assembled on top of a thermally grown SiO_2 film and subsequently confined by sputtering of a secondary layer of SiO_2 that is reactively sputtered on top of the first layer. The final configuration of the active region of the samples indicates that Au NPs are embedded in a single plane 200 nm far from the surface of the sample. Chemically, gold is known to have a fairly poor wetting affinity with the SiO_2 . Consequently, the mechanism of how precisely the oxide layer is formed around the Au NP during the deposition process is basically unknown. Following the process, our SiO_2 top film is grown at zone 1 at the low adatom mobility growth mode [22] and relatively low ion bombardment energy [23]. Within this sputtering scheme, most likely voids will form near the lower half of the NP in the growing oxide. The latter is attributed due to shadowing effects. On the other hand, during X-TEM analysis, none of the aforementioned voids were imaged. Therefore, it is plausible that a certain compaction of the SiO_2 surrounding the NP is required before the deformation process is activated.
- v. It has been mentioned in literature that under irradiation with swift heavy ions at low fluences, the SiO_2 matrix exhibits a compaction of about 3%. At higher irradiation fluences, an anisotropic growth dominates the compaction phase [24–27]. Rearrangement of the SiO_2 ringlike material into smaller compact ring volume leads to densification of the silica matrix [28, 29]. For swift heavy ion irradiation, within each individual cylindrical ion track, the virgin material density is irreversibly modified. Subsequent ion impact within the same region does not produce any further density changes [24]. In this view, the fluence required to achieve

Ion energy	Nanoparticle size (nm)	Threshold fluence (ions/cm ²)
18 MeV Ag ⁺⁴	15	5×10^{13}
25 MeV Ag ⁺⁵		3×10^{13}
18 MeV Ag ⁺⁴	30	7×10^{13}
25 MeV Ag ⁺⁵		5×10^{13}

Table 3. The threshold fluence for elongation as a function of ion energy and NP size for 15–80 nm Au particles.

the compaction corresponds slightly to a compromise where all incident neighboring tracks exhibit mutual overlap in such way that the perturbed area covers the overall sample surface.

- vi. As mentioned in our experimental part, our grown silica film is not free standing films but constrained by underneath silicon substrate. The stress state of a constrained silica film as an effect of the ion irradiation has been intensively studied in literature [25–27]. Two extremely opposite stress situations depending on the irradiation fluence have been reported as follows: (1) under irradiation at low ion fluences, the initially compressive stress turns into a tensile stress. The latter, which is related to the mechanism of compaction, leads to the structure to a higher equilibrium density state. The maximum value for this equilibrium is reached at the end of the matrix densification for fluences up to few 10^{13} ions/cm². (2) Under irradiation with fluences larger than 10^{14} ions/cm², anisotropic material deformation becomes quiet prominent in the further evolution of the system. The latter effect is associated with the tensile stress reduction and the buildup of a compressive stress for the constrained film.

Considering mechanisms (i) and (ii), we presume that the NP elongation is limited to the accomplishment of the structural transformation of the silica matrix. With the latter in mind, we try to correlate the threshold deformation evolution with the energy of the incident ions. As the end of SiO₂ matrix compaction implies the situation whereas the sample surface becomes entirely covered by the mutually overlapping ion tracks, it is conceivable that the resulting deformation threshold depends on the incident ion track diameter. In that sense, the larger the track radius is, the lower the deformation threshold fluence will be. In literature, a number of experimental and theoretical publications have already reported on the ion track cross sections in SiO₂ matrix [30–33]. In these publications, the track size is calculated from the thermal spike model and already found to correspond to the region that melted in the wake of the passing heavy projectile [34]. In our current results, the applied ion energies of 18, 25, and 54 MeV Ag, the corresponding electronic stopping powers in SiO₂ amount to 5.4, 6.7 and 9.7 keV/nm). The corresponding track diameters for these energies in the silica are approximately 3, 4, and ~5 nm, respectively. The calculated corresponding complete overlap of the ion tracks at the surface of the sample is found at fluences of 2.0×10^{13} , 1.0×10^{13} , 0.7×10^{13} , and 0.5×10^{13} ions/cm², respectively.

Putting on mind that (i) the swift heavy ion irradiation follows random statistics and that (ii) the compaction fluence for a silica matrix containing partially wetted metallic NP can be different from that of pure silica film, our calculations account pretty well for the reported reduction of the deformation threshold when the incident ion energy is increased.

In our results, we show that the inertia against NP elongation increases with size. In other words, NPs with larger diameters require higher electronic stopping powers to be deformed. Since the macroscopic stress induced by heavy ion irradiation in planar constrained films can reach larger values (several hundreds of MPa) [26], we presume that that mechanism (iii) can actively participate in deformation process of the embedded Au NPs. The aforementioned scenario of (iii) has already been introduced by Roorda et al. [12] for verification of the shape change of Au NPs confined within a silica shell and suggested to remain solid during the irradiation. However, this indirect mechanism alone is not enough to correlate the observed deformation of embedded solid NPs [18]. The metallic NP must have an active participation in the elongation process. In other words, the elongation process will only take place when

the temperatures of both the metallic NP and the surrounding dielectric matrix exceed their individual melting temperatures [18, 19]. In literature, it has been argued that the melting of metallic NPs with diameters in the range of nearly similar range to our NPs of the current study (6 and 20 nm) cannot be invoked with energy deposition corresponding to the electronic stopping powers in the current work [35]. Particles with relatively larger diameters are not expected to completely melt and virtually are not observed to deform under SHI irradiation, [18, 35, 36]. Awazu et al. [35] report that Au NPs with diameter of about 50 nm are not subject to deform under irradiation with 110 MeV Br ions to a fluence of about 1.0×10^{14} ions/cm². For this class of NP size, it is conceivable that a minimum compressive stress is needed to activate the NP deformation. On the other hand, it is necessary to mention that the threshold fluence cannot be directly regarded to the individual track-generated stress [37–39]. This is because the deformation threshold would be only dependable on the electronic stopping. Consequently, macroscopic stress should be invoked to clarify the observations. In this sense, direct correlation between minimum compressive stress and NP size could be established. The larger NP size requires larger (minimum) compressive stress to activate the NP elongation process leading to larger fluence necessary to reach it. The latter hypothesis accounts quiet well for our results for the deformation dependence on initial NP size, ion energy, and irradiation fluence. Furthermore, the variation of the embedded NP areal density has led to identification of two distinct fluence regimes for the NP elongation under swift heavy ion irradiations as follows:

- i. For low irradiation fluences, Au NPs deform into ion beam-aligned nanorods. This morphology transformation occurs under volume conservation. In other words, the ion-shaping mechanism is an individual mechanism, where each pristine NP deforms into a single oblate nanorod. As this behavior is observed for all values of the NP areal density, in this first stage which is represented by the region A, the ion-shaping process can be seen as an *individual process* as far as the nanoparticles are concerned.
- ii. For irradiation fluences above—somewhat critical threshold—of 1.0×10^{14} ions/cm², RBS analysis indicates that the deformation rate is sensitive to the initial NP areal density. With increasing the NP areal density, the deformation rate increases. In this deformation's secondary stage, high-resolution TEM images show long Au nanowires aligned in direction of the ion beam accompanied by strong signs of Au disintegration and/or fragmentation. As the volume of the longer nanowires visualized is about five to six times the volume of the originally spherical NP, the NP elongation process in this fluence-dependent region necessitates the contribution of several individual nanostructures. Within this fluence region, the elongation process might be identified in terms of a *collective process* where some of already-deformed NPs, or even some of the aligned nanowires, dissolve under the irradiation, while other nanowires continue to grow by integration of the atoms from the dissolving particles. The mechanism behind the driving force identifies which nanowire should dissolve and which nanowire should grow remain unknown. Consequently, there is a need for more detailed experimental and theoretical approach to verify it.

The mechanism governing the growth of Au nanowires most likely involves the diffusion through the silica matrix of the gold solute from the dissolved/fragmented nanoparticles toward the growing ones. The task to identify the physical origin of the driving force for preferred Au diffusion from shorter Au nanorods to longer ones, which causes a kind of Ostwald ripening, is difficult.

Some insights can be obtained from **Figure 11(c)** (the inset) and **Figure 14a, b** where small fragments are clearly visualized. In fact, those small fragments were not imaged before irradiation; thus, they must be a product of the ion beam irradiation. The energy deposited within the NP subsystem may have allowed the Au atoms and/or species to dissolve in silica. Upon local fluctuation of the solute concentration, the supersaturation of the solid solution then evolves toward the precipitation of the satellite particle phase. Under swift heavy ion irradiation, these small precipitates become unstable [40], and thus they dissolve by subsequent impinging ions (track by track) through the silica matrix. In other words, the diffusion of such nanostructures is driven by the transient melted region formed in the wake of the impinging ions. Dais et al. [41] report on direct observation of the gold diffusion within the ion track. As this process depends on the amount of the available solute sources, i.e., the NP concentration, the lower their relative distance the shorter the diffusion time and the longer the nanowires, as shown in **Figure 13c, d** and **Figure 14a, b**. On the other hand, when the NP areal density is low, the particle growth is limited by the too long distance between the metal particles. This effect accounts for the relatively low saturation length observed in the samples having the lowest NP areal density. If metal solute may diffuse only within the thermal spike region, for each ion impact, the lateral diffusion distance will be of the order of magnitude of the track size. In the current study, the calculated ion track radius corresponding to the applied ion energies ranges between 3 and 5 nm. Considering the minimum calculated interparticle distance of NPs of about 50 nm, and assuming that the minimum fluence needed for the sample surface overlap is about 1.0×10^{13} ions/cm², approximately ten ion impacts within the region are necessary to diffuse over 50 nm. Therefore, the minimum fluence required for solute metal atoms to diffuse from one particle to the nearest one is about 1.0×10^{14} ions/cm². The latter accounts quite well with the fluence necessary to pass from the individual deformation region (*denoted as A*) to the collective deformation process region (*denoted as B*) in our results.

Thus, the possibility to grow Au nanowires under swift heavy ion irradiation requires basically the possibility for original NPs to deform and the availability of short-distance solute sources to achieve an effective mass transport. It seems further required that the particles have a certain nanorod shape before the nanowire region is entered or that, alternatively, a certain fluence is applied to enter this region. For Au NPs larger than 30 nm diameter, the mechanism governing nanowire creation requires greater total energy deposition than the value applied here. We note a tendency that the elongation rate diminishes at a higher nanorod length for a higher areal density. For Au NPs of 15 and 30 nm diameter and with increasing irradiation fluence, the minor axis of the elongated nanorods reaches a saturated width at 8 nm. Much in standing with, Giulian et al. [36] report on the elongation process of Pt NPs with size of about 7 nm diameter in a SiO₂ matrix. In this study, the minor axis of the elongated Pt NPs is found to reach a saturation at an increasing fluence, while the saturation value of the minor axis increases with increasing the incident ion energy. The latter is attributed due to the NP confinement within a well-defined molten track radius in the amorphous SiO₂ matrix. On the other hand, Pt NPs with size smaller than 7 nm diameter did not show any sign of deformation but mostly indicate a decrease in size as a result of dissolution. In addition, Au nanocrystals (NCs) [42] with size between 1 and 6 nm diameters further grow in size under SHI irradiation with 100 MeV Au⁺⁸ ions to fluences of 5×10^{12} and 2×10^{13} ions/cm². These Au NCs were produced by implantation of 4×10^{16} ions/cm² of the 32 keV Au ion into silica glass. With increasing the irradiation fluence to 1×10^{14} ions/cm², the amount of Au nanocrystals retained in the silica matrix dropped to about 20% of its initial value as a result of dissolution. These observations

suggest that smaller NPs have the tendency to fragmentation and/or disintegration. With the latter in minds, a hypothesis could be that when the minor axis of the aligned nanostructures (nanorods and/or nanowires) is reaching a critical value (maybe in the order of about 8 nm), such nanostructures will disintegrate under subsequent direct ion impact. Due to the parallelism of such nanostructures with the ion beam direction, such ion impact does immediately affect the entire nanowire. Besides, a minimum value for the minor axis of the nanorods and/or nanowires implies that these aligned nanostructures can only be further elongated when atoms from the matrix are collected. In additions, the mutual ion impacts determine which nanowires disintegrate and which grow. In this frame, the NP disintegration and growth are treated as a continuous process, extending also in the region of the collective growth (region B). Eventually, and in view of the decreasing density of the nanowires, the rate of disintegration with fluence decreases and so does the rate of elongation until ultimately a saturation length is reached.

5. Conclusion

In this chapter, we have shown that the shape of originally spherical Au NPs embedded in a single plane within a SiO₂ matrix can be modified by swift heavy ion irradiations. Under Ag swift heavy ion irradiation, spherical Au NPs undergo anisotropic deformation into single prolate nanorod with their long axis parallel to the ion beam direction. Systematic experimental investigation has led to the existence of the so-called threshold fluence for deformation. The extent of the latter has been carried out by variation of both NP size and ion energy. In addition, we have shown that the NP size and areal density have a substantial influence on the characteristics of the ion-induced elongation of confined NPs. In that respect, a well-defined size-dependent NP elongation below a certain irradiation fluence (region A) is identified. In this region, all the NPs elongate following *individual elongation process* depending only on NP size. Under irradiation with fluence above a certain critical value of 1.00×10^{14} ions/cm², region B at which the deformation is regarded as *collective mechanism* is defined. In this region, longer nanowires are created as a product of several metallic NP contribution to the nanowire growth. Furthermore, in region B, the NP deformation increases with increasing initial NP areal density, i.e., the higher the initial NP areal density is, the longer the nanowires are grown.

Author details

Elmuez A. Dawi

Address all correspondence to: e.dawi@ajman.ac.ae

Ajman University, Ajman, UAE

References

- [1] Mayer JW. Ion implantation in semiconductors. Electron Devices Meeting, 1973 International, 1973; Vol. 19. pp. 3-5

- [2] Cheam DD, Bergstrom PL. ASC manuscripts. 2008; M/MP-2
- [3] Nastasi M, Mayer JW, Hirvonen JK. Ion-Solid Interactions: Fundamentals and Applications. Great Britain: Cambridge University Press; 1996
- [4] Klaumünzer S, Schumacher G. Physical Review Letters. 1983;**51**(1987)
- [5] Klaumünzer S, Ming-dong H, Schumacher G. Physical Review Letters. 1986;**57**(850)
- [6] Benyagoub A, Löffler S, Rammensee M, Klaumünzer S, Saemann-Ischenko G. Nuclear Instruments and Methods in Physics Research Section B. 1992;**65**(228)
- [7] van Dillen T, Polman A, Fukarek W, van Blaaderen A. Applied Physics Letters. 2001;**78**(7):910
- [8] Toulemonde M, Dufour C, Meftah A, Paumier E. Nuclear Instruments and Methods in Physics Research Section B. 2000;**903**:166-167
- [9] Gerardy JM, Ausloos M. Physical Review B. 1982;**25**:420
- [10] Penninkhof JJ, Polman A, Sweatlock LA, Maier SA, Atwater HA, Vredenberg AM, Kooi BJ. Applied Physics Letters. 2003;**83**(20):4137
- [11] Quinten M, Kreibig U. Applied Optics. 1993;**32**:6173
- [12] Roorda S, van Dillen T, Polman A, Graf C, van Blaaderen A, Kooi BJ. Advanced Materials. 2004;**16**:235
- [13] Gonella F, Mazzoldi P. Handbook of Nanostructured Materials and Nanotechnology. Vol. 4. San Diego: Academic Press; 2000
- [14] Kooij ES, Brouwer EAM, Wormeester H, Poelsema B. Colloids and Surfaces A: Physicochem. Engineering Aspects. 2003;**222**:103
- [15] Zhong O, Inniss D, Kjoller K, Elings VB. Surface Science Letters. 1993;**290**:L688
- [16] Digital Instruments, Santa Barbara, CA
- [17] Ziegler JF, Biersack JP, Ziegler MD. SRIM—A version of the TRIM program, The Stopping and Range of Ions in Matter (2008). Available from: <http://www.srim.org>
- [18] Klaumünzer S, et al. Nuclear Instruments and Methods in Physics Research Section B. 2006;**244**:1
- [19] Klaumünzer S, et al. Nuclear Instruments and Methods in Physics Research Section B. 2004;**225**:136
- [20] Penninkhof JJ, Graf C, Van Dillen T, Vredenberg AM, Van Blaaderen A, Polman A. Advanced Materials. 2005;**17**:1484
- [21] Penninkhof JJ. PhD Thesis. Utrecht University, September, 25th (2006)
- [22] Messier R, Venugopal VC, Venul PD. Journal of Vacuum Science and Technology. 2000;**A 18**:1538
- [23] van Hattum ED, Palmero A, Arnoldbik WM, Rudolph H, Habraken FHBM. Applied Physical Letters. 2007;**91**:171501

- [24] Benyagoub A, Klaumünzer S, Toulemonde M. Nuclear Instruments and Methods in Physics Research Section B. 1998;**146**:449
- [25] Snoeks E, Weber T, Cacciato A, Polman A. Applied Physics. 1995;**78**:4723
- [26] Brongersma ML, Snoeks E, van Dillen T, Polman A. Journal of Applied Physics. 2000;**88**:59
- [27] van Dillen T, Siem MYS, Polman A. Applied Physics Letters. 2004;**85**:389
- [28] Primak W. Studies in Radiation Effects in Solids Gordon and Breach. Vol 4. New York; 1975
- [29] Devine RAB. Nuclear Instruments and Methods in Physics Research Section B. 1994;**91**:378
- [30] Meftah A, Brisard F, Constantini JM, Dooryhee E, Hageali M, Hervieu M, Stoquert JP, Studer F, Toulemonde M. Physical Review B. 1994;**49**:12457
- [31] Meftah A, Djebara M, Khalfaoui N, Toulemonde M. Nuclear Instruments and Methods in Physics Research Section B. 1998;**146**:431
- [32] Kluth P, Schnohr CS, Sprouster DJ, Byrne AP, Cookson DJ, Ridgway MC. Nuclear Instruments and Methods in Physics Research Section B. 2008;**266**:2994
- [33] Rotaru CC. Ph.D. thesis. University of Caen, 2004. Available from: <http://tel.archives-ouvertes.fr/tel-00005399>
- [34] Toulemonde M, Dufour C, Paumier E. Physical Review B. 1992;**46**:14362
- [35] Awazu K, Wang X, Fijimaki M, Tominga J. Physical Review B. 2008;**78**:054102
- [36] Giulian R, Kluth P, Araujo LL, Sprouster DJ, Byrne AP, Cookson DJ, Ridgway MC. Physical Review B. 2008;**78**:125413
- [37] Trinkaus H, Ryazanov AI. Physical Review Letters. 1995;**74**:5072
- [38] Trinkaus H. Nuclear Instruments and Methods in Physics Research Section B. 1998;**146**:204
- [39] Kluth P, Schnohr CS, Pakarinen OH, Djurabekova F, Sprouster DJ, Giulian R, Ridgway MC, Byrne AP, Trautmann C, Cookson DJ, Nordlund K, Toulemonde M. Physical Review Letters. 2008;**101**:175503
- [40] D'Orléans C, Stoquert JP, Estournès C, Grob JJ, Muller D, Guille JL, Richard-Plouet M, Cerruti C, Haas F. Nuclear Instruments and Methods in Physics Research Section B. 2004;**216**:372
- [41] Dais C, Bolse T, Bolse W, Shubert-Bischoff P, Lindner JNK. Nuclear Instruments and Methods in Physics Research Section B. 2006;**245**:239
- [42] Joseph B, Ghatak J, Lenka HP, Kuiri PK, Sahu G, Mishra NC, Mahapatra DP. Nuclear Instruments and Methods in Physics Research Section B. 2007;**256**:659

We are IntechOpen, the world's leading publisher of Open Access books Built by scientists, for scientists

6,300

Open access books available

171,000

International authors and editors

190M

Downloads

Our authors are among the

154

Countries delivered to

TOP 1%

most cited scientists

12.2%

Contributors from top 500 universities



WEB OF SCIENCE™

Selection of our books indexed in the Book Citation Index
in Web of Science™ Core Collection (BKCI)

Interested in publishing with us?
Contact book.department@intechopen.com

Numbers displayed above are based on latest data collected.
For more information visit www.intechopen.com



Ion Beams for Materials Analysis: Conventional and Advanced Approaches

Vladimir Egorov and Evgeny Egorov

Additional information is available at the end of the chapter

<http://dx.doi.org/10.5772/intechopen.76297>

Abstract

Ion beam material diagnostic possibilities are discussed. Experimental data of H^+ and He^+ ion beams interaction with material for the energy range 0.8–1.6 MeV are presented. There are described the conventional ion beam analytical complex facility and some peculiarities featured for Sokol-3 IMT RAS one. Common characteristics of ion beam analytical methods are described. Specific attention is focused on the ion beam methods use for real objects investigations. It is shown that these methods are very effective for the light element diagnostics. New technology for the element surface analysis on base of the PIXE method modification by the planar X-ray waveguide-resonator application is elaborated. Attention is drawn to facts that all ion beam experimental methods are nondestructive and the Rutherford backscattering spectrometry is real quantitative analytical procedure.

Keywords: ion beam, ion beam scattering, Rutherford backscattering, RBS, ions stopping, ion acceleration, ion beam channeling, nuclear reactions, particle-induced X-ray emission, PIXE, ion beam-induced luminescence, depth elements profiles, nuclear elastic recoil spectrometry, vacuum systems, target chamber, X-ray fluorescence yield, X-ray detector

1. Introduction

It is well known that the interaction of ion beams—high energy charged particles fluxes with material is accompanied by the complex of specific effects [1]. The interaction with the solid material electron subsystem leads to uniform stopping of high energy charged particles. This interaction is not elastic owing to the atomic ionization effect initiation. Ion collisions with the atomic nuclei can have the elastic as well as inelastic character. Main channels of the interaction are presented in **Figure 1**. These channels can be used for the nondestructive quantitative analysis of studied target element composition and some features of its structure [2]. In result

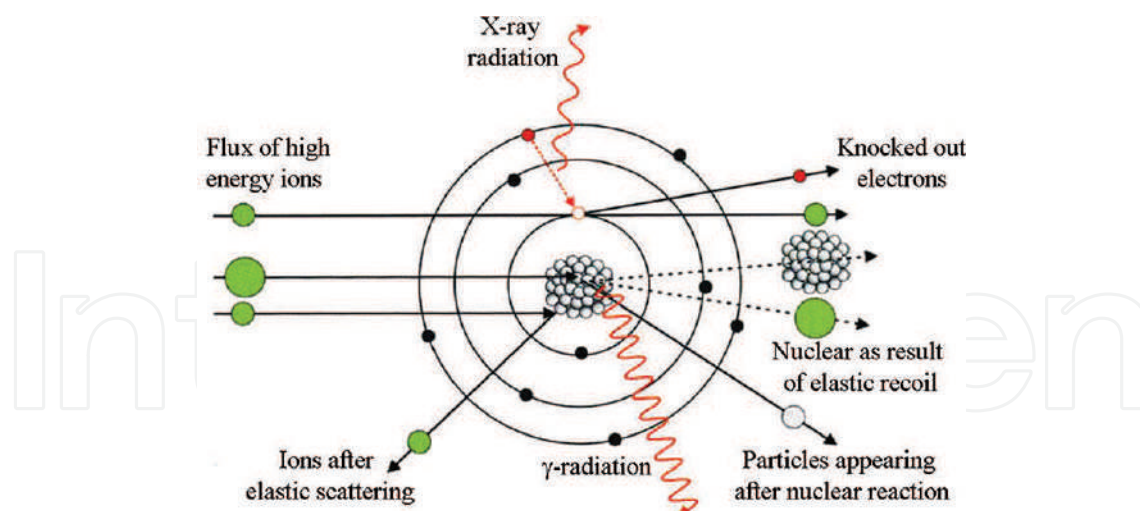


Figure 1. Products of the high energy charged particles interaction with atoms flux.

of the ion beam stopping the material, electron subsystem comes into the excited state. The excited state relaxation can happen by the radiation mechanism through luminescence. The optical luminescence spectra analysis allows to characterize some features of the studied material band structure [3–5]. More high energy relaxation leads to the X-ray characteristic fluorescence irradiation. Collection of X-ray fluorescence spectra is the subject of the particle-induced X-ray emission (PIXE) spectrometry [6–8].

The elastic interaction of high energy ion with atomic nucleus is described by the Rutherford expression, which presents fundamental basis for the Rutherford backscattering (RBS) spectrometry [8–14]. This type of ion-nucleus collision allows to create the nucleus elastic recoil spectrometry [15, 16]. The inelastic ion-nucleus collision leads to the nucleus excitation and the nuclear reaction provoking [17, 18]. Specific peculiarity of the ion-nucleus interaction is the nonRutherford scattering effect [19]. This effect is connected with the increase in time interaction and change in scattering conditions. It must be taken into account to use the proton beam scattering on nuclear of light elements at energy range 0.5–2.0 MeV. In such cases, this effect can be used for the increase in analytical efficiency for the light element diagnostics.

The above enumerated techniques based on interaction of charged particles beams with substance are indifferent to the material structure peculiarities. At the same time, experimental investigations showed that the monocrystalline and epitaxial targets study by ion beam analytical methods demonstrate specific deviations from results characteristic for polycrystalline and amorphous ones. The monocrystalline structure is characterized by long-range open spaces through the ion that can propagate without significant scattering and diminished stopping. Ions can spread to these open channels by glancing collisions with the atoms rows or planes, hereby extending the final ion distribution deeper into target. This effect was called the ion beam channeling, which can be the axial or planar one [20, 21]. The axial channeling of ion beam is visualized in **Figure 2**. The channeling effect can be used to the trace impurities diagnostics in single crystal and epitaxial targets, the structure defects analysis and for the position determination of impurity atom in the structure. Moreover, this method can allow to define the relative angular orientation of the unit cells axis within the layers of multilayer

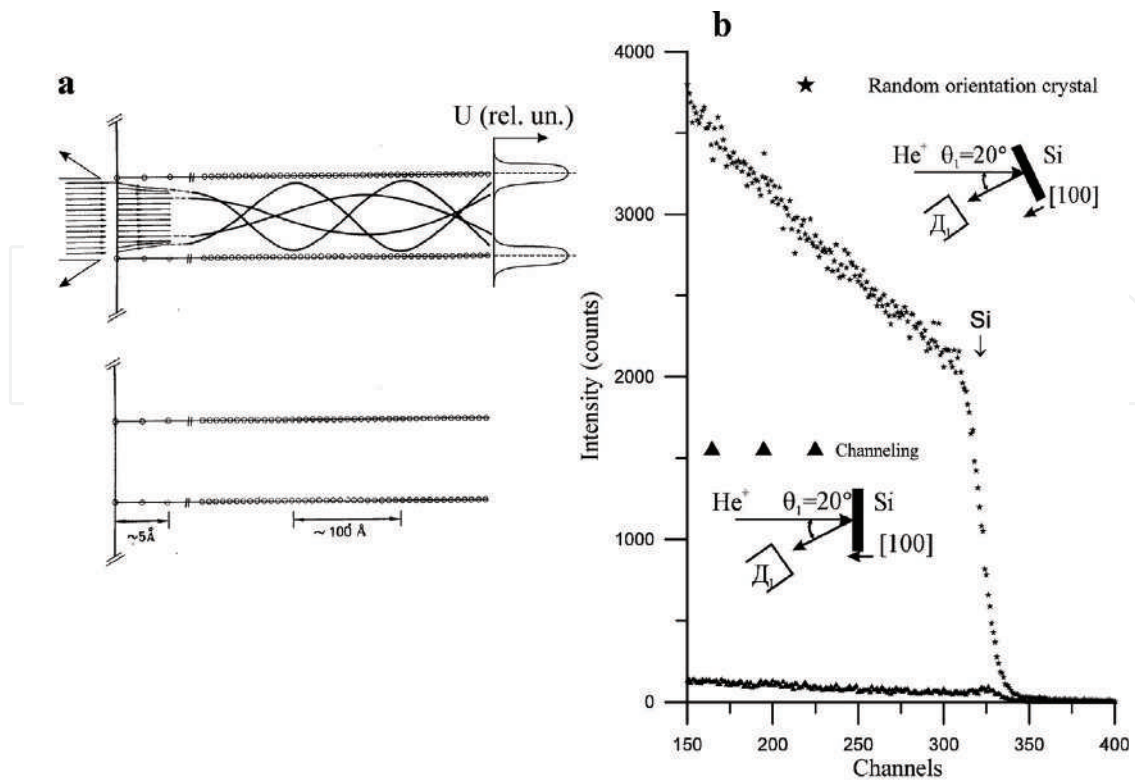


Figure 2. The model of He^+ ions flux axial channeling through Si monocrystal along [100] crystallographic axis (a) and RBS spectra He^+ ions flux for Si crystal in random position about the ion beam propagation direction and in conditions of the ion beam channeling along [100] its axis (b).

heterostructures [22]. The ion beam channeling is accompanied by the excitation processes efficiency reduction connected with inner atomic electrons of the target. X-ray fluorescence yield intensity excited by high energy beams comes down. At the same time, the intensity of ionoluminescence increases. In the ion beam channeling conditions, the nuclear reaction efficiency and probability of the nuclear recoil effect reduce to a minimum.

Ion beam experimental methods of the material diagnostics are realized by use of ion beams analytical complexes Sokol-3. This complex is in our disposal and will be shortly described in the next section.

2. Experimental setup for ion beam measurements

Common arrangement of the Sokol-3 units is presented in **Figure 3**. The Van de Graaff electrostatic generator, which can generate H^+ and He^+ ion fluxes in the energy range 0.05–2.0 MeV with energy dispersion $\Delta E = 0.1/0.3$ keV, is the most important device of the ion beam analytical complex. The generator allows to vary of the ion beam current magnitude from 0.1 to 50,000 nA (from 6×10^8 to 3×10^{13} ions/s) in the beam spot on studied target with diameter 0.1–5 mm. The ion beam current magnitude stability is 3–5%. The analytical complex is equipped by the vacuum system with total volume near 1 m^3 . The clean vacuum environment in ion guides and experimental chambers is provided by turbomolecular and magnetic-discharge pumps

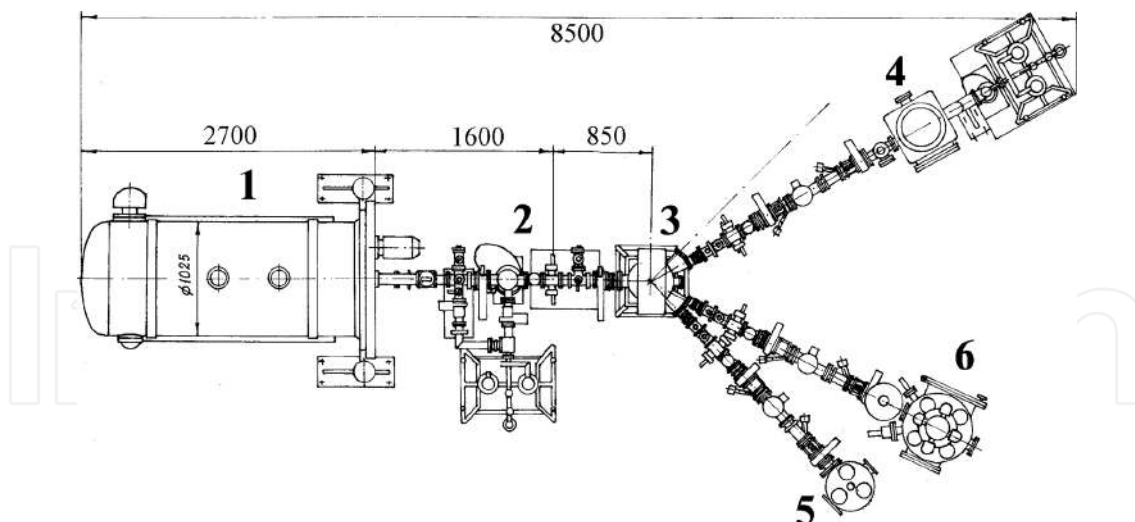


Figure 3. Units arrangement of Sokol-3 ion beam analytical complex facility. 1. Van de Graaff accelerator ESU-2; 2. Vacuum ion guide; 3. Analytical electromagnet; 4. RBS chamber; 5. Chamber for nuclear recoil spectrometry; 6. Chamber for PIXE and ionoluminescence measurements.

working in a pair with additional use the liquid nitrogen freezing out. In the result, the medium residual pressure in the vacuum system is usually near 1×10^{-6} torr (7×10^{-4} Pa). At the same time, experimental investigations in the complex chambers are accompanied by C-H film appearing in the ion beam spot. It is connected with great number of the vacuum joints with rubber-like gaskets. Any ion beam analytical complex must be provided by the analytical magnet for the ion beams turning into experimental chambers. Our analytical complex is equipped by three experimental chambers for the RBS, nuclear reaction, and channeling measurements, for the registration of the nuclear recoil effects and for the PIXE and ionoluminescence spectrometry. The Rutherford backscattering is characterized by the original system of the studied target scattered ions registration. It has two detectors for the ions fluxes parallel registration on angles $\theta_1 = 167^\circ$ and $\theta_2 = 125^\circ$ to the initial direction of ion beam propagation as shown in **Figure 4**. Furthermore, the figure presents experimental and theoretical RBS spectra of He^+ ions for Nb/Si target obtained for the angles pointed above. It is very important that two independent RBS spectra represent the target element distribution. The spectra approximation carried out by RUMPP computer program built on base of the RUMP software modification [23] allowed to obtain the target depth element concentration profile. The depth element profile of this target is very simple and the double detector registration system application in this case has an excessive character. But the approximation of two RBS spectra allowed to increase precision of the Nb thin film thickness. Application of two detector systems for RBS investigations and for registration of the nuclear reaction products allows to avoid possible errors at the experimental data interpretation.

We used the original construction for the PIXE measurements modification. **Figure 5a** presents chamber for conventional PIXE measurements execution. The conventional PIXE spectrometry allows to characterize the volume element composition of studied target. The method modification by application of the planar X-ray waveguide-resonator (PXWR) presents possibilities of the target surface element composition study [24]. **Figure 5b** shows the measurement scheme dedicated for the surface element study. PXWR can transport X-ray

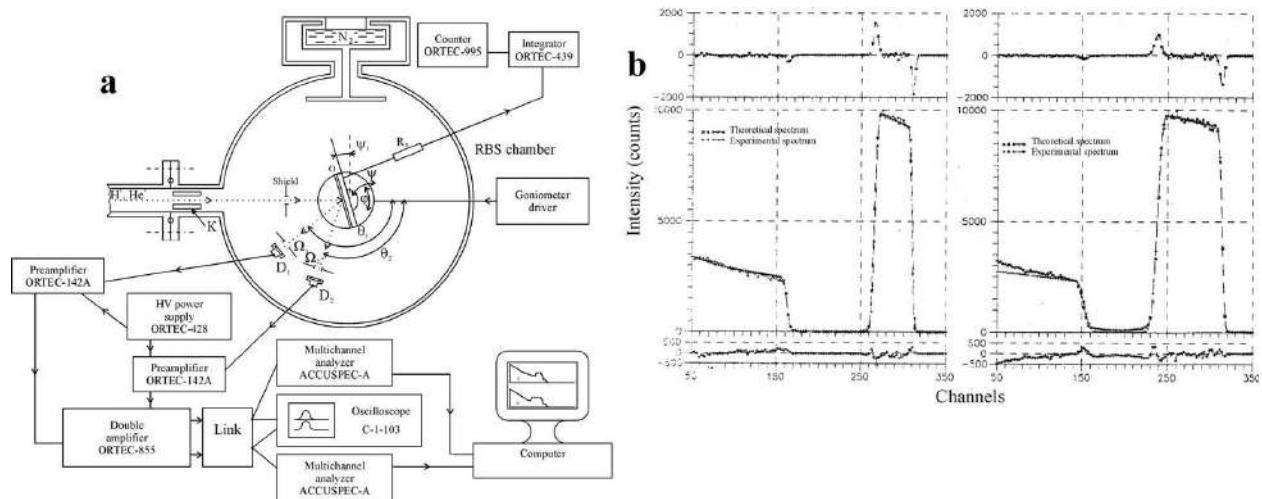


Figure 4. Schematic design of RBS chamber of Sokol-3 analytical complex equipped by two charge particle detectors (a) and pattern of application for study of Nb thin film with thickness $t=135.20.7$ nm on Si substrate (b).

quasimonochromatic radiation according to the waveguide-resonance mechanism of radiation flux propagation [25]. The waveguide-resonator showed in **Figure 5b** is formed by the Be polished reflector and surface of the studied target. The distance between Be reflector and target surface is equal $0.15 \mu\text{m}$. Be reflector has the hole for the exciting ion beam propagation to the target. The extended slit clearance formed by Be reflector and target surface captures radiation from the target X-ray fluorescence yield corresponding to the surface atoms fluorescence yield and transports it into SDD X-ray detector. Similar measurement geometry for the surface elements diagnostics at ion beam excitation presents

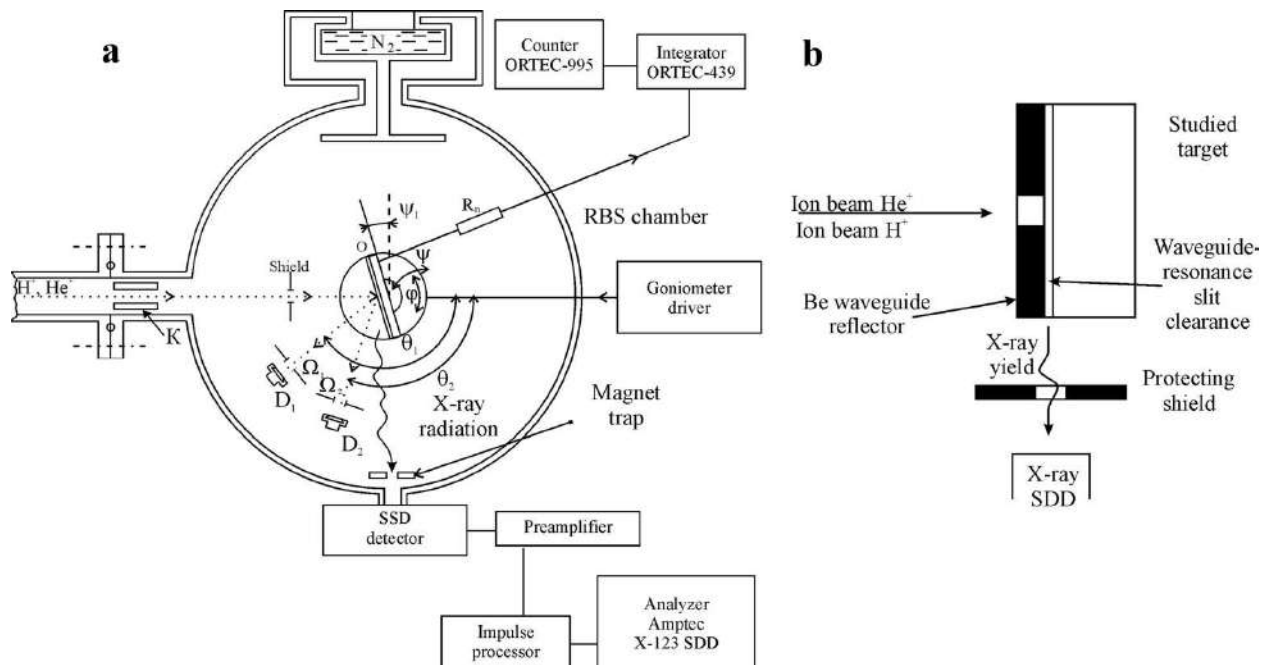


Figure 5. Experimental chamber for the PIXE conventional measurements (a) and scheme of the modified PIXE setup allowed to study the surface element composition (b).

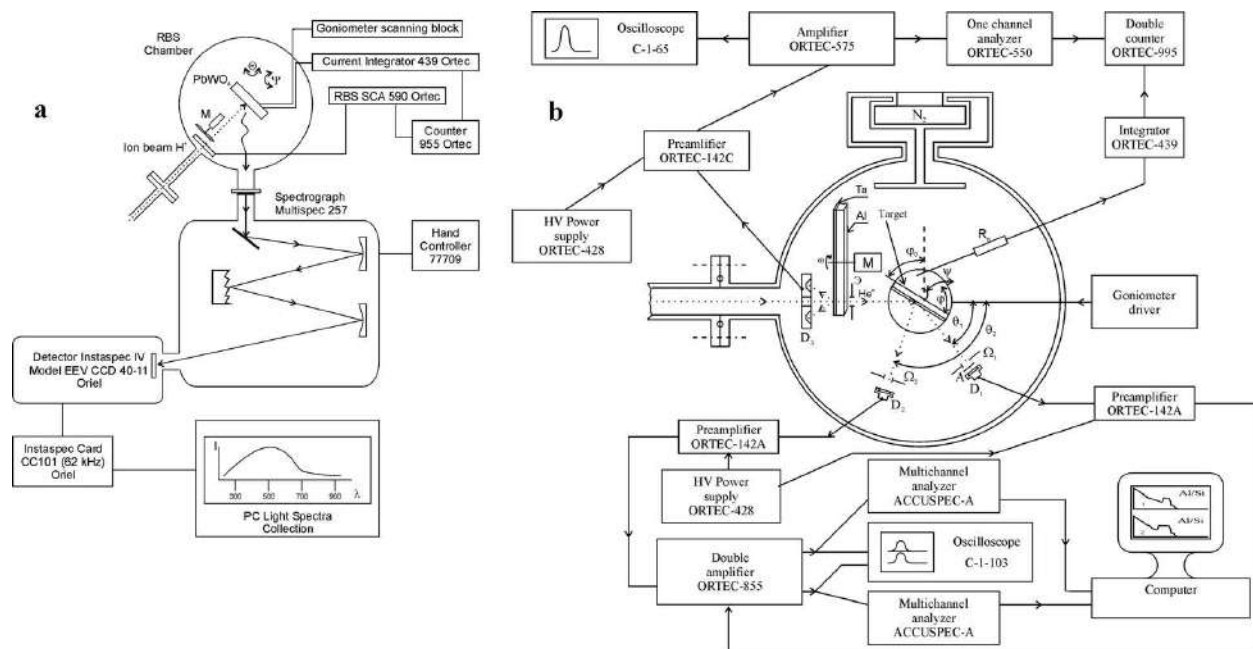


Figure 6. Schemes of experimental setups for yield registration of the light luminescence from the studied target at ion beam excitation (a) and for the target parallel investigation by RBS and the elastic nuclear recoil methods (b).

new experimental method, which was named as the total X-ray reflection fluorescence at particle excitation (TXRF PE).

Figure 6 shows the experimental chamber arrangement for the ionoluminescence and the nuclear recoil spectrometry. These investigation methods are realized in frame of the Sokol-3 facility in conventional arrangement.

Experimental investigations of the ion beam channeling can be executed in any chambers of the analytical complex. But most part of these experiments is carried out by using the RBS chamber.

3. Rutherford backscattering spectrometry as the basic method of material ion beam diagnostics

3.1. Common principles of the method

The Rutherford backscattering conception is based on possibility of the energy losses direct calculation for ion beams interacting with electron and atomic nuclear material subsystems. The energy redistribution in the ion-nucleus collision is defined by the kinematical factor expression [10]:

$$E_1 = E_0 \left[\frac{\sqrt{M_2^2 - M_1^2 \sin^2 \theta} + M_1 \cos \theta}{M_1 + M_2} \right] \quad (1)$$

where E_0 and E_1 are energies of ion pre- and post-collision, M_1 and M_2 are masses of ion and nucleus accordingly and θ is the angle of ion deviation from its initial propagation direction.

There is discussed the “backscattering” situation because the kinematical factor maximum magnitude is obtained for θ near 180° . In this case, we have the best mass resolution.

Probability of the ion-nucleus collision is defined by the Rutherford famous formula in form of the scattering average differential cross-section σ , which can be presented in the laboratory coordinates system by the next expression [8]:

$$\sigma = \frac{Z_1 Z_2 e^2}{2E} \frac{\sqrt{1 - x^2 \sin^2 \theta} + \cos \theta}{\sin^4 \theta \sqrt{1 - x^2 \sin^2 \theta}} \quad (2)$$

where x is M_1/M_2 relation, Z_1 and Z_2 are charges of ion and nucleus, e is the electron charge and E is the ion pre-collision energy. The charge particle detector registers the total particles quantity A_i , which defines by the collision cross-section, the total quantity of charged particles interacted with the studied target q , the detector spatial angle Ω , the volume atomic concentration N_i and the layer thickness t connected with the RBS spectrum discreteness degree and can be presented by the expression [8]:

$$A_i = q \Omega \sigma N_i t \quad (3)$$

Total Rutherford backscattering spectrum presents aggregate of similar magnitudes outlined in the diagrammatic form. Sample of this similar diagram is shown in **Figure 7**. RBS spectra of He^+ and H^+ ion beams obtained for the SrTiO_3 stoichiometric target are presented. These spectra are diagrams reflecting dependences of the ion beams scattering yield on the energy of scattering particles. Every channel of the diagrams reflects the ions number scattering on nuclei the target atoms (Eq. (3)). An energy scales of the spectra are connected with the depth

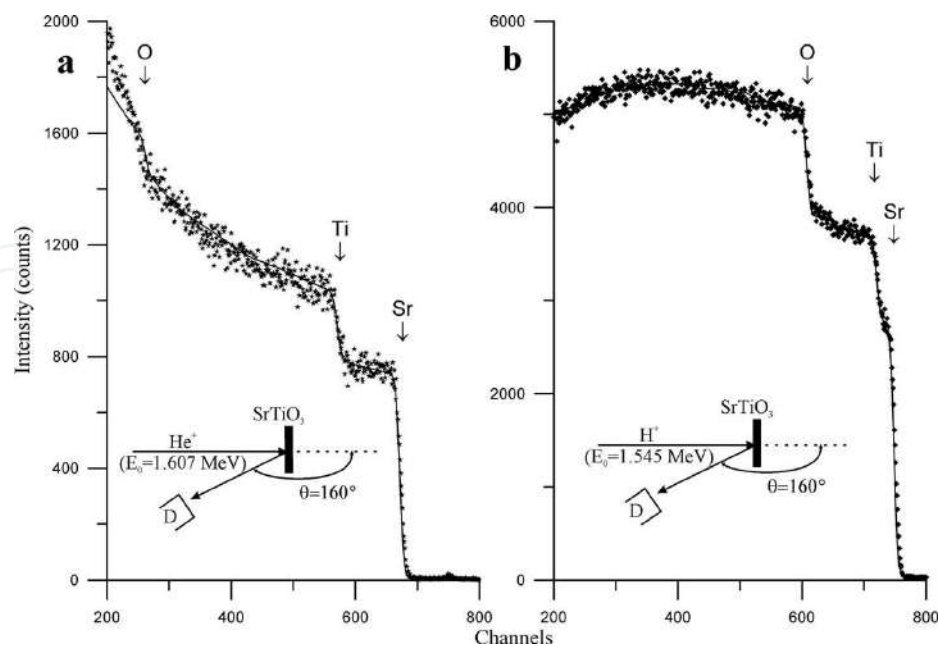


Figure 7. RBS spectra of He^+ (a) and H^+ (b) ion beams obtained for the SrTiO_3 stoichiometric target. Experimental spectra are approximated by RUMPP program and the theoretical spectra are superposed with experimental ones. The arrows designate the scattering energies corresponding to atoms on the target surface. The measurement geometry is shown on the inserts. The energy step is 1.9 keV/channel.

elements distribution profile for the studied target. The scattering energy for surface atoms is defined by the kinematical factor, only. These energies are connected to steps edges of the diagrams. The scattering description of ion beams on nuclei of the internal atoms demands taking into account the ions stopping as pre- and post-scattering act. The stopping energy losses ΔE on the distance Δx are usually described by the Bohr formula:

$$-\frac{\Delta E}{\Delta x} = \frac{4\pi Z_1^2 e^4 n}{mv^2} \ln \frac{2mv^2}{I} \quad (4)$$

where Z_1 and v are the charge and velocity of the stopping ion, e and m are the charge and mass of electron and n is the studied material electron density. I is the ion average energy loss for the electron excitation (near 30 eV). I and n parameters are not constants and depend from very much factors. As a result, the decision was made to present the stopping losses in the tabular form [26]. This approach allowed to calculate the energy losses by introduction of the $[\bar{\epsilon}]$ effective stopping cross-section accordingly to the expression [27].

$$\Delta E = [\bar{\epsilon}]Nt \quad (5)$$

where N is the atomic density (atoms/cm³). In case of the multielement material, the stopping cross-section is defined accordingly to the Bragg rule:

$$\epsilon^{AmBn} = m\epsilon^A + n\epsilon^B \quad (6)$$

Accuracy of tabular magnitudes for the material stopping cross-section is limited by value near 1%. In the result, the material parameters determination accuracy cannot be better of this value. In the practical work, the stopping cross-section data are fed into a computer program providing the RBS spectra approximation [23, 27]. As a result, we have that every channel of the spectrum is connected with a planar layer of the target with thickness t and average element concentration N . The rise steepness of steps in the RBS spectrum is defined by the detector energy resolution used for the spectrum registration. The resolution of He⁺ ions scattering fluxes is near 10 keV that corresponds to the depth resolution 10–12 nm at the ion beam vertical incidence on the studied target and up to 2 nm at the sliding incidence.

The Rutherford backscattering spectrometry is very effective method of the thin film structure analysis. **Figure 8** demonstrates experimental and theoretical spectra of RBS He⁺ ion beam for SrTiO₃ thin film on the silicon substrate with oxidizing layer. The experimental spectrum theoretical approximation showed that the film is characterized by the stoichiometric composition with thickness $t = 230$ nm. Theoretical approximation of the spectrum did not involve some difficulties, because the film material contained elements with high atomic masses, and substrate, on the contrary, contained light elements. Similar situation can be observed in **Figure 9**. It demonstrates experimental and theoretical RBS of He⁺ and H⁺ ion beams spectra for the Hf/Cr/Al multilayer target. Theoretical approximation of these spectra showed that the Hf film had thickness $t = 120 \pm 5$ nm and contained 11% of Sr atoms and 14% of Ti atoms. Cr film had not admixture. It was characterized by the thickness $t = 40 \pm 7$ nm. Interdiffusion zone between these films had the thickness near 25 nm. The surface roughness of the coating was

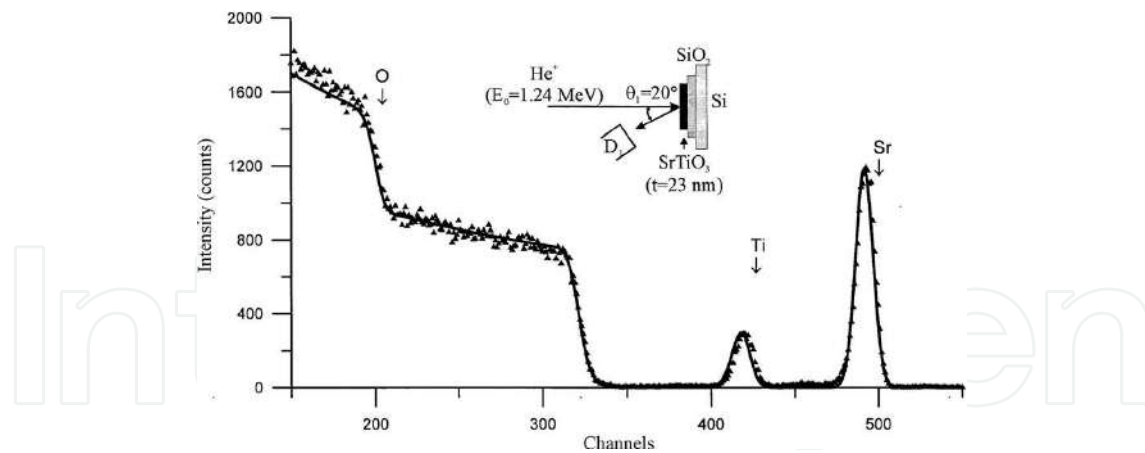


Figure 8. Experimental and theoretical RBS He^+ ions ($E_0 = 1.24 \text{ MeV}$) spectra for the $\text{SrTiO}_3/\text{SiO}_2/\text{Si}$ thin film structure. Arrows show the ion scattering energies on nuclei of atoms located on the target surface. Measurement geometry is shown on insert. Energy step 1.9 keV/channel .

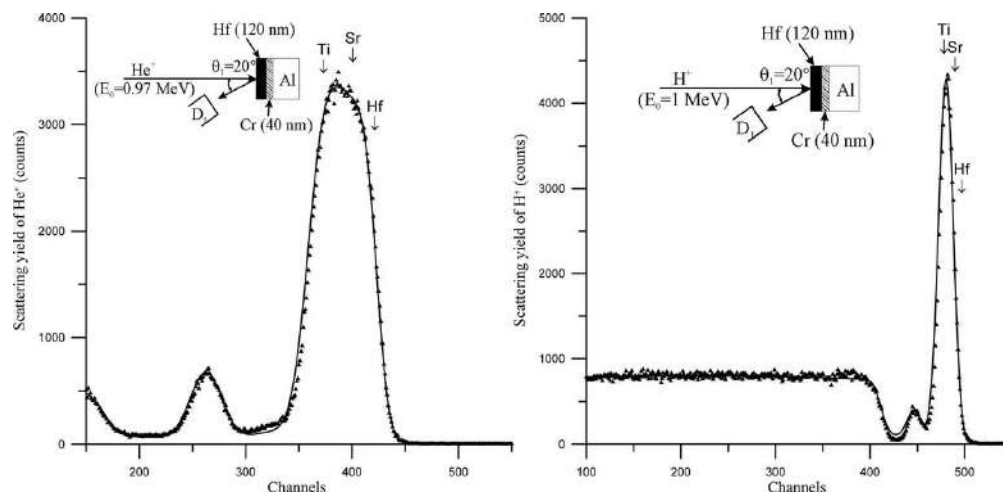


Figure 9. Experimental and theoretical RBS He^+ and H^+ ions spectra for the Hf/Cr/Al multilayer target. Arrows show the ion scattering energy on nuclei of atoms located on the target surface. Measurement geometry is shown on inserts. Energy step 1.9 keV/channel .

near 20 nm . Last parameter was evaluated on base of the steepness evaluation of step increasing for $\text{Hf}(\text{Sr}, \text{Ti})$ partial spectrum in comparison with this parameter for the Nb/Si standard target with roughness smaller 5 nm . The surface roughness Δr can be evaluated by the next expression [10]:

$$\Delta r = \frac{\sqrt{\Delta E_{\text{exp}}^2 - \Delta E_d^2}}{N_t [\bar{\sigma}]} \quad (7)$$

where ΔE_{exp} is the half width of the curve obtained as a result of the step rise steepness differentiation, ΔE_d is the detector energy resolution, N_t is the target atomic density and $[\bar{\sigma}]$ is the average value of the target atomic cross-section. Comparison of the RBS spectra obtained

for the same object shows that the He^+ ion beam application allows to have the better resolution and the H^+ ion beam use takes possibilities to test object on the more depth.

3.2. Possibilities of the RBS elements diagnostics

The RBS investigations of target with the heavy elements high content have evident problems. **Figure 10** presents RBS H^+ and He^+ ions beam spectra for the $\text{W}_{0.45}\text{C}_{0.43}\text{Co}_{0.12}$ target characterized by the tungsten atoms high concentration. The scattering cross-section of ions on the W nuclei is higher in comparison with these parameters for C and Co atomic nuclei. The alloy target composition had been gained in the result of the four spectra joint approximation obtained for He^+ and H^+ ion scattering beams collected for $\theta_1 = 167^\circ$ and $\theta_2 = 125^\circ$. The nonRutherford scattering effect was taken into account in the calculation. Owing to the necessity of this effect inclusion, specific investigation were executed [18, 19]. Sample of similar investigations of $^{12}\text{C}^6$ nucleus nonRutherford scattering factor is presented in **Figure 11**. Comparison of the Rutherford scattering cross-section and magnitudes of this parameter obtained in the experiments shows a great difference especially for the energy $E = 1735$ keV. The nonRutherford scattering factor value depends on the registration angle, and it is a need to get the factor experimental data for the selected measurement conditions. Similar work of the nonRutherford factor determination for carbon and boron atoms was executed preparatory to approximate RBS spectrum presented in **Figure 12**. The approximation of this spectrum is not simple procedure. Chief problem of the approximation is connected with the nonRutherford factors energy variation for carbon and boron atoms. The approximation result is presented in the table. Total thickness of the coating is $1.75\ \mu\text{m}$. Including the second RBS spectrum into approximation procedure does not improve the final result because this procedure demands additional investigations for receiving the nonRutherford factors energy dependences for the additional scattering angle. At the same time, the nonRutherford factor can be very useful for the

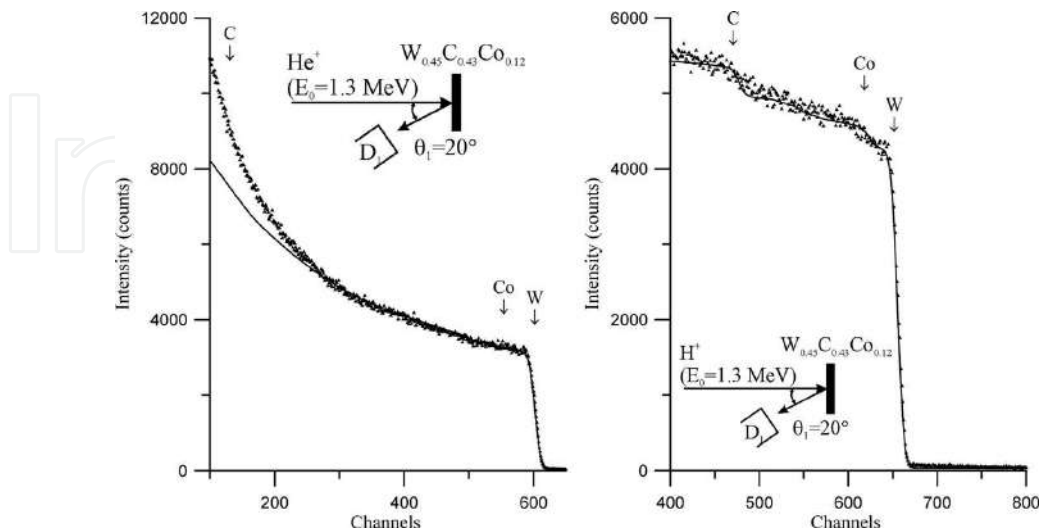


Figure 10. Experimental and theoretical RBS He^+ and H^+ ions spectra for the $\text{W}_{0.45}\text{C}_{0.43}\text{Co}_{0.12}$ high temperature alloy. Arrows show the ion scattering energies on nuclei of atoms located on the target surface. Measurement geometry is shown on inserts. Energy step 1.9 keV/channel.

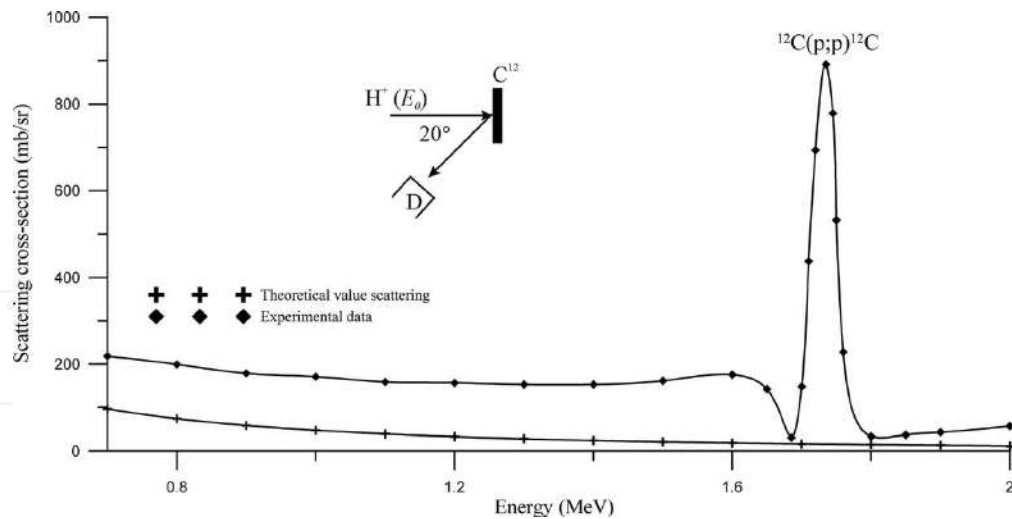


Figure 11. Theoretical and experimental energy dependences of H^+ ion beam scattering cross-section on ^{12}C nuclei for the collection angle $\theta = 167^\circ$.

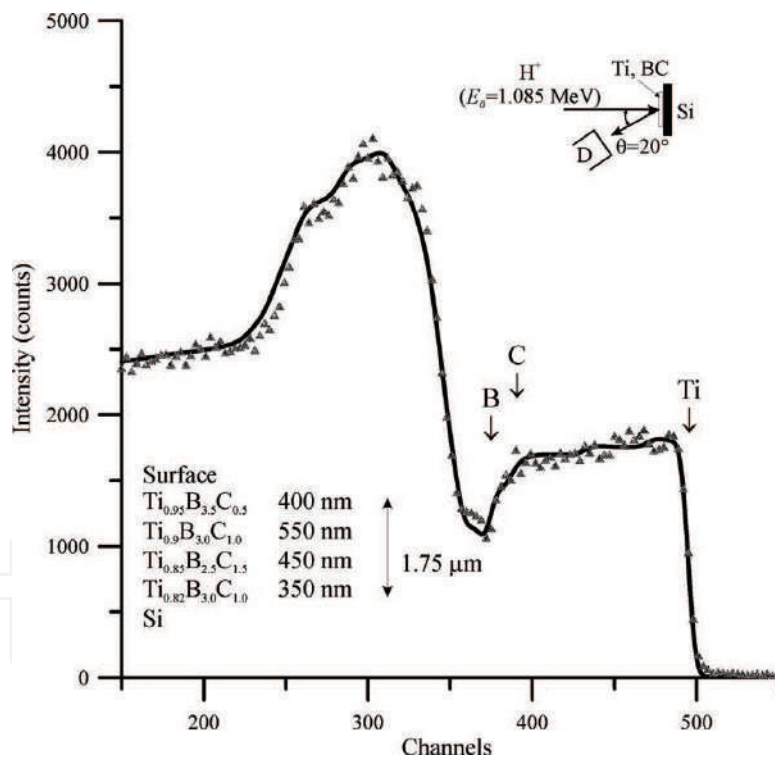


Figure 12. Experimental and theoretical RBS H^+ ions ($E_0 = 1.085$ MeV) spectra for Ti-B-C film deposited on Si substrate in result of the Ti_2CB_{10} sample magnetron sputtering (a) and table with the approximation results. Arrows show the ion scattering energies on nuclei of atoms located on the target surface. Measurement geometry is shown on insert. Energy step 1.9 keV/channel.

targets study containing light element. As the sample, RBS spectra of the polished beryllium disk are presented in **Figure 13**. The spectrum of the He^+ ions scattering in selected energy range does not distort by the nonRutherford factor. It shows that the target possesses the surface oxide film

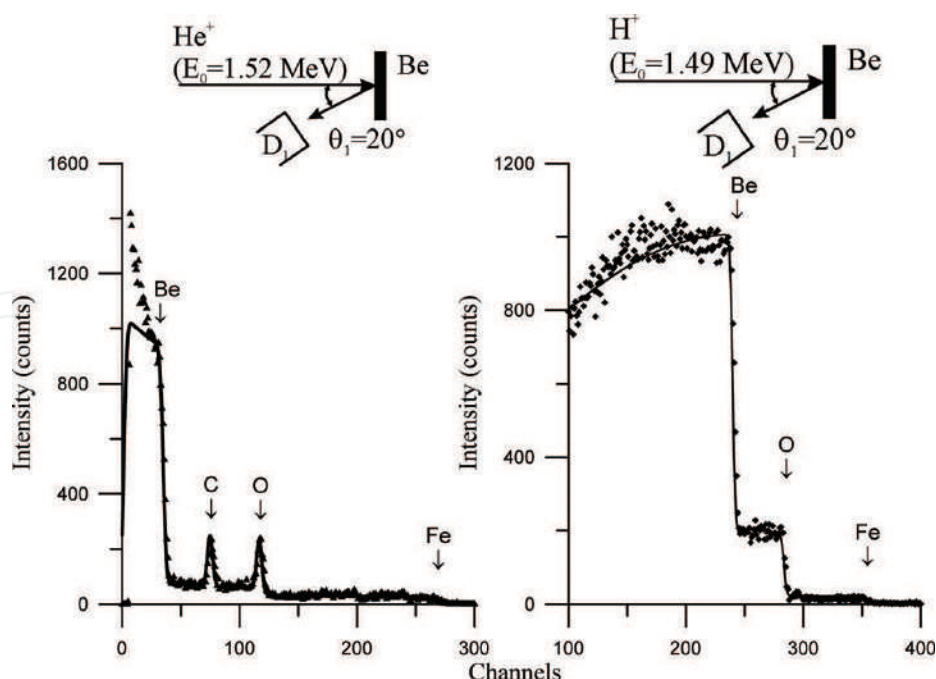


Figure 13. Experimental and theoretical RBS He^+ and H^+ ions for the polished Be disk. Arrows show the ion scattering energies on nuclei of atoms located on the target surface. Measurement geometry is shown on inserts. Energy step 3.8 keV/channel.

with thickness near 10 nm and the carbon hydrogen snuff with similar thickness appearing in result of the ion bombardment. The beryllium material contains 5% of the oxygen atoms, 0.1% of the iron atoms and 0.002% of the tungsten atoms. RBS spectrum of H^+ ions confirms these results. But its approximation is more difficult and it does not show the oxide film on the disk surface. At the same time, its registration time is more short in comparison with the He^+ spectrum collection.

Be polished disks can serve beautiful substrates for study of the solution dry residues and structures prepared by the specific procedure. Sample of the similar investigation is presented in **Figure 14**. This target is studied by RBS method and by application of the elastic nuclear recoil spectrometry. The main element composition of the petroleum film is $\text{H}_{0.07}\text{C}_{0.90}\text{S}_{0.028}\text{N}_{0.002}$. The film admixture composition defined by PIXE method will be discussed below. RBS spectrometry can be used for the medical preparation element diagnostics. **Figure 15** shows experimental and theoretical of RBS spectra for the solution dry residue of pantocrine in form of the film on Be substrate. The element composition knowledge is not chief problem for the pharmacology, but RBS, PIXE and nuclear reaction analysis can help for the specific element diagnostics of medical preparations.

Figure 16 shows experimental and theoretical RBS spectra for the graphene oxide film deposited on the Be substrate in the hydrothermal conditions. The technology of the grapheme oxide preparation is not perfect. As a result, the film contains Na and Ca atoms in the macro concentration. At the same time, RBS measurements allow to control the admixtures macro concentration presence and the film constitution. RBS method is useful for the target study containing other light element. **Figure 17** presents experimental and theoretical RBS He^+ and H^+ ions spectra for the hexagonal BN target. Mathematical approximation of the spectra shows

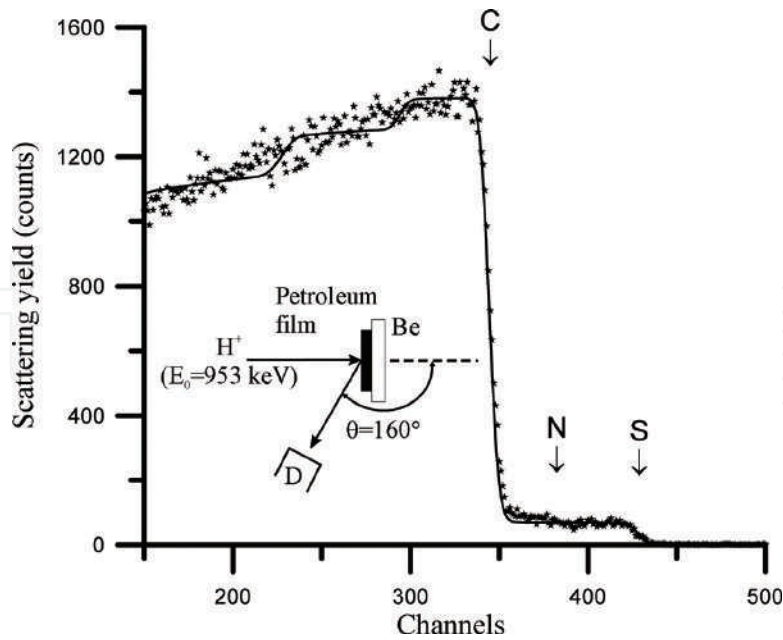


Figure 14. Experimental and theoretical RBS H^+ ions ($E_0 = 0.953$ MeV) spectra characterizing the petroleum film on Be substrate. Film composition is $H_{0.07}C_{0.9}S_{0.028}N_{0.002}$ (on mains elements). Arrows show the ion scattering energies on nuclei of atoms located on the film surface. Measurement geometry is shown on insert. Energy step 1.9 keV/channel.

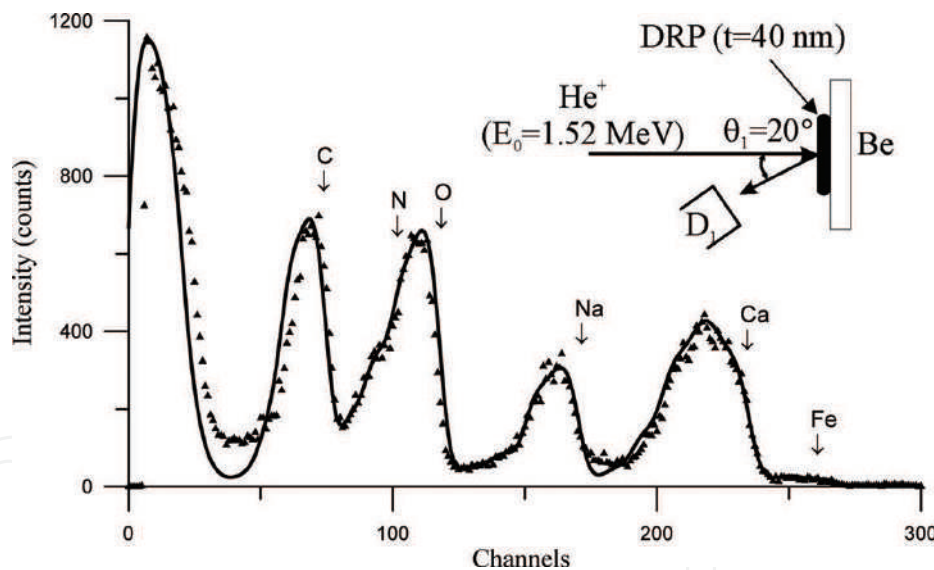


Figure 15. Experimental and theoretical RBS He^+ ($E_0 = 1.52$ MeV) ions spectra for the dry residue of pantocrine (DRP) aqueous solution on Be substrate. Arrows show the ion scattering energies on nuclei of atoms located on the dry residue film surface. Measurement geometrics and the pantocrine element compositions are presented on inserts. Energy step 3.8 keV/channel.

that the surface layer of the target has the boron increasing concentration. The spectrum of H^+ ions scattering showed that the scattering process is accompanied by the $^{11}B(p,\alpha)^8Be$ nuclear reaction course. The approximation has some problem in the context of $^{10}B^5$ and $^{11}B^5$ boron two isotopes existence in comparison concentrations. Every isotope is characterized by its own

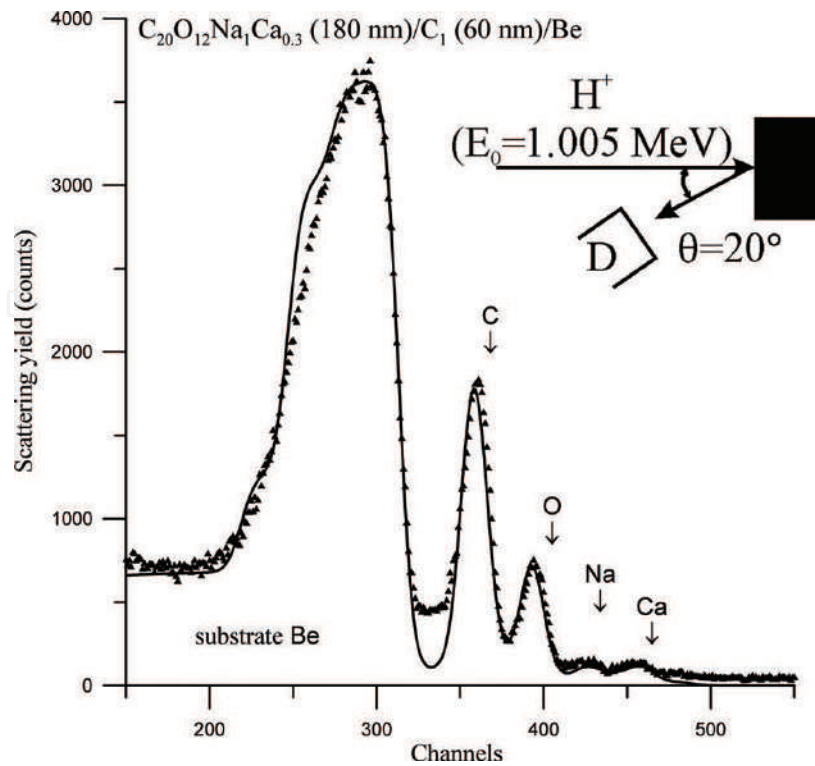


Figure 16. Experimental and theoretical RBS H^+ ($E_0 = 1.005$ MeV) spectra for the graphene oxide film deposited on the beryllium substrate in hydrothermal conditions. Arrows show the ion scattering energies on nuclei of atoms located on the film surface. Measurement geometries and the film parameters are presented on insert. Energy step 1.9 keV/channel.

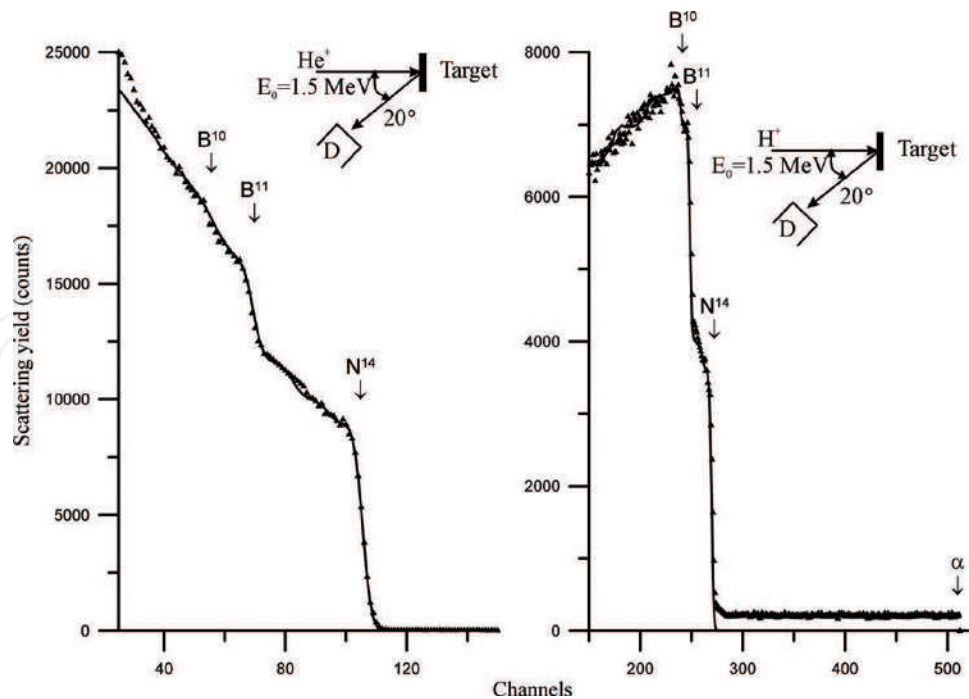


Figure 17. Experimental and theoretical RBS He^+ and H^+ ions ($E_0 = 1.5$ MeV) spectra for the Boron-Nitrogen target prepared by chemical exfoliation method in form of the free plate. Arrows show the ion scattering energies on nuclei of atoms located on the plate surface. Measurement geometry is shown on insert. Energy step 3.8 keV/channel.

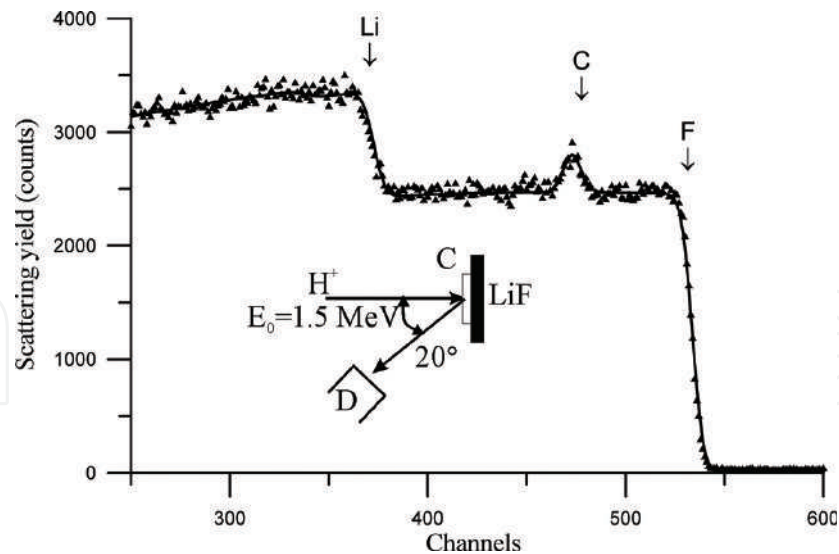


Figure 18. Experimental and theoretical RBS H^+ ions spectra for the LiF natural specimen. Surface carbon film with thickness $t = 12$ nm appeared during of the measurements process. Arrows show the ion scattering energies on nuclei of atoms located on the target surface. Measurement geometry is shown on insert. Energy step 1.9 keV/channel.

nonRutherford factors for the proton beam scattering. The nuclear reaction existence can be used for the boron concentration diagnostics in materials.

The Rutherford spectrometry can help to analyze the lithium atoms presence in materials. **Figure 18** shows RBS spectrum for the LiF stoichiometric target. This approximation required the nonRutherford data collection in the selected energy range for the H^+ ion beam scattering on Li and F atomic nuclei. But owing to the nonRutherford factor for Li, N, O and F atomic nuclei is not great the diagnostic of its atoms in targets with high concentration of heavy atoms presents some difficulties (see **Figure 10**). PIXE and ion beam channeling methods can help in this problem solution.

3.3. Atomic diffusion study by RBS method

Study of atomic diffusion peculiarities in solid material is the main branch of the solid state physics [28]. The wide use of thin material films has direct relation to study the material transport in thin films and coatings, since the density of short-circuit diffusion paths, especially grain boundaries (GBs) in its compositions is higher as compared with massive materials [29]. In our work, we used RBS spectrometry possibilities for the interdiffusion study in the Au/Cu bimetallic structure. **Figure 19** presents RBS He^+ spectra of the bimetallic structure pre and post treatment used different thermal actions [30]. At the long thermo treatment, the main interdiffusion mechanism was connected with the bulk diffusion (**Figure 19a**). In this case, the Au/Cu interface disappears and the intermediate layer arises. In case of the short high temperature treatment, we can see the copper atoms on the target surface, and Au atom from the initial interface dissolves in the Cu film. As a result, it is possible to obtain bulk and GB diffusion factors for different bimetallic combinations and to evaluate magnitudes of the possible segregation effect [31]. Particular significance for the diffusion practice can have the element isotopic investigation with the nuclear reaction application.

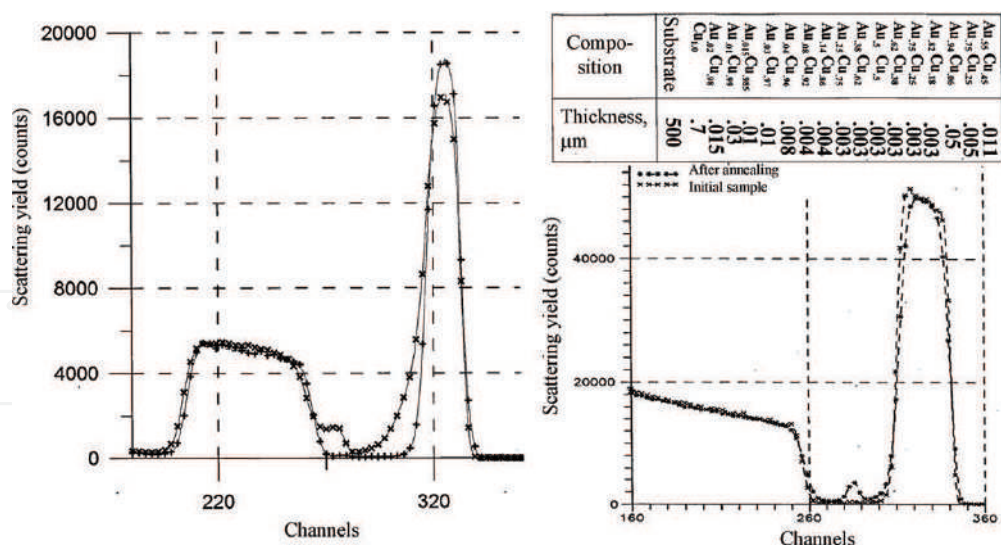


Figure 19. Experimental and theoretical RBS He^+ ions spectra for the Au/Cu bimetallic structure pre and post-treatment of the thermal action. The long time treatment at $T = 493$ K during 2400 sec of Au (44 nm)/Cu (190 nm) led to bulk interatomic diffusion (a). The short time treatment at $T = 523$ K during 300 sec showed the grain boundary diffusion, only. Second case is illustrated the table of the depth element distribution. Energy step 3.8 keV/channel.

3.4. Special features of the material density analysis

The material atomic density is a principle parameter of the substance condenses state. This parameter magnitude is usually defined by direct measurement of the subject mass and volume. But this method is not suitable for the material density determination of thin film structures. The Rutherford backscattering method can help to solve this problem. The atomic density distinction must lead to variation of the RBS yield intensity. **Figure 20** shows that the

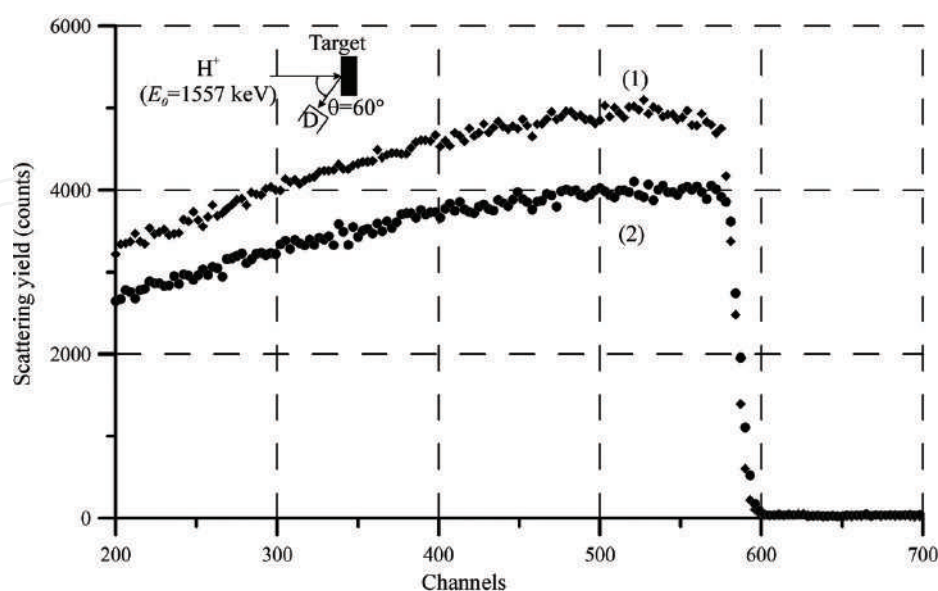


Figure 20. Experimental RBS H^+ ions ($E_0 = 1.557$ MeV) spectra for diamond ($\rho = 3.52$ g/cm³) and glassy carbon ($\rho = 2.21$ g/cm³) sample. Measurement geometry is shown on insert. Energy step 1.9 keV/channel.

expected effect takes place, really. RBS H^+ ions spectra for the diamond crystal and for the glass carbon sample are not equivalent. The diamond structure is characterized by a more compact atomic packing and demonstrated the enhanced scattering yield in the RBS spectrum. Its effect can be used for study of the porous structures. **Figure 21** shows the sample of the Rutherford backscattering study of the Al film in conditions after its preparation and in the result of thermal treatment [32]. Initial spectrum demonstrates the smaller scattering intensity yield in comparison with the theoretical spectrum (a). It is connected with the structure vacancy concentration near 6%. The thermal treatment let to the Al film, thickness decreasing from 300 to 284 nm (see the diagram (c)). The comparison of initial and finishing experimental spectra demonstrates the thickness decreasing and the atomic density increasing up to the normal structure value. Similar investigations is very important because the thin film preparation is no the equilibrium thermodynamic process.

The material atomic density variation can be connected with not only the structural vacancy appearing. Material in the nanostructure state is characterized by the increase in interatomic distance [33]. **Figure 22** demonstrates the Rutherford backscattering yield decreasing for the Ag thin films deposited on the silicon substrate. There are presented two RBS He^+ ($E_0 = 1.27$ MeV) ions spectra collected by our double detector system ($\theta_1 = 160^\circ$, $\theta_2 = 120^\circ$). Theoretical approximation of these spectra showed that the Ag film thickness is equal 48 nm but the evident discrepancy between Ag theoretical and experimental partial spectra was discovered. In this case, it was nearly equal to 6%. Moreover, the discrepancy increases as the Ag film became more slender and disappears when it will be large 100 nm. Our diffraction measurements confirmed supposition about the atomic density decreasing as a result of the interatomic distance growth. Similar RBS investigations can be very useful for the material atomic density evaluation in multilayer structures.

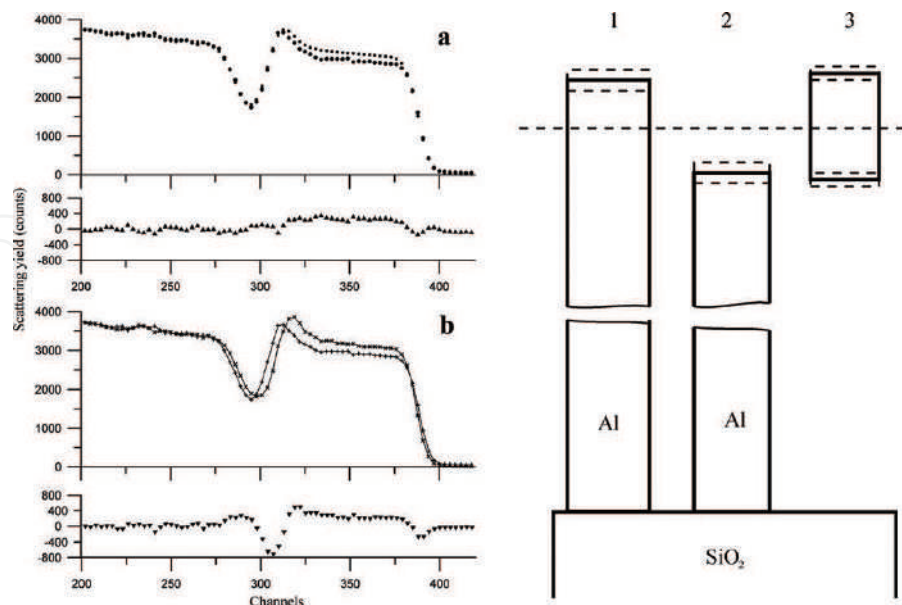


Figure 21. Experimental and theoretical RBS He^+ ($E_0 = 1.5$ MeV) ions for Al/SiO₂ structure pre (a) and post-thermal treatment (b) and the experimental diagram of the Al thin film thickness variation in result of the thermal treatment influence. Scattering angle is 160° . Energy step 1.9 keV/channel.

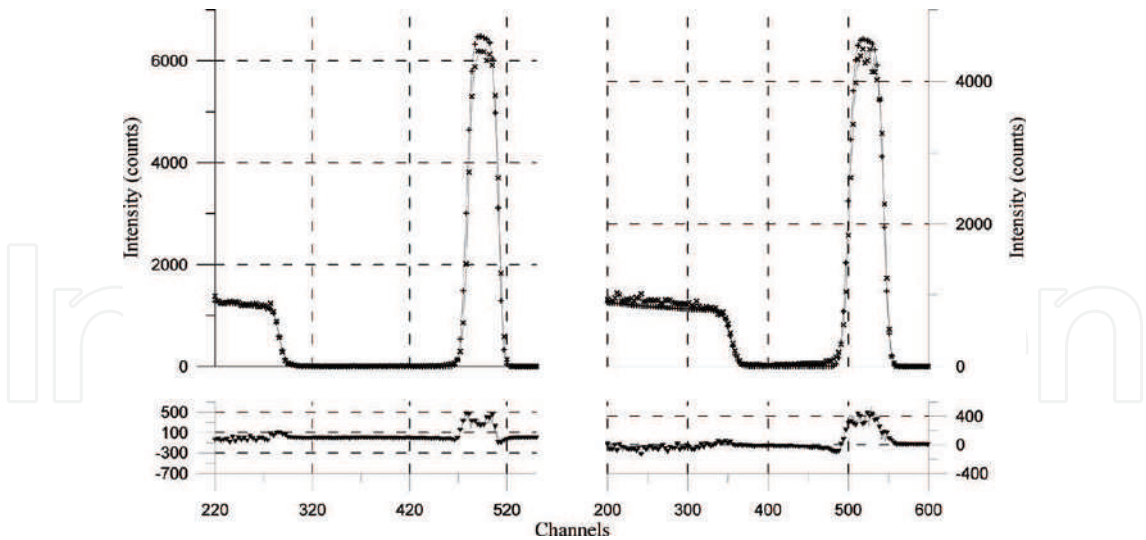


Figure 22. Experimental, theoretical and subtraction RBS He^+ ($E_0 = 1.27 \text{ MeV}$) ions spectra for the Ag thin film deposited on Si substrate. Spectra were collected by the double detector system ($\theta_1 = 160^\circ$ and $\theta_2 = 120^\circ$). Measurement geometries is presented on inserts. Energy step 1.9 keV/channel .

4. Particle-induced X-ray emission

4.1. Common principles of the method

Particle-induced X-ray emission is an ion analytical method, which utilizes the X-ray characteristic yield induced by ion beam interacting with the electron subsystem of target atoms. X-ray characteristic energy depends on Z atomic number of the target atom. PIXE method similar to other X-ray fluorescence diagnostic technologies collects the characteristic lines yield corresponding to K, L and M radiation series. At the same time, the main distinguishing of the

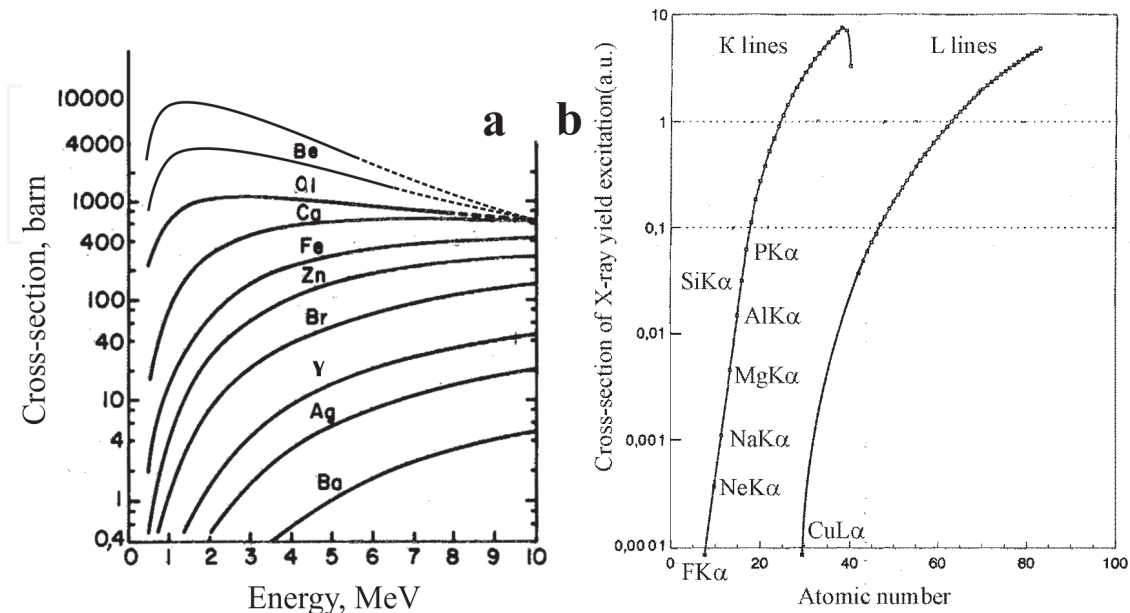


Figure 23. Cross-section of the X-ray fluorescence excitation by proton beam [34] (a) and $\text{MoK}\alpha$ radiation flux (b).

ion beam excitation method from X-ray, electron beams and gamma radiation ones is the very high efficiency of the low energy characteristic radiation excitation. In this plane, it is very interesting to compare the X-ray fluorescence yield excitation cross-section at use the X-ray high energy flux ($\text{MoK}\alpha$, $E = 17.4 \text{ keV}$) and the proton high energy beam. These data are presented in **Figure 23** [34]. Cross-sections of X-ray low energy lines excitation by the $\text{MoK}\alpha$ radiation flux use are characterized by very small magnitudes. At the same time, these parameters in conditions of the proton beam use demonstrate high values, especially for the low energy lines excitation. Comparison of $\text{YK}\alpha$ and $\text{AlK}\alpha$ fluorescence excitation cross-section in case of the $\text{MoK}\alpha$ radiation flux application shows that the yttrium fluorescence excitation efficiency is higher as the aluminum one on three orders. Similar comparison of these elements fluorescence excitation cross-sections at the proton beam excitation with energy $E_0 = 1 \text{ MeV}$ shows that the situation will be changed on the reverse one. So, it is evident that the light element diagnostic difficulties at the X-ray beam fluorescence application can be compensated by use the PIXE method [35, 36]. The X-ray fluorescence excitation by ion beams is more effective not only in comparison with the X-ray hard radiation flux application. PIXE bears some similarity to the fluorescence yield electron beam excitation but it characterizes by smaller values of the bremsstrahlung photon intensity yield. As a result, PIXE measurements are distinguished by the background lower level in comparison with the electron excitation. This fact is illustrated in **Figure 24** [7]. The spectra

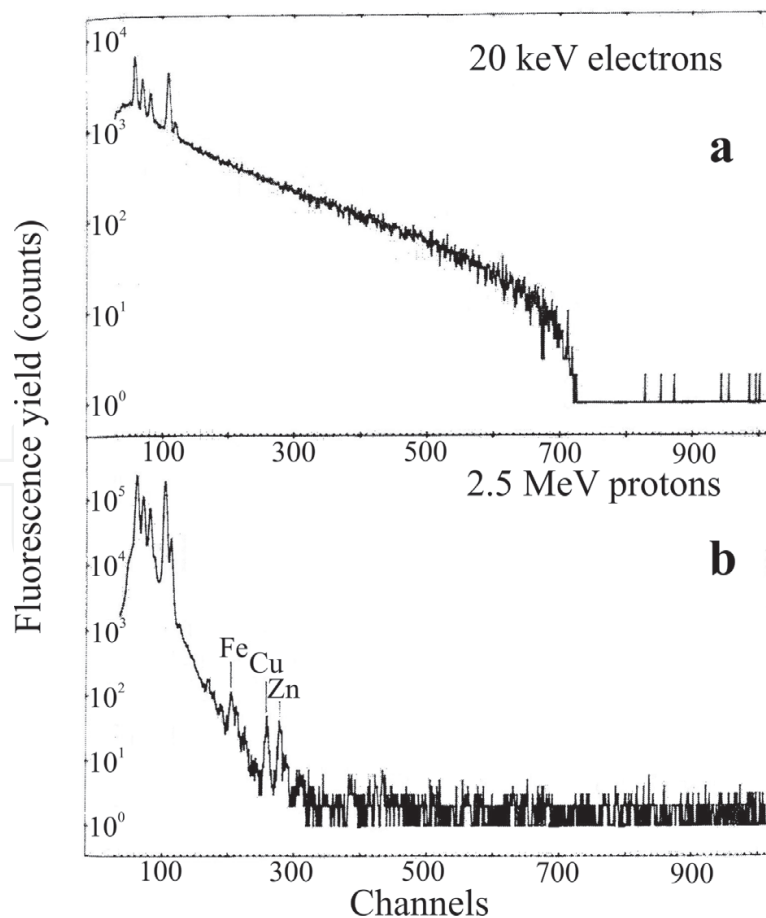


Figure 24. X-ray fluorescence spectra of the human brain tissue collected in conditions of the electron beam ($E_0 = 20 \text{ keV}$) excitation (a) and the proton beam ($E_0 = 2.5 \text{ keV}$) application (b) [36].

comparison shows that the ion beam excitation leads to the background intensity decreasing in result of the bremsstrahlung photon yield reduction. In the presented data, the ion beam excitation application allows to registrate Fe, Cu and Zn atoms presence in the studied target. In the result, one can establish that the PIXE method is characterized by very low magnitudes of detection levels. At the same time, it should be emphasized that the PIXE spectrometry is not the quantitative analytical method. PIXE measurement results are controlled by the matrix effect [37] and by the specific factor connected with the absorption cross-section distinction for different characteristic lines. The last factor is defined by the material layer thickness responsible for the line X-ray fluorescence yield. (This factor can be eliminated by using the planar X-ray waveguide-resonator, see **Figure 5**.)

PIXE element diagnostics, in addition to the matrix and absorption effects, must take into account specific peculiarities of the X-ray fluorescence yield registration by the energy dispersion detector. Any X-ray detector is equipped by the input window, which absorbs the collected radiation. Moreover, X-ray detector is characterized by the reduced efficiency at the high energy photon registration. **Figure 25** presents the experimental diagram reflecting the X-ray radiation efficiency registration for the wide range of photon energy. Best results of the light element diagnostics can be obtained with X-ray detectors equipped by C_1 and C_2 superfine windows because it allow to collect PIXE spectra up to the photon energy $E \cong 0.1$ keV. As a whole, the PIXE spectrometry is very beautiful supplement to the RBS spectrometry.

4.2. PIXE for the material element analysis

Distinction in the X-ray fluorescence yield excitation cross-section demonstrated in **Figure 23** can be illustrated by the direct experimental measurements. **Figure 26** shows spectra of the

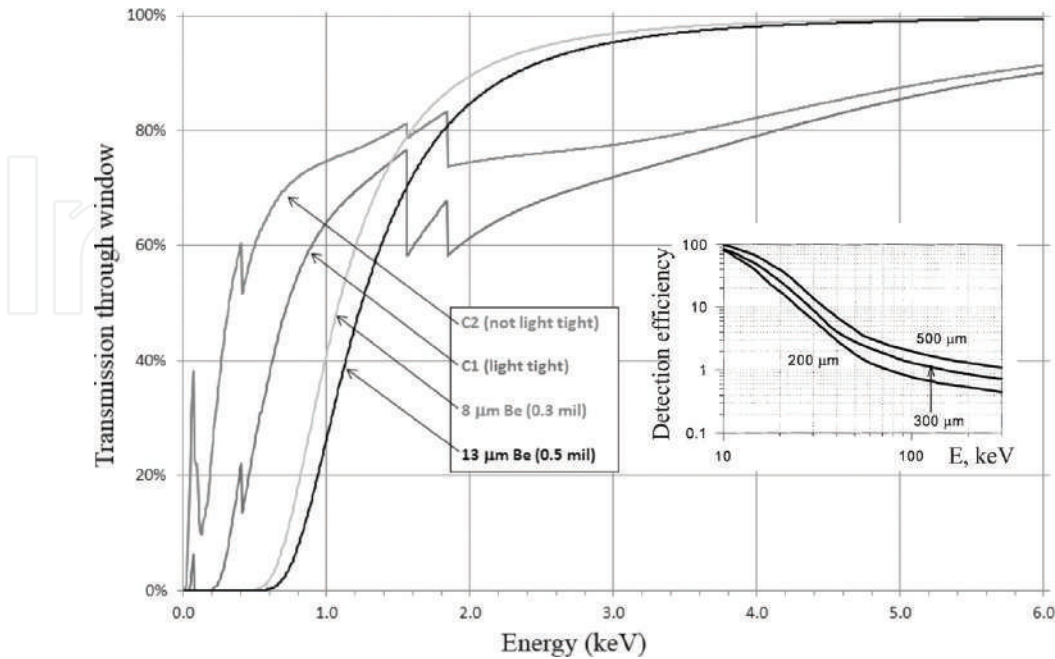


Figure 25. X-ray radiation energy efficiency of the SDD detector equipped by different input windows. Insert shows the efficiency dependence on the detector working plate thickness.

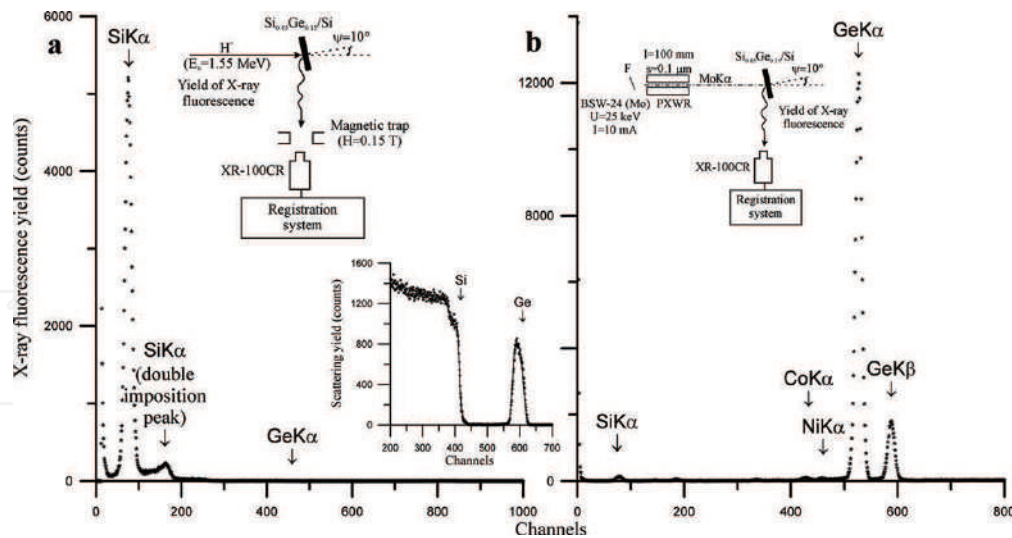


Figure 26. Comparison of X-ray fluorescence yield for $\text{Si}_{0.85}\text{Ge}_{0.15}/\text{Si}$ epitaxial structure collected in conditions of the proton beam (a) and the $\text{MoK}\alpha$ radiation flux excitation (b). Arrows shows the energy position of X-ray characteristic lines collected by X-ray pin detector. Insertions show the measurements geometry and RBS He^+ ($E_0 = 1.525$ MeV) ions spectrum for the target. Energy steps for ones 1.9 keV/channel.

X-ray fluorescence yield excited by the proton beam and the $\text{MoK}\alpha$ radiation flux. For the reference, the figure presents experimental and theoretical RBS spectra of the target. The target is the silicon-germanium epitaxial film with thickness 112 nm on the silicon monocrystal substrate. Experimental spectrum was collected in the target random position. Comparison of X-ray fluorescence spectra collected in conditions of the different excitation methods use shows that the PIXE approach is more effective for the light element diagnostics in materials, but the X-ray fluorescence excitation is more preferable in case of the heavy element analysis. It is very important to notice that the ion beam excitation provokes the X-ray characteristic fluorescence yield by very high intensity. The spectrum excited by the proton beam with current $I = 2$ nA (1.2×10^{10} ion/sec) was registered for 5 seconds, at the same time, the time registration of spectrum excited by the $\text{MoK}\alpha$ radiation flux ($N = 4 \times 10^5$ photon/sec) was equal 300 s. High intensity of the X-ray fluorescence yield characteristic for the first spectrum is borne out by the double imposition peak appearance. So, in the last experiments, we use SDD silicon detector in frame of the Sokol-3 ion beam analytical complex facility, which can work at the enhanced pulse loading without double imposition peaks.

High efficiency of the PIXE light element diagnostics was used in our investigations of the geological object. **Figure 27** shows the proton-induced X-ray emission spectrum of the $(\text{Mg}_{0.93}\text{Fe}_{0.07})_2\text{SiO}_4$ natural olivine. Host composition of the mineral was defined by RBS method. Experimental and theoretical spectra of the object are presented in the figure, too. PIXE measurements allow to fix in the target structure the Ca, Cl, S, Al and Na elements set existence. Quantitative analysis of the target contamination can be carried out by the TXRF spectrometric method [38].

PIXE spectrometry can be used for petroleum contamination analysis. **Figure 28** shows TXRF and PIXE spectra demonstrating the contamination set existence in the petroleum film deposited on Be substrate. RBS spectrum of the film is shown in **Figure 14**. TXRF spectrum allows to

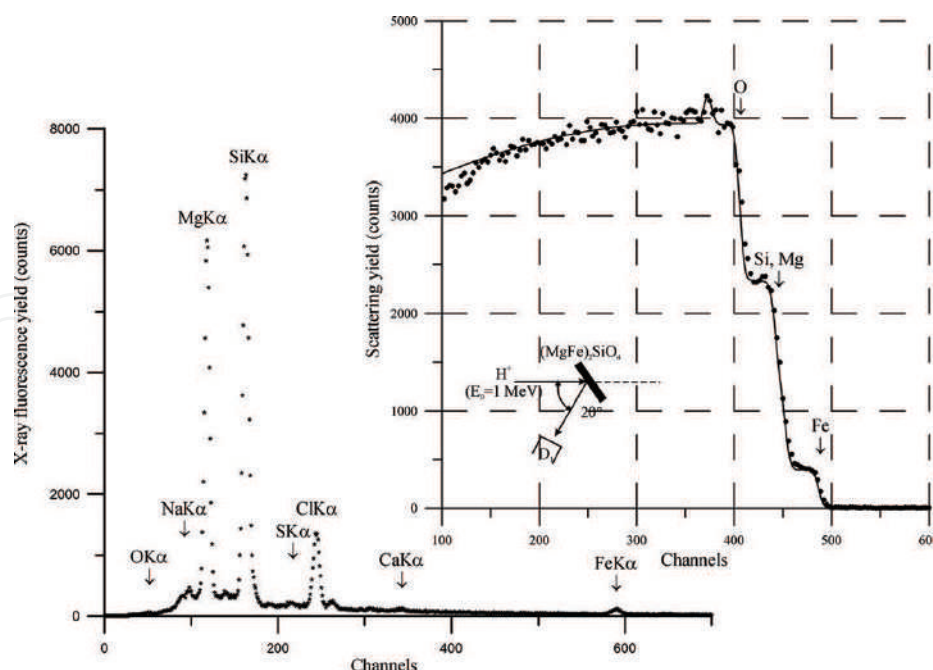


Figure 27. PIXE spectrum of the olivine natural crystal collected in result of H^+ ion beam excitation. Arrows shows the energy position of X-ray characteristic lines collected by SDD silicon detector. Rutherford backscattering spectrum of the target is presented on insert. Energy step for PIXE spectrum 10.9 eV/channel, for RBS 1.9 keV/channel.

produce the quantitative analysis of the contamination concentration that used the sulfur atomic content as the internal standard. TXRF and PIXE spectra confirm the vanadium atoms presence in the petroleum sample. At the same time, the La atoms concentration diagnostics is inaccessible for the total X-ray external fluorescence spectrometry. PIXE analysis is able to fix the La atoms presence in the petroleum sample. The lanthanum atomic content was evaluated by using the comparison method with data for Ca and V atom concentration. It is 0.0005 if the sulfur concentration is elected as a one. PIXE diagnostics of the solution dry residue is the very perspective application for this specific target.

PIXE measurements can be used for the nonstandard element analysis. **Figure 29** shows RBS and PIXE spectra collected for the leather processing material by using the proton beam excitation. RBS spectrum allows to evaluate the host elements concentration (except hydrogen atom), at the same time, the PIXE investigation takes possibilities to fix the contamination element presence in the leather processing material. How showed experience of the leather goods manufacturing the chromium and contamination concentrations defines quality of different products manufactured from the leather. The quantitative contamination analysis can be executed by TXRF method application. But if the TXRF spectrometry sensitivity is not enough, it is possible to use the planar X-ray waveguide-resonator for the trace surface element diagnostics in frame of the PIXE excitation of the X-ray fluorescence yield. The experimental scheme for such measurement execution is presented in **Figure 5b**, and the diagnostic method has name – TXRF PE.

Figure 30 presents the experimental data characterizing the method possibilities on base of the old coin study. PIXE spectrum shows X-ray fluorescence lines initiated by surface and

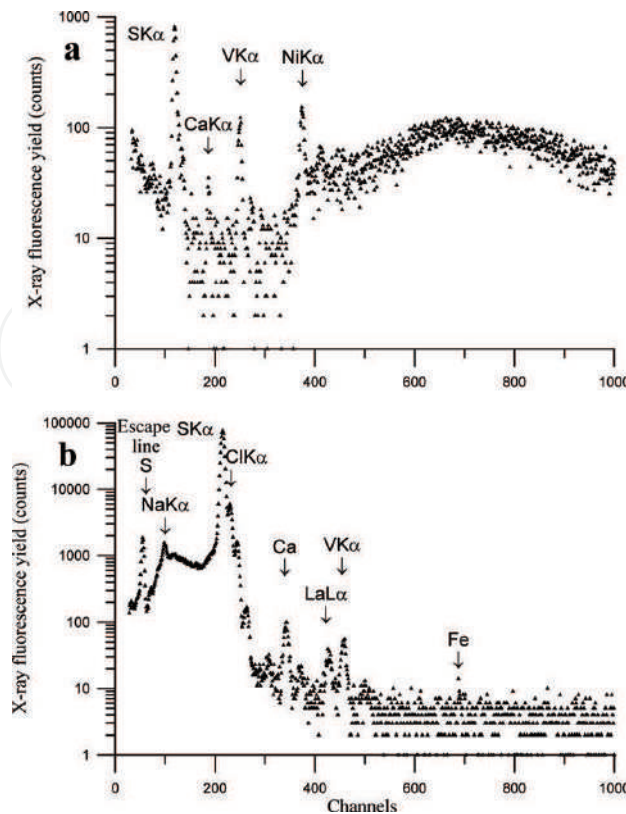


Figure 28. X-ray fluorescence spectra collected for the petroleum film deposited on Be substrate by use the TXRF and the PIXE spectrometry. Energy step for TXRF spectrum 20 eV/channel, and 10 eV/channel for PIXE spectrum. TXRF fluorescence yield was excited by the MoK α flux, PIXE – by the proton beam with energy $E_0 = 0.953$ MeV. Arrows show the energy position of X-ray characteristic lines collected by SDD silicon detector.

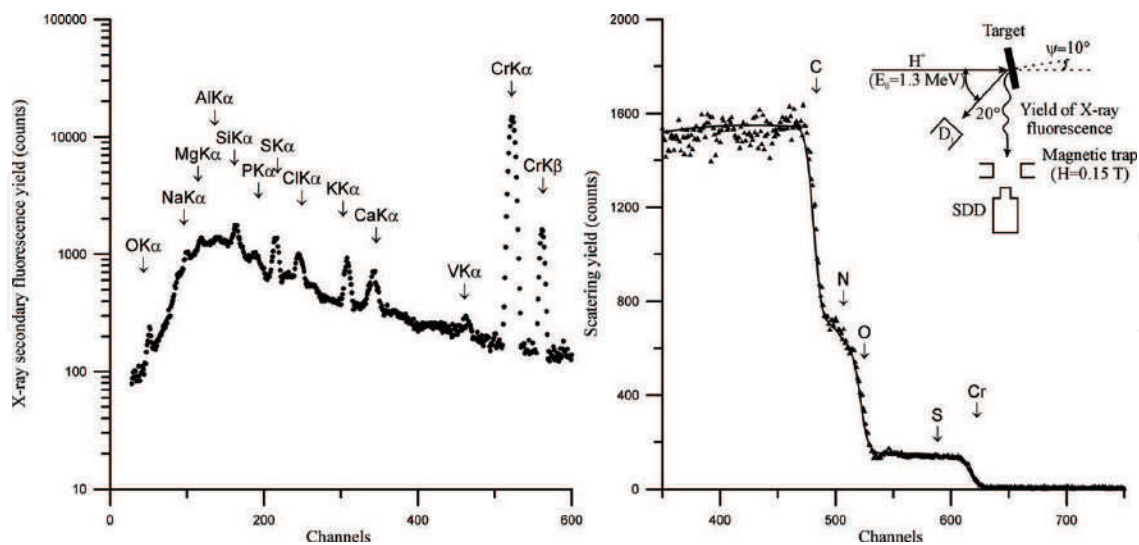


Figure 29. Experimental and theoretical RBS H^+ ($E_0 = 1.3$ MeV) ions for the sample of thin leather – processing material and PIXE spectrum of the one collected in the same experiment. Arrows on the RBS spectrum show the ion scattering energies on nuclei of atoms located on the sample surface, and on the PIXE spectrum show the energy position of X-ray characteristic lines collected by SDD silicon detector. Energy step for RBS spectrum 1.9 keV/channel, for PIXE one 10 eV/channel. Insert shows the measurement geometry.

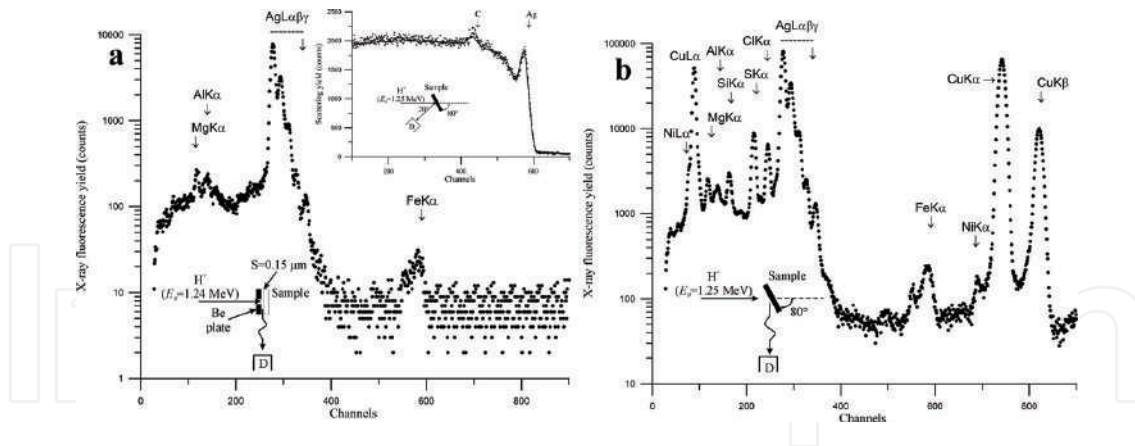


Figure 30. TXRF PE (a) and PIXE (b) spectra of the half copeck old coin fabricated from copper with the surface Ag coating ($t = 170$ nm) collected by SDD silicon detector in conditions of the X-ray fluorescence excitation by the proton beam ($E_0 = 1.25$ MeV). Inserts show measurements geometry and RBS H^+ ions spectrum of the target. Arrows on fluorescence spectra show of the energy position of X-ray characteristic lines and on RBS one ion scattering energies on nuclei located on the coin surface. Energy step for fluorescence spectra 10.5 eV/channel for RBS one 1.9 keV/channel.

volume atoms of the target. In its turn, TXRF PE spectrum reflects X-ray fluorescence lines characteristic for the coin surface. (Carbon peak on the Rutherford backscattering diagram is connected with the C-H film appearing in process of the proton beam scattering in the measurement period.) The X-ray fluorescence spectra comparison allows to conclude that the Mg, Al and Fe atoms contamination are typical for the Ag coating. This conclusion was confirmed by the TXRF direct study. So, new experimental method can be recommended for the trace light elements diagnostic in addition to the standard TXRF experimental measurements.

5. Nuclear elastic recoil for the hydrogen diagnostics

It is known, that the hydrogen atoms diagnostic can be carried out by using the direct resonance nuclear reaction, for example, $^1H(^{15}N; \alpha, \gamma)^{12}C$ and $^1H(^{19}F; \alpha, \gamma)^{16}O$, or by the nuclear elastic recoil (NER) method [16]. The resonance method has a limited spearing because its application demands ion beams with the enhanced energy. For example, the low energy resonance of $^1H(^{15}N; \alpha, \gamma)^{12}C$ reaction has value 3.35 MeV. So, the nuclear recoil spectrometry is more accessible while less informative. The experimental scheme for the nuclear recoil method is presented in **Figure 6b**. The measurement scheme assumes the surface target installation on the $\theta_1/2$ small angle about of the helium ion beam propagation line and the recoil and scattering ion detector placing under the θ_1 angle. The detector must have a collimator and the thin film absorber. The absorber thickness must provide a total absorption of the helium ions scattering flux. In these conditions, the recoil hydrogen atoms undergo the noticeable straggling [10–16]. The straggling effect is characterized by the ion beam average energy decreasing attended by increasing of the ΔE energy dispersion. Moreover, it is a need to take into account the adsorbed layer existence on the any material surface, which contains some hydrogen quantity. As a rule, the hydrogen surface concentration is higher in comparison of the hydrogen target volume content.

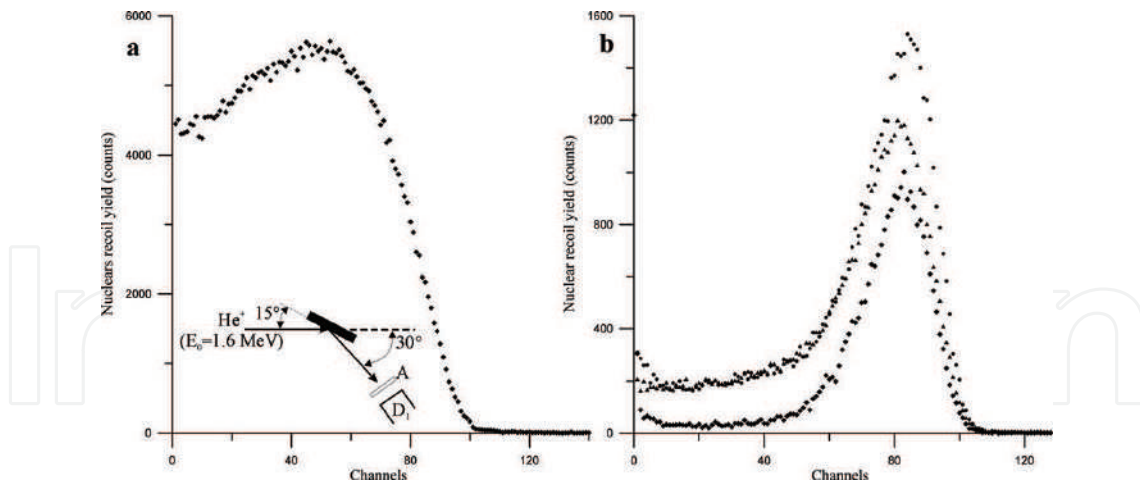


Figure 31. Nuclei elastic recoil spectra of the $\text{TiH}_{0.98}$ weighting etalon (a) and some perovskite structures (b) collected in the specific geometry allowed to fix the hydrogen atoms recoil. Hydrogen recoil spectrum for SrTiO_3 monocrystal (\bullet), for BSTO film on MgO substrate (\blacktriangle), for BSTO film Si substrate (\blacklozenge). Measurement geometry is presented on insert. Energy step 3.8 keV/channel.

The nuclei recoil spectrometry, similar to the RBS method allows to produce the absolute analysis. At the same time, it is possible to use standard samples attested by the precision weighting. We used $\text{TiH}_{0.98}$ as the similar etalon. **Figure 31** shows NER spectra of the etalon and some perovskite structures. Data obtained from the etalon spectrum allows to evaluate the hydrogen content in studied perovskite structures. It is very strange but the hydrogen atoms concentration in the SrTiO_3 monocrystalline structure was near 4% at. Similar hydrogen content was detected in the BSTO film deposited on MgO substrate. The BSTO film deposited on the silicon substrate had smaller hydrogen atoms in its structure (near 1% at.). Evaluation of the hydrogen atoms in surface absorbed layers shows that the film has the C_1H_1 composition. NER measurements are characterized by specific conditions. The helium ion beam energy must be higher as 1.5 MeV. At smaller energy of the beam some experimental and interpreting difficulties appear.

6. Nuclear reaction analysis application for the material study

Nuclear reactions excited by high energy ion beams can have the resonance nature and can demonstrate the threshold characteristics[39]. It is the isotopically sensitive methods. Some nuclear reactions have the practical significance. It is the $^{27}\text{Al}(p,\gamma)^{28}\text{Si}$ famous resonance reaction, which uses for the ion beam accelerator calibration [40]. Nuclear reaction analysis (NRA) is mostly used for the light element diagnostics in material. In our work we applied the $^{11}\text{B}(p,\alpha)^8\text{Be}$ nuclear reaction for study of the electro-rocket engine function peculiarities [41]. The main investigation task of the study was the elements spatial distribution determination in the engine output jet. The engine discharge chamber was manufactured from the material elaborated on the BN base composition. So, it is expected that the main admixture element in the xenon jet will be boron. For the boron spatial distribution in the engine jet, we used the Be plates set arranged on different angles about the jet propagation line. The deposit on the Be

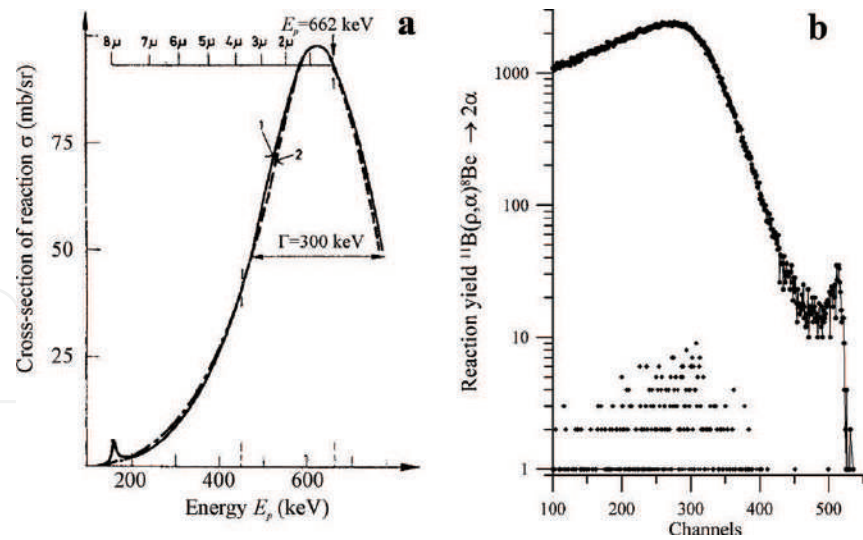


Figure 32. Cross-section energy dependence of the $^{11}\text{B}(\text{p}, \alpha)^8\text{Be}$ nuclear reaction (a) [43], and the reaction yields for the $\text{B}_{0.4}\text{N}_{0.45}\text{X}_{0.15}$ engine ceramic, for the Be plate with deposited film, which was arrangement on angle 59 about the jet propagation line and for the Be clean plate.

Isotope	Content in nature, %	Nuclear reaction	Energy of proton, keV	Cross-section of reaction, mb/sr	Width of resonance, keV	Emission product $E_\gamma, E_{\alpha}, \text{ MeV}$	Limits detection, at. %
^6Li	7.62	—	—	—	—	—	—
^7Li	92.58	$^7\text{Li}(\text{p}, \gamma)\text{Be}^8$	441	6	12	17.65; 14.75	~100 ppm
^9Be	100	$^9\text{Be}(\text{p}, \alpha)^6\text{Li}$	330	4	1.5	8.5; 14.2	~50 ppm
^{10}B	19.61	$^{10}\text{B}(\text{p}, \gamma)$	1146	0.01	570		~10 ppm
^{11}B	80.39	$^{11}\text{B}(\text{p}, \alpha)^8\text{Be}$	650	90	10	~; 3.7	~10 ppm
^{12}C	98.89	$^{12}\text{C}(\text{p}, \gamma)^{13}\text{N}$	459	0.13	40	2.36; —	~120 ppm
^{13}C	1.11	$^{13}\text{C}(\text{p}, \gamma)^{14}\text{N}$	550	1.44	32	8.6; —	~100 ppm
^{14}N	99.64	$^{14}\text{N}(\text{p}, \gamma)^{15}\text{O}$	278	~0.01	1.6	6.8	~100 ppm
^{15}N	0.36	$^{15}\text{N}(\text{p}, \gamma)^{12}\text{C}$	898	800	2.2	4.43	~10 ppm
^{16}O	99.8	—	—	—	—	—	—
^{18}O	0.2	$^{18}\text{O}(\text{p}, \alpha)^{15}\text{N}$	730	15	10	3.4	~10 ppm
^{19}F	100	$^{19}\text{F}(\text{p}, \gamma, \alpha)^{16}\text{O}$	872	661	4.5	6.13	~1 ppm
^{23}Na	100	$^{23}\text{Na}(\text{p}, \alpha)^{20}\text{Ne}$	592	4	45	2.238	~20 ppm
^{24}Mg	78.6	$^{24}\text{Mg}(\text{p}, \gamma)\text{Al}^{25}$	1200	~0.01	<10	3.44; 1.83; 1.61	~200 ppm
^{25}Mg	10.2	$^{25}\text{Mg}(\text{p}, \gamma)\text{Al}^{26}$	317	~0.01	12	6.19; 4.86; 0.82	~500 ppm
^{26}Mg	11.2	$^{26}\text{Mg}(\text{p}, \gamma)\text{Al}^{25}$	661	~0.01	<10	7.88; 6.68; 5.9	~500 ppm
^{27}Al	100	$^{27}\text{Al}(\text{p}, \gamma)^{28}\text{Si}$	992	0.1	0.05	1.77; 7.93; 10.78	~10 ppm

Table 1. Resonant nuclear reaction parameters for light element isotopes initiated by proton beams.

plates was analyzed by the boron resonance reaction. Cross-section energy dependence of the reaction is presented in **Figure 32a** [42]. **Figure 32b** shows the pattern of our measurements, which allowed to evaluate the boron spatial distribution in the jet of electro-rocket engine. Similar investigations are very effective but are very expensive. At the same time, it is useful to have a grasp about possibilities of NRA methods application and atomic detection limits determination on base of the real nuclear reaction use. **Table 1** presents the information about the most useful reaction applied for the light element diagnostics.

7. Some peculiarities of the ion beam optical luminescence excitation

Our active investigations in the optical scintillation field at ion beam excitation were connected with the PbWO_4 and LaF_3 luminescence response study [43–45]. Interest to the PbWO_4 luminescence characteristic study was initiated by the fast component existence in the luminescence response at the proton beam excitation. There was the specific interest to fix the luminescence distinction between yields in the random and the channeling orientation of the crystal and to study kinetic of the luminescence yield dependence on the absorbed radiation dose. Results of these investigations are shown partially of **Figure 33**. The luminescence spectrum obtained in the channeling proton beam condition demonstrates some integral intensity yield increasing [43] and is characterized by some spectrum variation. Dosimetric data showed that luminescence yield intensity reduces as the radiation dose increases up to some critical value J_∞ . After

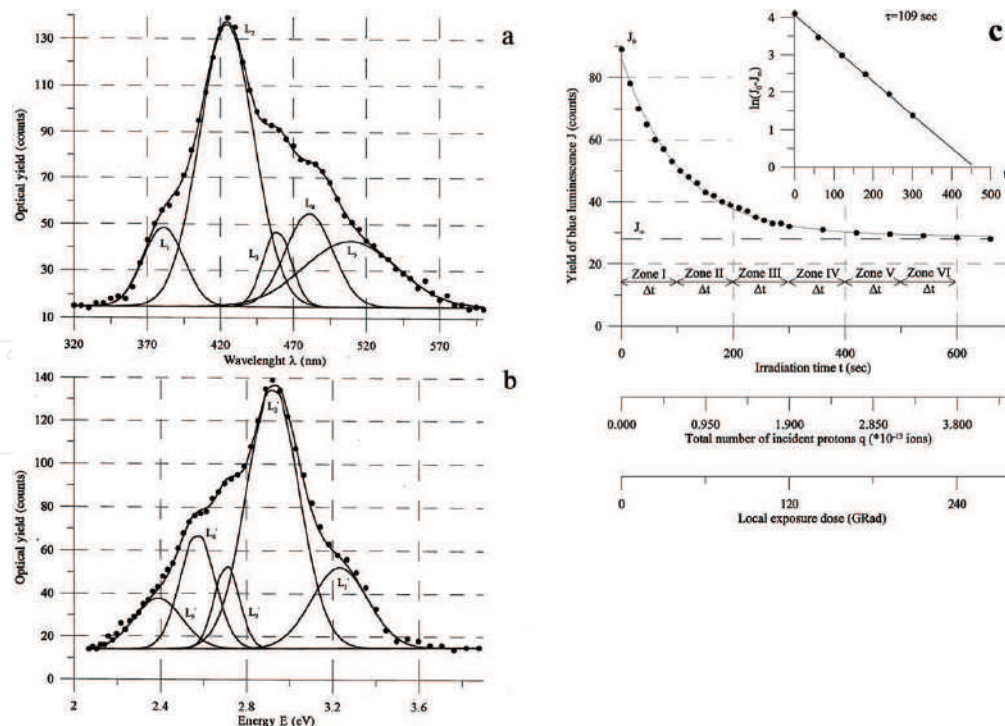


Figure 33. Luminescence yield optical spectra for random (a) and channeling along [001] axis (b) of PbWO_4 monocrystal target executed by H^+ ions beam ($E_0 = 0.9$ MeV), and the kinetic function of random spectrum blue component ($\lambda_0 = 412$ nm) on the absorbed radiation dose.

warning at $t = 100^\circ\text{C}$ during $\tau=600$ s, the PbWO_4 target had got the critical radiation dose returned into the initial state. Total interpretation of the experimental data is very difficult, but some results of our investigations were found useful for the elaboration of the PbWO_4 monocrystal great size preparation technology. The experimental arrangement used for our luminescence study in conditions of the ion beam excitation is presented in **Figure 6**. The ion luminescence investigations does not have wide spread use owing to the interpretation problems existence. At the same time, it is a need to understand that the ion beam luminescence excitation mechanism is different from the X-ray, gamma ray and electron beam excitation one. In case of the PbWO_4 excitation by the proton beam, we can observe the L_1 luminescence line being absent at any other excitation types.

8. Monocrystalline and epitaxial structures study by the ion beam channeling method

How it was discussed early peculiarities of the ion beams interaction with materials is defined by the material structure features. Experimental investigations of very much crystals confirmed the Starks assumption about possibility for high energy ions to propagate through the crystal almost without scattering in case of its movement along ordered atomic chains [46]. This effect was called the ion beam channeling in crystals. Fundamental features of the effect and its possible practical application were discussed in details in the specific monograph [20]. Some features of the effect were studied in our investigation. **Figure 34** shows this effect observation for the monocrystalline synthetic diamond target prepared by the temperature gradient method realized at the high hydrostatic pressure conditions. Ion beams axial channeling along [100] axis of the target demonstrates the high perfection structure ($\chi_{\text{exp}} = 0.23$ at $\chi_{\text{tcor}} = 0.09$). W atoms are the main admixture of the target. The hydrogen ion channeling allows to evaluate the channeling effect depth for the diamond. SiO_2 thin film presents on the diamond surface. It is the result of polishing procedure. The studied diamond target has noticeable sizes ($0.5 \times 5 \times 5 \text{ mm}^3$). It can be used as the substrate for the power integral circuits

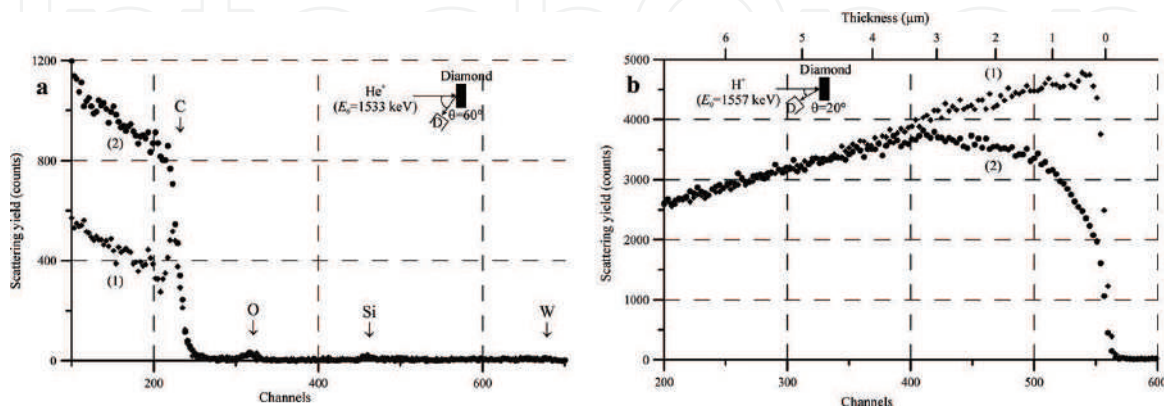


Figure 34. Experimental RBS He^+ and H^+ ions spectra for the random position (a) and the channeling orientation through [100] axis (b) of the diamond monocrystal. Arrows show the ion scattering energies on nuclei of atoms located on the target surface. Measurement geometries are shown on inserts. Energy step 1.9 keV/channel. (1) Random orientation. (2) Channeling.

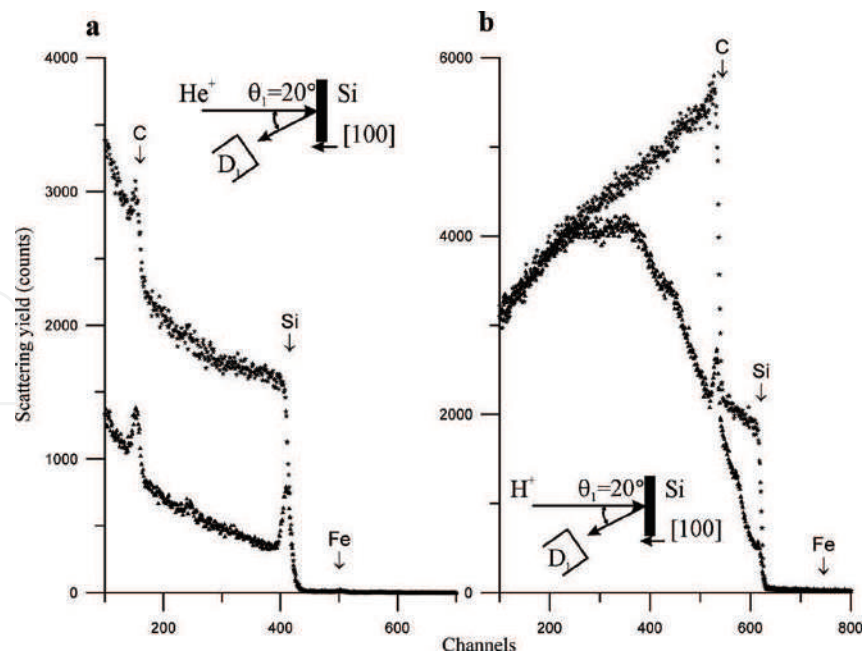


Figure 35. Experimental RBS He^+ (a) and H^+ (b) ions spectra for the SiC monocrystal in the random position and the channeling condition along [001] axis. Arrows show the ion scattering energies on nuclei of atoms located on the target surface. Experimental geometries is shown on inserts. Energy step 1.9 keV/channel.

preparation and the X-ray tube windows manufacturing owing to its high thermal conductivity. Other sample of the ion beams axial channeling is shown in **Figure 35**. It demonstrates patterns of He^+ and H^+ ion beams channeling along [001] axis of SiC monocrystal prepared by the Lely method [47]. RBS measurements executed for the random and oriented conditions showed that the silicon carbide crystalline structure has high perfection ($\chi = 0.36$). The target structure is characterized by the 6H hexagonal polytype with crystallographic parameters of the cell $a = 0.308$ nm, $c = 1.512$ nm. Because the preparation method is connected with molten metals, Fe atoms are a chief contamination of the target. The technology preparation of SiC monocrystalline boules is very important for the nanophotonics because the silicon carbide material is very suitable for manufacture of light emitting diodes (LED) on base of the high energy-gap semiconductors. In the context of this, very interesting works of Prof. Kukushkin are connected with combination of the silicon and the silicon carbide technologies [48]. He elaborated the technology of SiC/Si epitaxial heterostructure preparation. The ion beam analysis application showed that the SiC/Si heterostructure is characterized by low perfection but the crystallographic epitaxy existence [49]. Moreover, on base of the SiC/Si substrate, they were able to prepare the effective light emission structure. So, the ion beam analysis application to the compositions diagnostics having the SiC structure has the direct practical application.

The living practical interest is connected with perovskite crystals and its heterostructures investigations. It is well known, that multielement oxide films fabricated on base of the doped barium titanate (BaTiO_3) are assumed to be promising material structures for the development of micro and nanoelectronic and electro-optical devices. Such coatings are potentially applicable as electro-optical modulators and phase shifter, switching devices, optical microprocessors, surface waveguide-acoustic transducers and capacitive elements in dynamic memory. Experimental investigations showed that the epitaxial coatings on single crystals substrates with appropriate

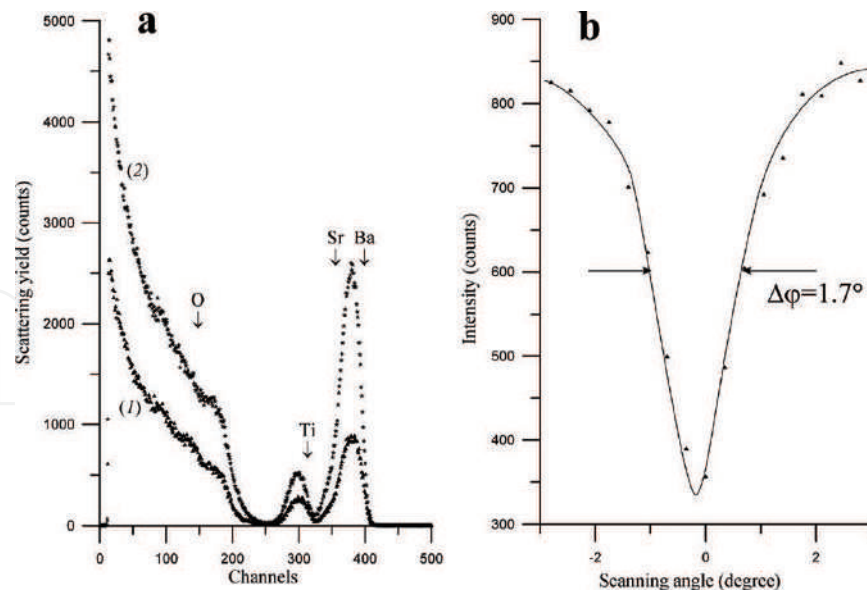


Figure 36. Experimental RBS He^+ ions spectra for $\text{Ba}_{0.8}\text{Sr}_{0.2}\text{TiO}_3/\text{MgO}$ epitaxial structure in the random position and the channeling condition along $[100]$ structure axis (a) and the rocking resette near the channeling axis (b). Arrows show the ion scattering energies on nuclei of atoms located on the target surface. Measurement geometry is presented on the insert. Energy step 1.9 keV/channel.

crystallographic parameters exhibit the best electro-optical properties. So, the BSTO films study deposited on different substrates were one of our priority films study deposited on research direction. **Figure 36** shows experimental RBS spectra of the $\text{Ba}_{0.8}\text{Sr}_{0.2}\text{TiO}_3/\text{MgO}$ epitaxial heterostructure collected for the target random position and in conditions of He^+ ion beam channeling along $[100]$ direction. Comparison of He^+ ion scattering spectra collected in the random and channeling target disposition shows that the scattering yield proportional decreasing for the film and substrate atoms takes place. Moreover, rocking rosettes obtained for film and substrate atoms showed the identical form. At the same time, it is a need to notice that the χ experimental factor for the target is twice as much as the theoretical magnitude $\chi_{\min} = 0.18$. It is showed that the target structure is characterized by some nonperfection. But the ion beam channeling along the sole crystallographic axis does not always reflect real degree of the target structure perfection. Similar information can be accessible at the channeling data use for some crystallographic axis. Sample of such situation is presented in **Figure 37**. It shows experimental and theoretical RBS He^+ ions spectra for the $\text{Si}_{0.8}\text{Ge}_{0.2}/\text{Si}$ epitaxial structure obtained for random target positions and oriented states and the rocking rosettes of the ion beam channeling near $[100]$ and $[110]$ axis [50]. The minimum yield for the He^+ ion beam channeling along $[100]$ axis is near this parameter theoretical magnitude ($\chi_{\min} = 0.03$). One can expect on base of the RBS channeling spectrum that the thin film epitaxial structure is characterized by the almost ideal perfection. But the ion beam channeling spectrum along $[110]$ crystallographic axis does not confirm the similar expectation. Experimental magnitude of the minimum yield parameter for the $[110]$ silicon crystallographic axis is higher as the theoretical one on two times. This discrepancy is connected with the elastic stress owing to the magnitudes difference of film and substrate unit cells. In this case, the structure distortions have an anisotropic character. The stress value is dependent on the film composition and its thickness. Thick films demonstrate the exfoliation trend. The channeling method can be used with success for the light element diagnostic

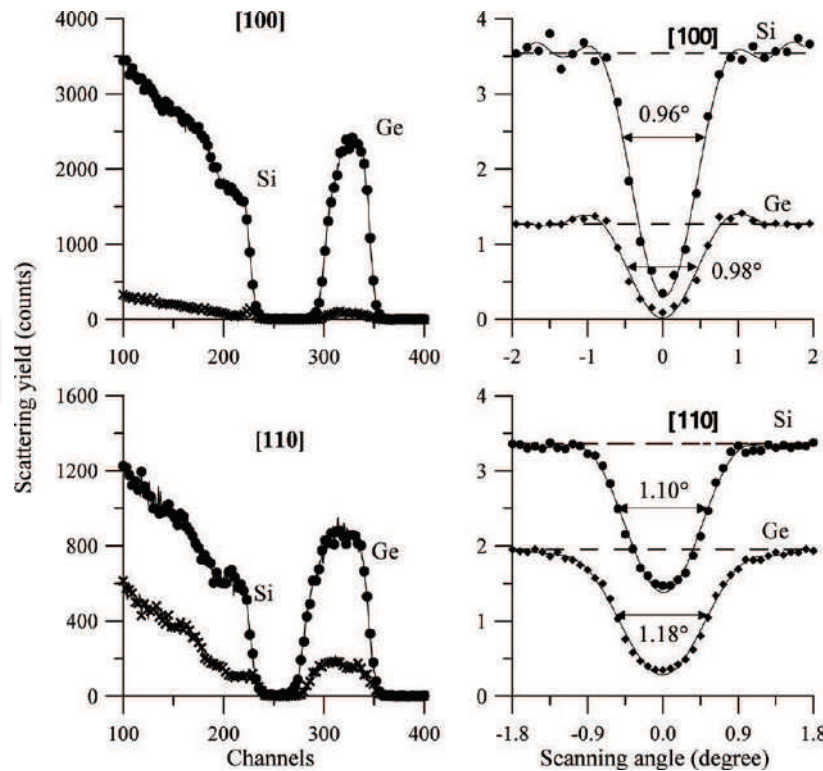


Figure 37. Experimental RBS He^+ ions spectra for $\text{Si}_{0.8}\text{Ge}_{0.2}/\text{Si}$ epitaxial structure in the random positions and the channeling conditions along [100] axis, [110] axis and the rocking rosettes near the channeling axis. Arrows show the ion scattering energies on nuclei of atoms located on the target surface. Measurement geometries is shown on inserts. Energy step 1.9 keV/channel.

implanted into the monocrystalline objects. It has possibilities to study the structure defects types and its distribution [22]. But it is a need to notice that the channeling method is very expensive.

9. Conclusion

Short review of the ion beam spectrometry and analytical method built on base of the ion beams interaction with material shows that the methods application is very useful and in some cases unique. All ion beam analytical methods are the nondestructive technique. RBS spectrometry is the only instrumental method being not demanded analytical standards and etalons. Complex application of the material ion beam analysis allows to present the total description of the material properties. But the cost of its use is very high.

Acknowledgements

We are grateful to Prof. S.A. Kukushkin and Dr. M.S. Afanas'ev for helping this work. The work was partially supported by Russian Foundation for Basic Researches (project #16-07-00665) and state task #007-00220-18-00. This paper received partial financial supported by the Ministry of Education and Science of the Russian Federation on the program to improve the

competitiveness of Peoples' Friendship University of Russia (RUDN University) among the world's leading research and education centers in the 2016–2020.

Author details

Vladimir Egorov^{1*} and Evgeny Egorov^{1,2}

*Address all correspondence to: egorov@iptm.ru

1 Institute of Microelectronics Technology Russian Academy of Science (IMT RAS), Chernogolovka, Russia

2 RUDN University, Moscow, Russia

References

- [1] Schmidt B, Wetzig K. Ion Beam in Material Processing and Analysis. Wien: Springer; 2013. p. 418
- [2] Bird JR, Williams JS. Ion Beams for Material Analysis. Sidney: Academic Press; 1989. p. 719
- [3] Townsend PD. Optical effect of ion implantation. Reports on Progress in Physics. 1987;**50**: 501-558
- [4] Pop SS, Belikh SF, Drobnich VG, Ferleger VK. Ion-Photon Metal Emission. Tashkent: FAN; 2000. p. 200 (In Russian)
- [5] Huddle JR, Grant PG, Ludington AR, Foster RL. Ion beam-induced luminescence. NIM. 2007;**261**:475-476
- [6] Koljada VM, Zaychenko AK, Dmitrenko PV. X-Ray Spectral Analysis at the Ion Beam Excitation. Moscow: Atomizdat; 1978. p. 248 (In Russian)
- [7] Johansson SAE, Campbell JL. PIXE: A Novel Technique for Element Analysis. New York: Wiley; 1988. p. 347
- [8] Instrumentation for PIXE and RBS. Special Issue of International Atomic Energy Agency (IAEA). IAEA-TECDOC-1190. Vienna: IAEA; 2000. p. 83
- [9] Petrov NN, Abrojan IA. Surface Diagnostics by Ion Beams Application. Leningrad: LGU Press; 1977. p. 160 (In Russian)
- [10] Chu WK, Majer JM, Nicolet MA. Backscattering Spectrometry. New York: Academic Press; 1978. p. 384
- [11] Shipatov ET. Background Scattering of Fast Ions, Theory, Experiment, Practice. Rostov-on-Don: Rostov State Univ. Press; 1988. p. 155

- [12] Tesmer JR, Nastasi M, editors. Handbook of Modern Ion Beam Material Analysis. Pittsburgh: MRS Published; 1995. p. 704
- [13] Hellbord J, Whitlow HJ, Zhang Y. Ion Beams in Nanosize and Nanotechnology. Heidelberg: Springer; 2009. p. 457
- [14] Nastasi M, Mayer JW, Wang Y. Ion Beam Analysis, Fundaments and Application. Boca Raton: CRC Press; 2015. p. 434
- [15] Chernov IP, Shadrin VN. Analysis of Hydrogen and Helium Concentration by the Nuclei Recoil Method. Moscow: Energoatomizdat; 1988. p. 129 (In Russian)
- [16] Hofsas H. Forward Recoil Spectrometry. New York: Plenum; 1996. p. 278
- [17] Amsel G, Lanford WA. Nuclear reaction techniques in material analysis. Annual Review of Nuclear and Particle Science. 1984;**34**:435-460
- [18] Ehmann WD, Vance DE. Radiochemical and Nuclear Methods of Analysis. New York: Wiley; 1991. p. 531
- [19] Rauhala E. Proton elastic scattering cross-section of carbon, nitrogen and silicon for back-scattering analysis in the energy range 0.7-2.5 MeV. NIM. 1985;**12**:447-452
- [20] Feldman LC, Mayer JW, Picraux ST. Material Analysis by Ion Channeling. New York: Academic Press; 1982. p. 300
- [21] Shipatov ET. Ions Channeling. Rostov-on-Don: Rostov State Univ. Press; 1986. p. 144 (In Russian)
- [22] Gotz G, Gartner K, editors. High Energy Ion Beam Analysis of Solids. Berlin: Acad. Verlag; 1988. p. 342
- [23] Doolittle LR. Algorithm for the rapid simulation of Rutherford backscattering spectra. NIM. 1985;**9**:344-351
- [24] Egorov V, Egorov E, Afanas'ev M. TXRF spectrometry at ion beam excitation. IOP Publishing; IOP Conf. Ser.: Journal of Physics: Conf. Ser. 2017;**808**:012002. DOI:10.1088/1742-6596/808/1/012002
- [25] Egorov V, Egorov E. Waveguide-resonance mechanism for X-ray beam propagation. Advances of X-ray Analysis. 2003;**46**:307-315
- [26] Ziegler JF. The Stopping and Ranges of Ions in the Matter. New York: Pergamon Press; 1977. p. 367
- [27] Mayer M. SIMNRA: simulation of RBS, ERD and NRA spectra [Internet]. 1999. Available from: [http://home.mpcdf.mpg.de/~mam/Mayer-AIP-Conference-Proceedings-475-\(1999\)-541.pdf](http://home.mpcdf.mpg.de/~mam/Mayer-AIP-Conference-Proceedings-475-(1999)-541.pdf) [Accessed: 2018-02-19]
- [28] Mehrer H. Diffusion In Solids, Fundaments, Methods, Materials, Diffusion-Controlled Processes. Berlin: Springer; 2007. p. 651

- [29] Poate M, Tu KN, Mayer JW, editors. Thin Film Interdiffusion and Reactions. New York: Wiley; 1978. p. 578
- [30] Aleshin AN, Egorov VK, Bokstein BS, Kurkin PV. Study of diffusion in thin au/cu films. Thin Solid Films. 1993;**223**:51-55
- [31] Aleshin AN, Bokstein BS, Egorov VK, Kurkin PV. Segregation effect on grain-boundary diffusion in thin metallic films. Thin Solid Films. 1996;**275**:144-147
- [32] Egorov VK, Kononenko OV, Kondratiev OS. Porosity of film coatings in Rutherford backscattering. Surface Investigation. 1988;**13**:729-741
- [33] Natelson D. Nanostructures and Nanotechnology. Cambridge: Cambridge Univ. Press; 2015. p. 630
- [34] Cahill TA. Proton microprobes and partial induced X-ray analytical system. Annual Review of Nuclear and Particle Science. 1980;**30**:211-252
- [35] Folkman F, Gaarde G, Huus T, Kemp K. Proton induced X-ray emission as a tools for trace element analysis. NIM. 1974;**116**:487-499
- [36] Johanson SAE, Campbell JL, Malquist KG. Particle Induced X-Ray Emission Spectrometer (PIXE). New York: Wiley; 1995. p. 451
- [37] Seppala A, Raisanen J. Matrix effects in particle induced X-ray emission channeling measurements of ZnSe/GaAs heterostructures. Applied Physics Letters. 1999;**75**(6):820-822
- [38] Klockenkamper R. Total Reflection X-Ray Fluorescence Analysis. New York: Wiley; 1997. p. 245
- [39] Verma HR. Atomic and Nuclear Analytical Methods. Berlin: Springer; 2007. p. 375
- [40] Scharf VH. Particle Accelerators Application in Technology and Research. Somernot: Res. Stud. Press; 1989. p. 663
- [41] Arbatskii VM, Nadiradze AB, Chirov AA, Shaposhnikov VV, Egorov VK. The study of the angular distribution of doped elemental composition in a jet of an electro-rocket engine by ion beam methods. Surface Investigation. 2001;**16**:875-888
- [42] Golicheff I, Locullet M, Engelman C. Analytical application of the direct observation of nuclear reactions induced by low energy protons and leading to the emission of gamma-photons which are measured. Journal of Radioanalytical Chemistry. 1972;**12**:233-250
- [43] Egorov VK, Zuev AP, Egorov EV. Scintillation response of monocrystal PbWO₄ to random and channeled ions. NIM. 1996;**119**:418-424
- [44] Egorov V, Zuev A, Egorov E. Light output of scintillation upon ion excitation of surface layers of PbWO₄ single crystal in oriented and nonoriented positions. Surface Investigation. 1997;**12**:717-731
- [45] Egorov VK, Egorov EV. Luminescence kinetics of PbWO₄ crystal at excitation by H⁺ ion beam. NIM. 2001;**179**:536-542

- [46] Stark J. Bemerkung über strahlen zerstreung und absorption von beta strahlen und rontgenstrahlen in kristallen. *Physikalische Zeitschrift*. 1912;**13**:973-988
- [47] Lely JA. Darstellung von einkristallen von silicium carbide und beherrschung von art und menge der eingebauten verunreinigungen. *Berichte der Deutschen Keramischen Gesellschaft*. 1955;**32**:226-264
- [48] Kukushkin SA, Osipov AV. New method for growing silicon carbide on silicon by solid phase epitaxy, model and experiment. *Physics of the Solid State*. 2008;**50**(7):1238-1245
- [49] Egorov VK, Egorov EV, Kukushkin SA, Osipov AV. Structural heteroepitaxy during thermochemical transformation of silicon to silicon carbide. *Physics of the Solid State*. 2017;**59**:135-141
- [50] Vyatkin AF, Egorov VK, Egorov EV. Study of strain relaxation in epitaxial structure $\text{Ge}_{0.2}\text{Si}_{0.8}/\text{Si}$ at thermo-implantation treatment by ion beam channeling. *Materials Research Society Symposium Proceedings*. 2000;**585**:183-189

IntechOpen